People’s Democratic Republic of Algeria
Ministry of Higher Education and Scientific Research
Ferhat Abbas-Setif1 University
Faculty of Sciences
Department of Physics

Thesis Submitted for the Degree of Doctor 3rd Cycle LMD of Physics in Radiophysics and Biomedical Imaging

Title:

Dosimetric and quality assurance comparison study of radiotherapy beam’s data acquisition equipments and treatment techniques (3D-CRT vs. IMRT) at the cancer fighting centre of Setif

Presented by: **BENKAHILA Karim**

Board of Examiners:

Prof. Djamel MAOUCHE	University of Setif 1	President
Prof. Fayçal KHARFI	University of Setif 1	Thesis Director
Prof. Khadidja BOUDAOUD	University of Constantine 3	Examiner
Dr. Nabil OUNOUGHI	University of Jijel	Examiner
Dr. Fouad BOULAKHSSAIM	Cancer Fighting Centre of Setif	Invited Member

- March 4, 2021-

Acknowledgments

I would like to express my deep gratitude to Professor **Fayçal Kharfi**, my research and thesis supervisor, for his patient guidance, assistance, advices, enthusiastic encouragement and useful critiques of this research work. I would also like to thank Dr. Fouad Boulahkassiam and Mr. Saad Khoudri for their assistance in keeping my progress on schedule by helping me in doing the dosimetry and the analysis of the clinical data. My grateful thanks are also extended to Pr. Bouadoud Khadidja head of the radiotherapy service at the cancer-fighting centre of Setif.

I would like to express my sincere appreciation to the president and members of my thesis examining committee, Pr. D. Maouche, Pr. K. Boudaoud, Dr. N. Ounoughi and Dr. F. Boulakhssaim, for kindly agreeing to serve on my examining committee.

I would also like to extend my thanks to the professional and administrative staff of the radiotherapy service of the cancer-fighting centre of Setif.

Special thanks to the teaching staff of the faculty of sciences of Ferhat Abbas-Setif1 University for providing me the fundamental necessary knowledge.

Finally, I wish to thank everyone who supported me.

CONTENT

Chapter I: External Radiotherapy

Chapter II: Quality assurance, quality control, and heterogeneity correction in external radiotherapy

Chapter III: Thermoluminescence Dosimetry

Chapter IV: Influence of wrong positioning of water phantom and ionization chamber on the accuracy of the treatment planning in external radiotherapy

Chapter V: Dosimetric control and comparison of 3D-CRT versus IMRT in the treatment of lung cancer

LIST OF FIGURES

Chapter I

Chapter II

Chapter III

Chapter IV

Chapter V

LIST OF TABLES

Chapter II:

Chapter III

Chapter IV

Chapter V

LIST OF ABBREVIATIONS

AAA: Anisotropic Analytical Algorithm
AAPM: American Association of Physicists in Medicine
CTV: Clinical Target Volume
DVH: Dose Volume Histogram
DVO: Dose-Volume Optimization
3D-CRT: 3D conformal radiotherapy
ESTRO: European Society for Therapeutic Radiation Oncology
FOC: Factors Opening Collimator
GTV: Gross Tumor Volume
IAEA: International Atomic Energy Agency
ICRU: International Commission on Radiation Units
IGRT: Image-guided Radiotherapy
IMRT: Intensity-Modulated Radiotherapy
MeV: Megaelectron-Volt
MLC: Multi-Leafs Collimator
MU: Monitor Units
OARs: Organs at Risk
OCR: Off-centre Ratio
PDD: Percentage Depth Dose
PMMA: Poly Methyl Meth Acrylate
PTV: Planning Target Volume
PTW: Physikalisch-Technische Werkstätten
SSD: Source to Surface Distance
TERMA: Total Energy Released per unit MAss
TL: Thermoluminescence
TLD: Thermoluminescent Dosimeters
TPS: Treatment planning systems

INTRODUCTION

Introduction

External radiotherapy (RT) is the most used treatment method in radiotherapy. It is called "external" because the radiation used for treatment is emitted from a source outside the body and passes through the patient's skin to reach the tumor tissue. High energy ionizing radiation is used in external radiotherapy to achieve the desired therapeutic effect. These radiations are, thus, able to change the structure of cells in order to damage and destroy cancer cells. Most external radiation treatments use photons (such as X-rays), but electrons and protons are also used. Photons and protons are used to treat deep cancers inside the body while electrons are only used for superficial cancers. Indeed, the clinician chooses the type of radiotherapy and the treatment device according to the type of cancer and its location in the body. There are different types of external radiation therapy which includes:

- ✓ 2D or 3D conformal radiotherapy (2D or 3D-CRT),
- ✓ Intensity-modulated radiotherapy (IMRT),
- ✓ Image-guided radiotherapy (IGRT),
- ✓ 4-dimensional radiotherapy (4D-RT),
- ✓ Stereotaxic radiotherapy (SABR) and radio-surgery (SRS),
- ✓ Adaptive radiotherapy.

Computerized treatment planning systems (TPS) are used in external radiation therapy to generate beam shapes and dose distributions that ensure optimal dose delivery to the patient by minimizing complications and side effects. Treatment planning systems are at the heart of radiation therapy and are the key for patient treatment outcomes improving. Once the image data sets are loaded and the tumors are identified, the systems develop a complex plan for each beam showing how the radiation therapy machine will deliver the prescribed dose. The TPS also calculates the expected dose distribution in the patient's tissues by including variables such as the penetration level of used beam in tissues which is influenced by the energy of the radiation and the type of tissue that the beam rays meet (bone, lung, muscular…). TPSs also help to choose the right ballistics avoiding the irradiation of critical structures and organs that are more sensitive to radiation. This is in order to reduce the collateral damage of radiotherapy. Treatment planning on TPS also includes complex and automated programming for sequencing the leafs of the multi-leafs collimator (MLC) of the radiotherapy machine (linear accelerator) to shape the beam around critical structures during the administration of the dose. Treatment plans can also be changed to compensate the effect of tumor size reduction during treatment.

Quality assurance (QA) in radiotherapy is the set of procedures which guarantee the consistency of the medical prescription and the safe fulfillment of this prescription. This includes administering the maximum of the prescribed dose at the target volume and a minimum dose to normal tissue, as well as minimal staff exposure and adequate patient monitoring. Quality assurance in radiotherapy concerns all aspects of the radiotherapy process which involves all groups of staff in a cooperative approach. Indeed, the fundamental objective of a quality assurance program in radiotherapy is to provide each patient with the best and safest radiotherapy treatment to obtain a cure, long-term tumor control, or palliation. Quality control in radiotherapy includes systematic controls of treatment planning system and dose administration parameters. Advice on appropriate methods, frequency of testing and levels of action for these controls comes from professional and scientific organizations and societies such as the International Atomic Energy Agency (IAEA) and the American Association of Medical Physicists (AAPM) . The establishment of a quality management plan in radiotherapy services is currently a requirement in all countries of the world.

QA programs that guarantee the safety and reliability of external radiotherapy are currently limited in their applicability to advanced radiotherapy techniques such as three-dimensional conformal radiotherapy (3D-CRT), intensity modulated radiotherapy (IMRT), reverse planning treatment, and stereotaxic radiotherapy. All these techniques present a high degree of complexity and great variations depending on the technique and the material used. Emerging high-tech radiation therapy techniques, such as image-guided external beam therapy (IGRT), adaptive radiation therapy, and motion-adaptive radiotherapy, require higher levels of automation and quasi-real-time execution of operations such operations such as automatic contouring, image registration, and treatment plans optimization making automatic QA procedures expensive and even more complicated. Thus, the application of one treatment technique in external radiotherapy in place of another with more complicated and costly QA should be done in an objective allowing access to better treatment benefits. The improvements brought by the new radiotherapy technique should be consolidated by comparisons in terms of administration of the dose to the target volume and critical organs at risk (OARs) sparing. These comparisons are generally to be consolidated by dosimetric measurements on a phantom before the application of the new technique on a patient which must be in full conformity with the quality assurance of the treatment.

Verification of the accuracy of the beam data used in radiotherapy planning is also part of the QA process. Tests on the variability of such data (accidental or not) on beam-specific calculations can help the user in case the differences between the measured and calculated doses are found outside the recommended criteria. These controls concern single-beam irradiation of water phantom under conditions close to those used for clinical trials during the commissioning of radiotherapy service. These controls have been designed so that the user can use the previously measured data. Comparisons can also be performed between measured doses and calculated ones by the TPS on selected points. The beam data checking includes the output factors, the field size and its penumbra and the doses at different points of the water phantom for a range of open or stuck field sizes.

In this thesis work, we are interested in the dosimetric comparison between 3D-CRT and IMRT radiotherapy techniques in order to justify the use of the latter for the treatment of certain types of cancer relatively complex in terms of localization and existence of wide heterogeneities such as the case of lung cancer. The dosimetric comparisons by thermoluminescence dosimetry and TPS calculation are made, in a quality assurance perspective, to demonstrate of the benefits on the patient to be treated. It was also a question to verify the impact of some plausible scenarios of wrong positioning of the beam data measurement equipments and instruments, namely: the water phantom and the ionization chamber on the accuracy of the treatment planning in external radiotherapy. This thesis project was carried out in the radiotherapy service of cancer fighting centre of Setif.

This manuscript is organized into five chapters: three are theoretical presenting the methods and techniques used and the two others are experimental presenting the results obtained as well as their interpretations. The first chapter is reserved to the presentation of external radiotherapy and treatment planning. The second chapter presents quality control in external radiotherapy and the heterogeneities correction methods. In the third chapter the principle of thermoluminescence dosimetry is spread out. The study of the influence of improper positioning of the water phantom and the ionization chamber on the accuracy of radiotherapy treatment planning is presented in the fourth chapter. Finally, in the fifth chapter, the results of the control and the dosimetric comparison between 3D-CRT and IMRT, for the case of lung cancer treatment are presented.

CHAPTER I :

External Radiotherapy

In this chapter

I.1 External Radiotherapy

External radiotherapy consists of the irradiation of benign or malignant tumors with ionizing radiation. It brings together all of the irradiation techniques where the source is placed at a distance from the patient to be treated. We also talk about Transcutaneous Teleradiotherapy. The treatment of cancer by external radiotherapy uses radiation of different energies. The most used types of radiation are photons and electrons, which interact with matter mainly by ionizing the atoms in their path (directly for charged particles or indirectly for photons). That's why that they are called radiation or ionizing radiation.

The interaction of radiation with atoms creates biological effects, which can lead to cell death. The ion produced in matter by radiation, has the capacity to damage DNA in two different ways:

1 The direct action breaks the molecule into two fragments. One of these fragments is a free radical possessing the capacity to produce a biological effect.

2 The indirect action is induced by the radiolysis of cellular water. The ionization of a water molecule produces free radicals which are the source of biological effects.

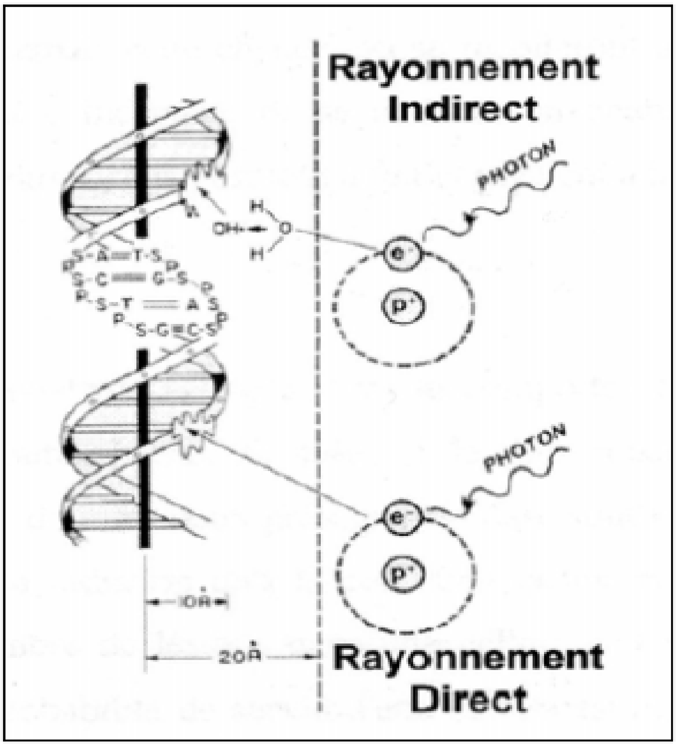

Figure I.1: Direct and indirect effects of radiation on DNA

The goal of external radiation therapy is to destroy cancer cells, modifying DNA, while preserving healthy cells as much as possible. Therefore, the precision with which the tumor is irradiated is essential.

External radiotherapy treatments are carried out using a linear particle accelerator or a telecobalt (practically no longer used). This particle accelerator is originally set to deliver a dose under reference conditions. From this and by fixing ballistics, there is a treatment planning tool (the Treatment Planning System, TPS) which allows the dose to be calculated at any point in space.[1]

I.2 Interaction radiation matter

In general, we can define radiation or radiation as a mode of propagation of energy in space, in the form of electromagnetic waves or particles. Radiation can only be detected and characterized by its interactions with the material in which they propagate. They can give in to the middle that they go through all or part of their energy during these interactions.

Radiation is said to be ionizing when it is capable of removing electrons from matter.

A more exhaustive definition is given: "ionizing radiation is a transport of energy in the form of particles or electromagnetic waves of a wave length less than or equal to 100 nanometers, or with a frequency greater than or equal to $3\text{x}10^{15}$hertz,capable of producing ions directly or indirectly. " The energy equivalent corresponds at 12.4 eV. Among these radiations, there are those which are directly ionizing, charged particles, those which are said to be indirectly ionizing because they are not charged. [2]

I.2.1 Different ionizing radiations

I.2.1.1 Direct ionization

They include light charged particles (electrons), and charged particles heavy (protons, α particles, and heavy ions) which deposit energy in the middle by a single step, through the process of Coulomb interaction between the incident particle and the orbital electrons [2].

I.2.1.2 Indirect ionization

They include neutrons and electromagnetic radiation (X and γ photons) which deposit energy in the middle by two steps [2]:

- At first, a charged particle is released in the absorbing medium (the photon releases an electron or electron / positron pair, and the neutron releases a proton or nucleus backward).

- In the second stage, the particles released deposit the energy in the absorbing medium by Colombian interactions with the orbital electrons of atoms.

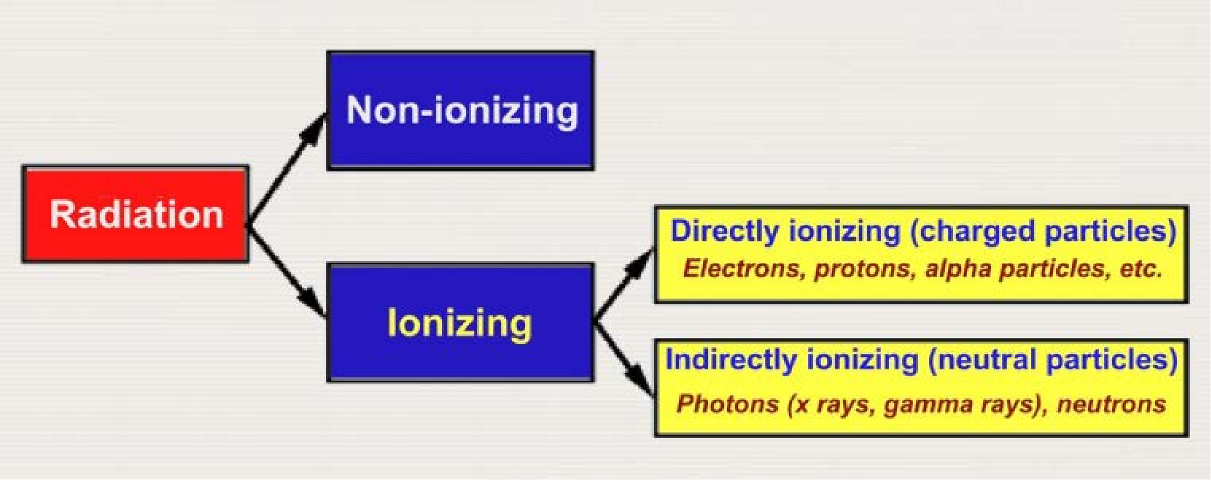

Figure I.2: Classification of radiation [3]

I.2.2 Electron interaction with matter

The rapidly moving electrons are obtained from:

- ✓ The radio-elements β emitters,
- ✓ The linear accelerators,
- ✓ The emission of secondary electrons after X or γ photons interaction.

Their kinetic energy is between a few keV and a few MeV.

Electron interactions can be divided according to the radius of the target atom (a) and the distance between the incident particle and the nucleus (b) of this atom in 3 categories: radiative collision, hard collision, and soft collision [4].

I.2.2.1 Hard collision (a≈b)

Electrons can have direct Colombian interactions with orbital electrons. The energy communicated to these electrons allows them to either:

- ✓ To move them from their level to a higher level (excitement),
- ✓ Or to eject with kinetic energy (ionization).

The number of hard collisions is generally low, but the energy transferred associated with this collision is relatively large (50% of the kinetic energy of the incident electron) (Figure I.3).

I.2.2.2 Soft collision (b≫a)

The incident electron is affected by the Coulomb force of the entire atom. The energy transferred to the orbital electrons is very low. However, the number of soft collisions is generally large.

I.2.2.3 Radiative collision (b≪a)

The electron interacts with the nucleus of the target atom and undergoes either elastic or inelastic diffusion, accompanied by a change in its direction. The majority of these interactions are elastic; where the electron only loses an insignificant amount of kinetic energy. However, a small percentage of these interactions are inelastic, where energy loss.

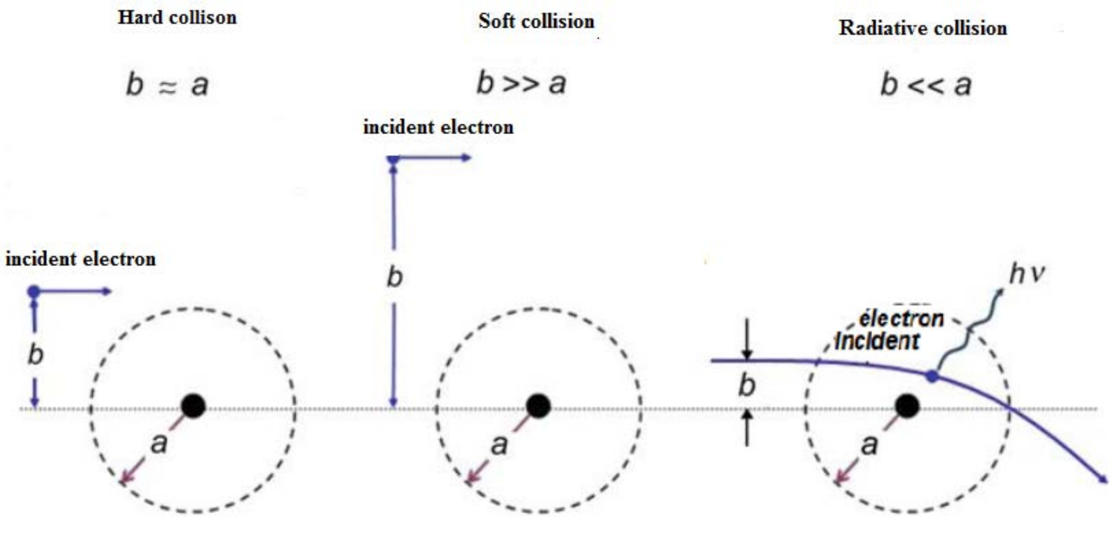

Figure I.3: The different collisions of light charged particles (electrons / positrons) with matter.

I.2.3. Indirectly ionizing radiation (photons)

The attenuation of a beam of photons by homogeneous matter is a phenomenon which is the consequence of several types of elementary physical interactions which lead either to a change of direction of the beam of photons (diffusion), or to a transfer of part of their energy to matter (total or partial absorption) [5].

I.2.3.1 Photoelectric effect

It is a phenomenon of total absorption. The incident photon disappears after giving all its energy to an electron from a middle atom. The ejected electron carries away kinetic energy E_k equal to the difference between energy $E_{h\upsilon}$ of incident photon and its bond energy W.

$$E_k = E_{h\vartheta} - W \qquad \text{(I.1)}$$

Following the expulsion of the electron by photoelectric effect, there is an electronic rearrangement with emission of fluorescence photons:

- ✓ Let photon X be for heavy atoms,
- ✓ Either of ultra-violet photons for light atoms.

The fluorescence photon can in turn expel a second electron from the atom; in this case it is said to be an Auger electron (Figure I.4) [3].

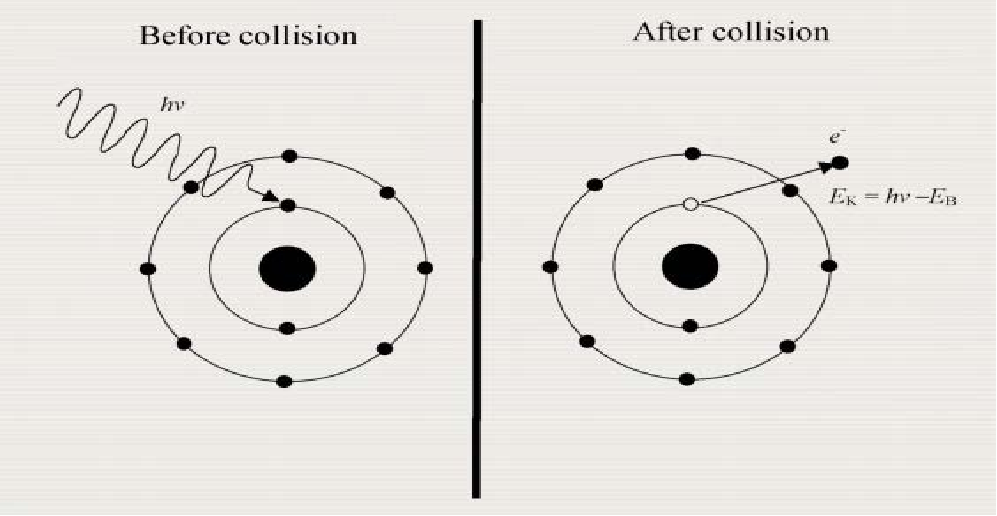

Figure I.4: Photoelectric effect

I.2.3.2 Compton effect

Compton scattering corresponds to a shock between an hv photon and a weakly bound valence electron. Le photon est alors diffusé avec une énergie inférieure à son énergie incidente $h\nu_0$ (with $hv_0 < hv$). The so-called recoil electron is ejected with kinetic energy E_k complementary to the energy of the scattered photon ($hv= hv_0+E_k$) and an angle Φ. This recoil electron can cause subsequent ionizations. The angle of diffusion of the recoil electron can be calculated using the following formula:

$$\Delta\lambda = \frac{h}{m_e c}(1-\cos(\phi) \qquad (I.2)$$

Where $\Delta\lambda$ is the difference in wavelength between the incident photon and the scattered photon, m_e is the mass of the electron (Figure I.5) [3].

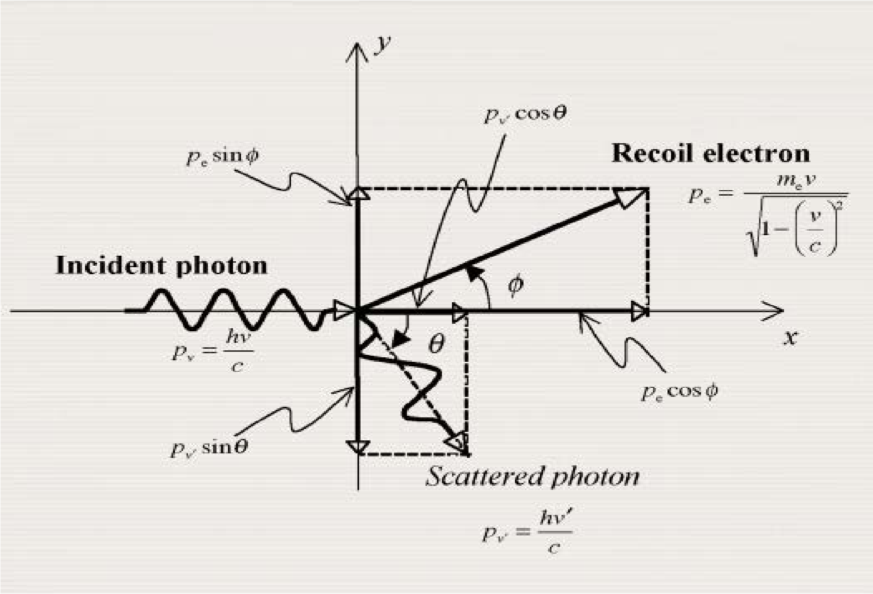

Figure I.5: Compton effect

I.2.3.3 Pair production

Pair production is a phenomenon that takes place near the field of the nucleus. In nuclear pair production:

- photon disappears, and

- ➢ an electron-positron pair with a combined kinetic energy equal to $h\nu - 2m_e c^2$ is created by the nuclear coulomb field (Figure I.6) [3].

Threshold energy for nuclear pair production is given by:

$$h\upsilon_{thr} = 2m_e c^2 \left(1 + \frac{m_e c^2}{M_A c^2}\right) \approx 2m_e c^2 \qquad \text{(I.3)}$$

Where: m_e is the electron mass, M_A is the mass of nucleus, and $m_e c^2 = 0.511$ MeV.

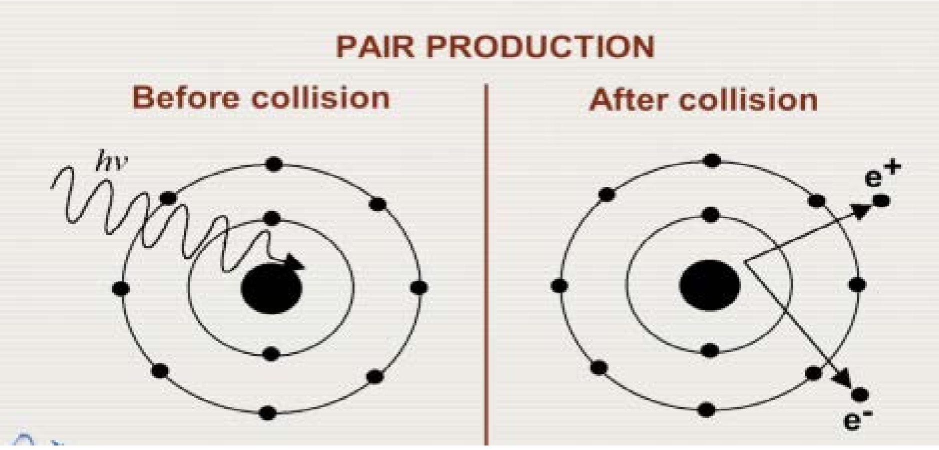

Figure I.6: Pair production [3]

I.2.3.4 Relative predominance of individual effects

Probability for a photon to undergo any one of the various interaction phenomena with an atom of the absorber depends:

- On the energy $h\nu$ of the photon,
- On the atomic number Z of the absorber.

In general:

- Photoelectric effect predominates at low photon energies.
- Compton effect predominates at intermediate photon energies.
- Pair production predominates at high photon energies (Figure I.7) [3].

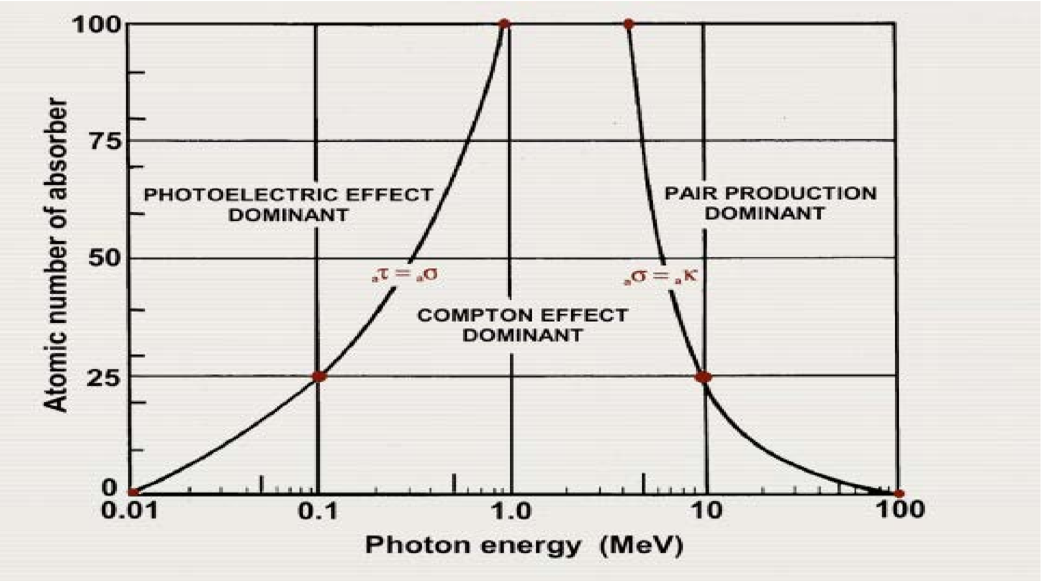

Figure I.7: Regions of relative predominance

I.3 Different Treatment Techniques

There are different techniques of external radiotherapy. Technological advances have made it possible to better protect tissues and organs at risk while delivering a therapeutic doseoptimal for processing the target volume. Indeed, today all of the treatments are based on computed tomography images.

I.3.1 Conformational Radiotherapy

The term "conformational" means "close to the shape or configuration of a structure". 3D conformal radiotherapy is a transcutaneous irradiation in which the treated volume is adapted to the target volume reconstructed in 3 dimensions (Figure I.8). The objective of this radiotherapy technique is to decrease the dose delivered to the healthy tissues surrounding the tumor, to increase the dose in the tumor and to obtain better local control, thus increasing patient survival. At present, the implementation of this technique calls for:

- means ensuring the reproducibility of the treatment (immobilization of the patient, restraint, etc.);

- three-dimensional imagery of all the irradiated volumes (CT scan possibly supplemented by MRI, PET, and image fusion, etc.);

- delineation of target volumes and critical organs to which appropriate safety margins are applied;

- ballistics and personalized collimation of the beams (personalized caches, multileafs collimators (MLC)) determined from a three-dimensional calculation of the distribution of doses in the different volumes (GTV, CTV, PTV, organs at risk);

- control of the reproducibility of the treatment (portal imaging, radiography) [6].

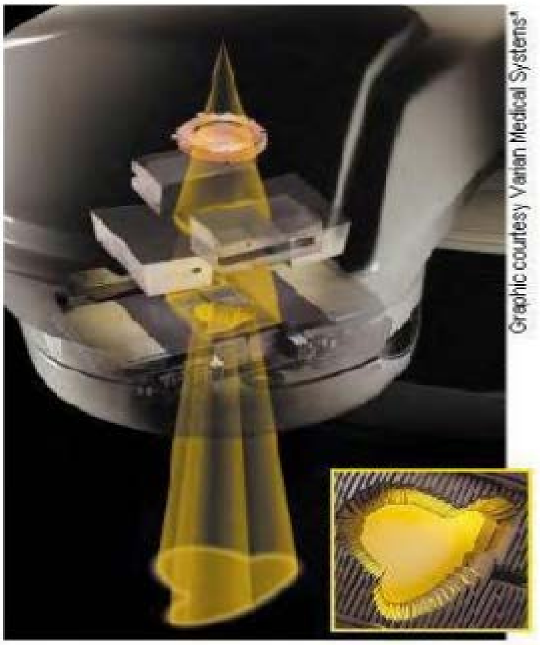

Figure I.8: Fields conform to the structure

I.3.2 Intensity-Modulated Radiation Therapy (IMRT)

I.3.2.a.Definition and Interest of IMRT

Intensity-Modulated Radiation Therapy (IMRT) can be defined as a voluntary spatial variation of the photon fluence, applied to the different points located inside the irradiation field (FigureI.9 (B)). This fluence modulation is performed during the same treatment session of the patient. In order to define this modulation, the fluence of the field is then discretized into small volume elements called bixels (for "beam elements"). Each bixel is associated with a weight which can be either a fraction of the dose obtained in open beam, or a number of monitor units (MU) [7]. The dimensions of each bixel determine the spatial resolution of the intensity modulation and the number of possible intensity levels for each bixel determines the resolution in intensity [8].

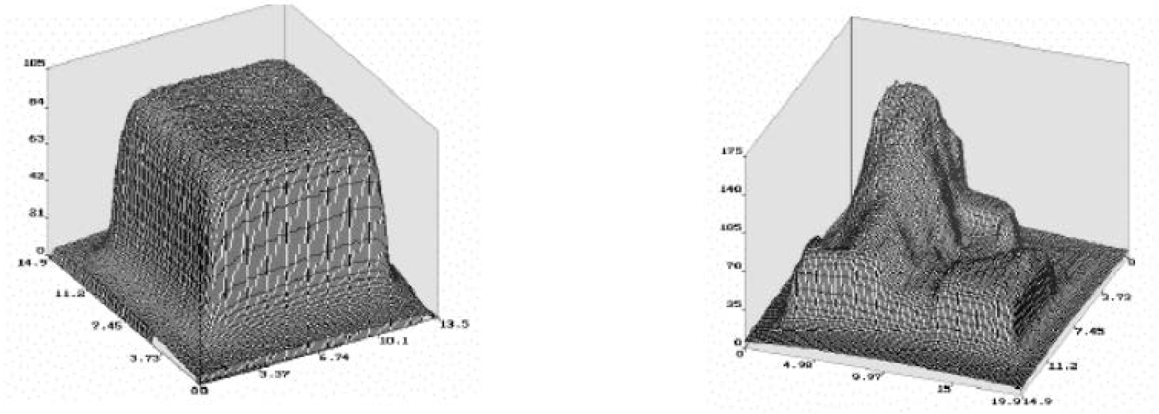

A

B

Figure I.9: A.: Example of a homogeneous field obtained in conformational technique and B.: Example of a modulated field obtained in IMRT for the treatment of ORL cancer [7]

Thus, thanks to the modulation of the intensity inside the irradiation field, the IMRT makes it possible to adjust the absorbed dose in depth so that the high isodoses are all confined within the tumor volume and s " adapt perfectly to shape complex of it. This gives IMRT two major advantages over 3D-CRT [9]:

1. The possibility of increasing the dose in the tumor area (target volume), thus resulting in a potential gain in efficiency (better local control);

2. The possibility of reducing the dose in healthy tissues close to the tumor, thus leading to a gain in tolerance (better overall tolerance of the treatment, fewer complications) [10-11].

I.3.2.b Modulation of static and dynamic intensity

- ✓ **Static mode"step-and-shoot":** It is about the superimposition of fields of complex shapes with discontinuous displacement of the blades and stop of irradiation of the beam between two movements of the blades (static segmental mode). Figure (I.10) shows schematically how the fluence map of a beam segmented into a level map is obtained. Each of the segments is applied with the number of Monitor Units (MU) calculated [12].

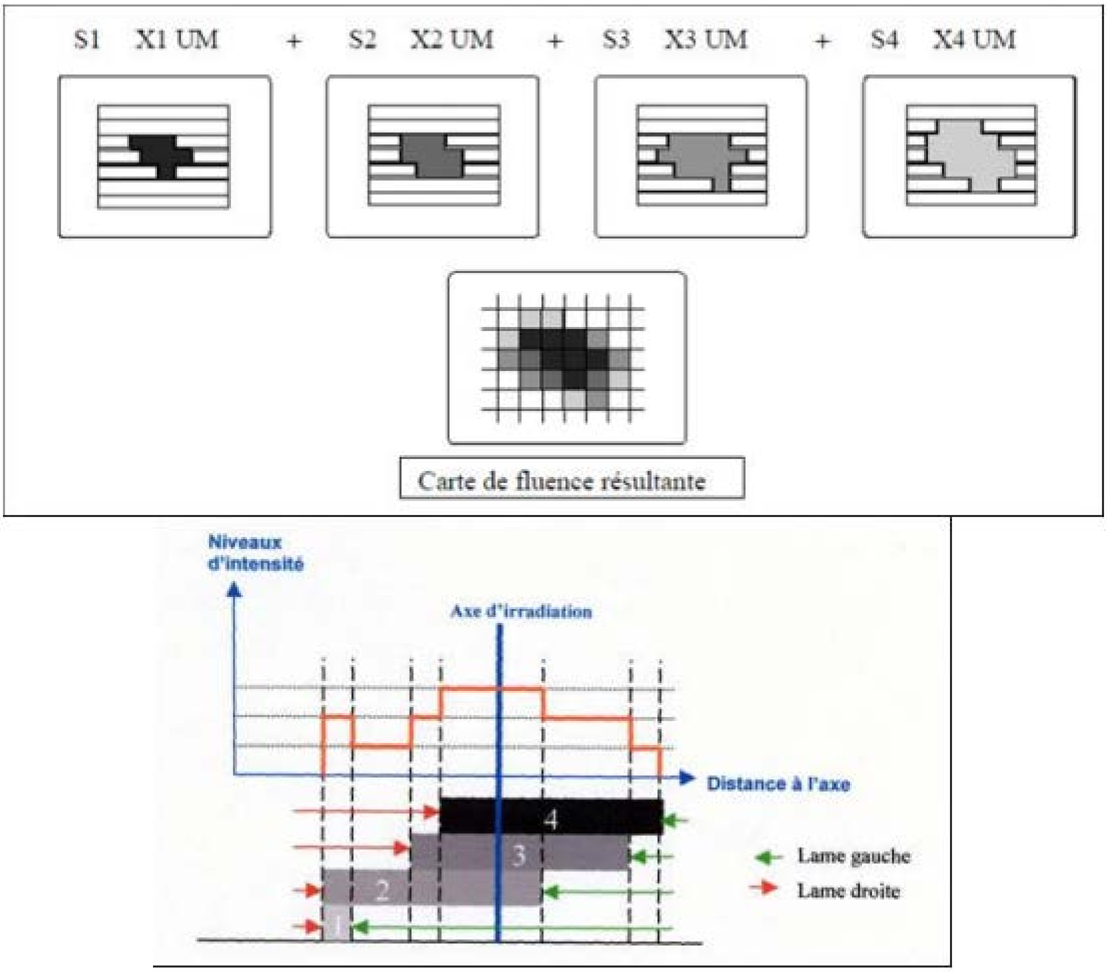

Figure I.10: Principle of obtaining intensity modulation in static mode, superposition of four segments generating four intensity levels.

- ✓ **Dynamic mode "sliding window":** During an intensity modulation by sliding blades ("sliding window"), the blades of the MLC move continuously during the irradiation, with control and synchronization dose rate and slide speed. The movement of each of the blades is done independently and at variable speed. The radiation emission is continuous during the displacement of the blades. The blades move in the same direction. The treatment begins with all the blades positioned on the same side of the field to be produced (for example on the left). Then the blades of right open at variable speed depending on their position relative to the axis. Their opposites (those on the left) move at the same time at variable speed to close the beam (Figure I.11) [12].

✓

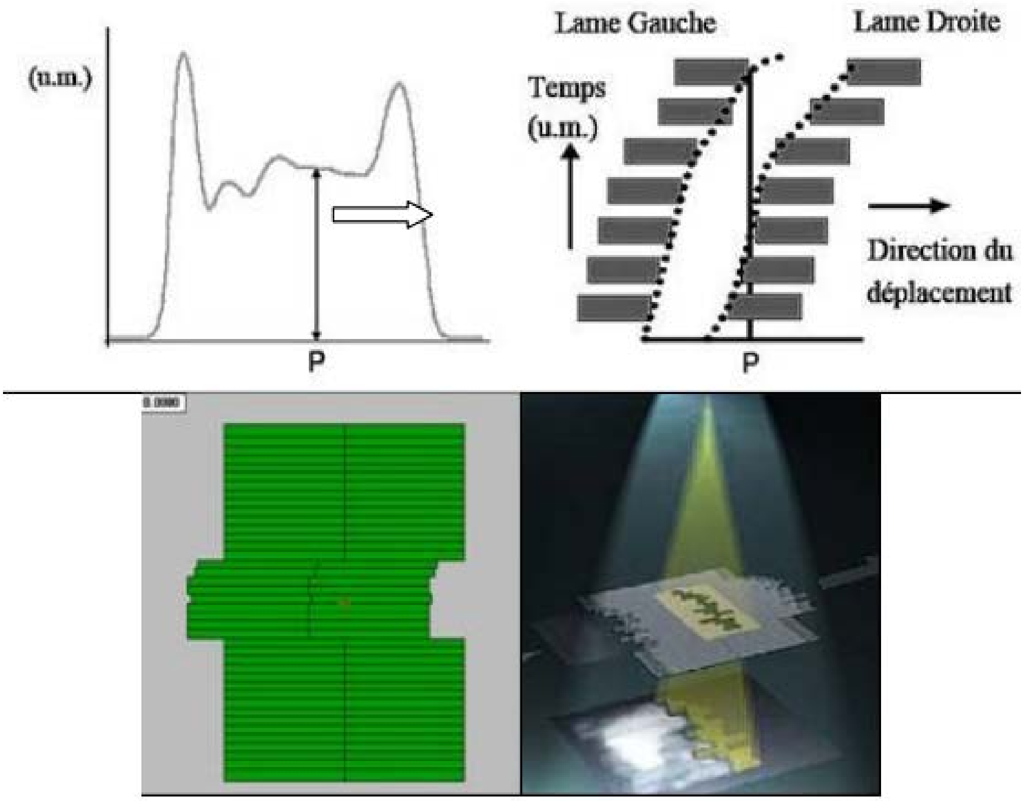

Figure I.11: Principle of obtaining intensity modulation in dynamic mode

I.3.2.c Problems related to the use of multileafs collimator MLC

The physical problems generated by the mechanical and geometric constraints of multileafs collimator (MLC) are managed in a diverse and more or less effective way in the planning systems marketed currently. Generally, they are compensated by the introduction of additional dosimetric parameters.

- **Transmission:** In intensity modulation, the number of monitor units useful for delivering the prescribed dose is higher than in conventional mode.

In static mode, the transmissions linked to each segment are added, thus increasing the proportion of the dose relating to the transmission of the collimator.

In dynamic mode, the problem is further accentuated by the fact that a point in the area to be irradiated most of the time passes under the blades. The transmission varies, depending on the energy, the size of the field, the position of the field relative to the axis and the depth of measurement. Some calculation systems use two transmission values: the main transmission and a dosimetric offset (additional transmission) linked to the rounded shape of the blades of certain collimators which adjusts the calculated and measured dose distributions. Others consider only an energy transmission value. In this case, an average value of this transmission under reference conditions [12].

- **Focus**: In most MLCs, the front of the blades is not focused, which leads to a mismatch between the light field and the irradiated field which is more important as their position moves away fromthe axis. This irradiated field / light field offset is corrected by the manufacturers.

In addition, the flare of the front of the blades of certain MLCs increases the transmission on the edge of these and the penumbra. This phenomenon, of low incidence for static fields, becomes nonnegligible for dynamic irradiations because its effect is distributed over the entire width of the irradiated field [12].

- **Lateral profile of the leaf:** In order to limit leaks between the adjacent blades, the blades fit into each other in a "tenon and mortise" mode. In static intensity modulation, this particular geometry can cause under dosing at the junctions of 2 adjacent segments (Figure I.12). This type of junction is avoided by certain sequencers.

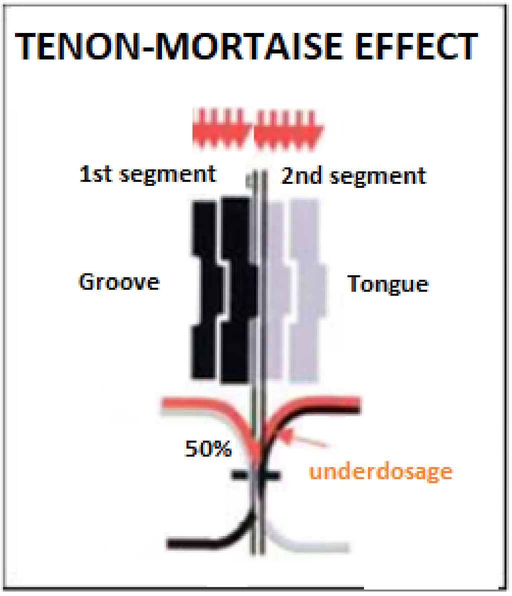

Figure I.12: Diagram of the Tenon-Mortaise effect in static mode.

In addition to the Tenon-Mortaise effect described above, when the speed of the adjacent blades is different, the distance between the angles of the opposite blades each belonging to a pair different is then less than the distance between the blades of each of the pairs (Figure I.13), it creates a sub-dosing zone. The synchronization of the blades reduces the amplitude of this effect but to the detriment of the quality of the modulation [12].

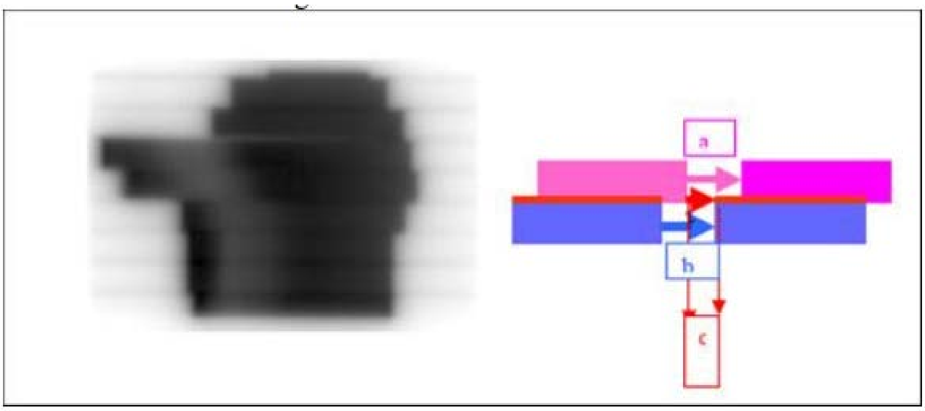

Figure I.13: Tenon-Mortaise effect in dynamic mode not synchronized.

- **Leafs position accuracy:** In static mode, only the isodoses of the edge of the segments are affected by a positioning error as well as the dose in the center for small segments. In dynamic mode, a blade positioning error results in a modification of the spacing between the opposite blades and induces a dose difference over the entire irradiated field since the blades cross the entire field during irradiation [12]. A 1mm error on a 1cm window can lead to a dose variation of 10% (Figure I.14).

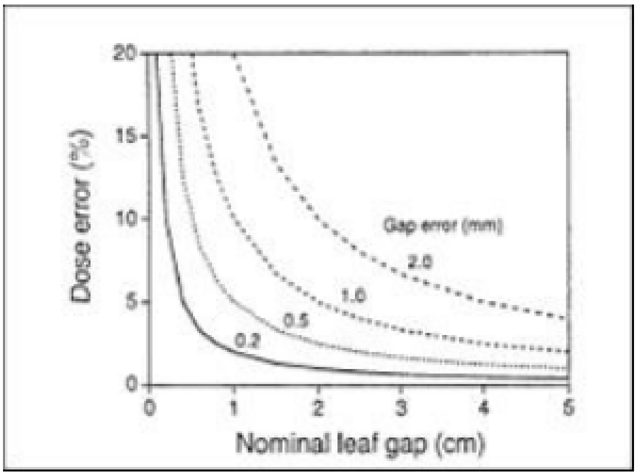

Figure I.14: Influence of a positioning error of the MLC leafs on the dose delivered in dynamic mode

- **Leafs movement speed:** In static mode, the speed of movement of the blades has no particular effect on the dose distribution. On the other hand, in dynamic mode, a stable blade speed will lead to a uniform intensity profile while a variation in the speed of the blades during irradiationintroduce profile level fluctuations [12].

I.3.2.d Reverse planning

Reverse dosimetry is a predictive dosimetry procedure, the starting point of which is based on the clinical objectives imposed by the radiotherapist (dose to tumor and OAR), the computer calculating the irradiation parameters necessary to achieve these objectives, hence its name of reverse dosimetry (Figures I.15 and I.16). In conventional predictive dosimetry, the dose to the tumor and to the OARs represents the final objective and not the starting point of the treatment plan (Figures I.15 and I.16) [13].

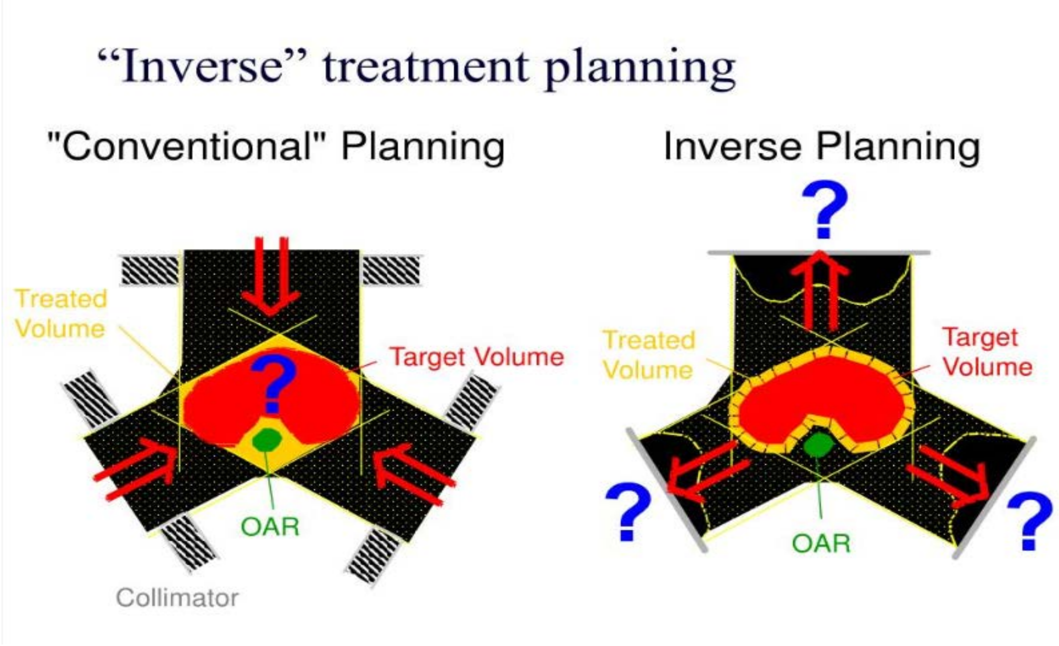

Figure I.15: Conventional direct planning on the left and indirect planning by intensity modulation on the right [14]

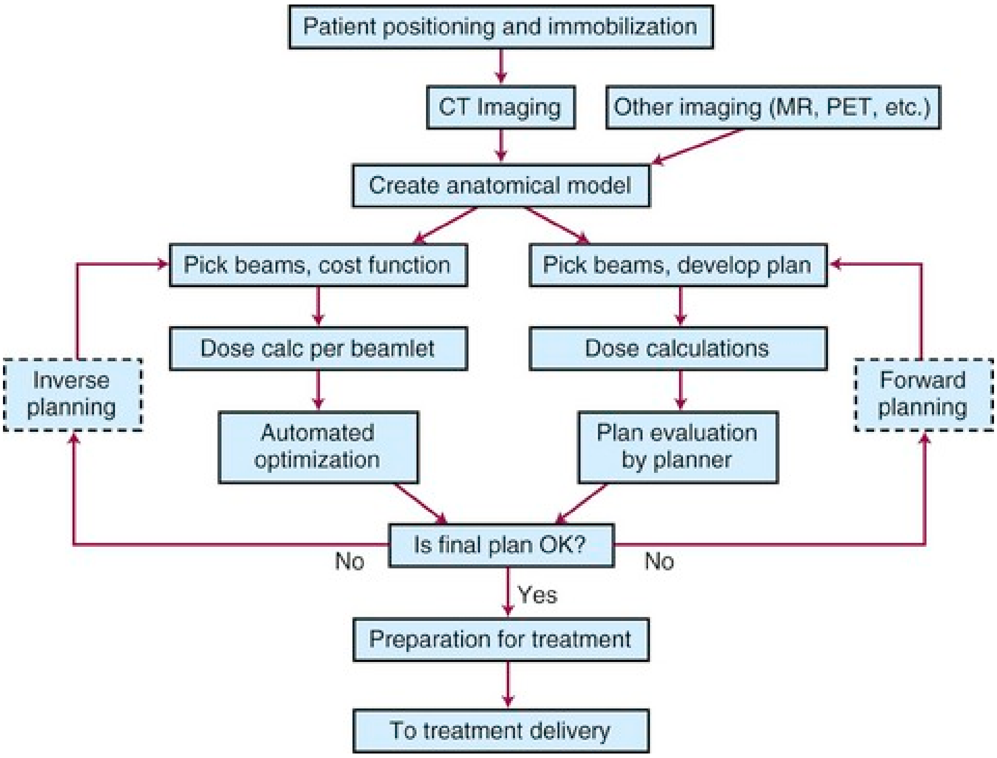

Figure I.16: Diagram representing the direct and indirect planning process [15]

The reverse optimization process is the first step in planning specifically for intensity modulation. The previous steps of acquiring anatomical data, determining interest structures and setting up ballistics are identical to standard conformational processing.

For clinical use of intensity modulation, it is essential to know how to pose the problem and how to adjust the optimization parameters so that the treatment plan conforms to what is desired.

Reverse planning programs generally include a dose calculation algorithm combined with an optimization method (optimization on intensity modulation) [13]. Based on dosimetric objectives and optimization constraints, the

TPS calculates the modulation of each of the beams to be applied to obtain the desired dose distribution. It builds and minimizes a mathematical expression called "objective function" which we will detail later.

Ideally, the reverse planning system should optimize all of the processing parameters. Most reverse planning software calculates the intensity modulation to be applied to each of the beams so as to obtain the desired dose distribution. But because of the very high computation time, the systems do not carry out, to date, of optimization on energy, the number, the orientation and the geometry of the beams. These parameters are always dependent users and must be optimized manually.

I.3.2.e The objective function

To calculate the dose distribution which must correspond to that prescribed dose, it is necessary to translate the dosimetric (or clinical) objectives by a mathematical expression called objective function. Its most frequent representation is by a quadratic expression translating the difference between the distribution of current dose and prescribed dose:

$$F = \alpha \sum_{i \in Target\ volume} (D_i\,(x) - D_p\,)^2 \ +\ \beta . \sum_{i \epsilon\ organ\ at\ risk} (D_i\,(x) - D_t)^2 \qquad \text{(I.4)}$$

Where: *Di (x)* is the dose calculated at point *i* for all the modulated profiles *x*, *Dp* is the prescribed dose to target volume and *Dt* is the dose tolerated by organ at risk.

The first term of this expression translates the distribution in the target volume and the second the dose distribution in the OARs. When the constraints are not respected a penalty is introduced. These are the factors α and β. To evaluate the result of this function, criteria are necessary, and are of 2 types: physical or biological.

Most systems are based on physical criteria. These optimization criteria or constraints are in the form of minimum dose (*Dmin*) and maximum dose (*Dmax*) not to be exceeded for the target volumes and *Dmax* to be respected for OARs. Indeed, such criteria apply mainly to target volumes but also to OARs which have a threshold reaction (the spinal cord for example). For the organs which rather show significant volume effects (the lungs for example), criteria on the dose – volume relationship have been introduced, they are of the type: *x*% of the volume must not receive a dose greater than *y* Gy [13].

I.3.2.f. IMRT optimization algorithms

Optimization algorithms consist of two elements:

- ✓ The objective function which groups together the clinical objectives to be achieved during the planning and which gives a numerical score to the plan obtained,
- ✓ The optimization algorithm which will minimize this objective function.

Optimization algorithms can be divided into two main groups: inversion methods (mathematical methods) and iterative methods (deterministic or stochastic). The optimization methods used are generally iterative. Their choice is mainly based on the number of beams and the nature of the constraints depending on whether they are of the dosimetric type orbiological. Each of these methods comes from a "modeling / dose calculation / profile determination method" association, correlated with a set of compromises made during all the stages, in order to simplify the system tosolve and / or reduce calculation times.

Iterative optimization methods are subdivided into two types, deterministic methods and stochastic methods:

- The first type is a process in which a history always produces the same effect.
- The second type is a process which, for a given antecedent, can produce several effects, each with a determined probability. Stochastic processes are the subject of statistical analysis.

A. Determinist methods

Among the deterministic methods, we can distinguish:

- Linear programming algorithms such as the Simplex algorithm which traverses the convex polyhedron formed by the linear constraints of the problem by optimizing the cost function (also linear).
- Numerical gradient methods which are based on the determination of the derivative of the cost function or an approximation of the derivative (by linearization) and possibly successive derivatives like the Newton method (and quasi-Newton).

A.1 Simplex algorithm

The method is deterministic (even if its initialization can be random). George Dantzig's simplex algorithm is a technique that is both fundamental and very popular for linear programming problems. Thus, given a set of linear inequalities on n real variables, the algorithm makes it possible to find the optimal solution for an objective function, which is also linear.

In geometric terms, the set of linear inequalities defines a polyhedron in n-dimensional space and it is a question of finding the optimal vertex for the given cost function. In the search for the optimal vertex, the simplex algorithm can take aexponential calculation time.

However, the simplex algorithm is very efficient in practice and it is implemented in all linear program solvers, and in particular for the computation of the displacements of the CML blades in dynamics.

This algorithm does not seem the most effective for our reverse planning problem, indeed too many parameters are to be programmed which makes the task extremely difficult with this type of algorithm.

A.2 Gradient technique

The technique of finding the optimal solution by the gradient method is the most commonly used in radiotherapy because one of its main features is its speed of obtaining an acceptable solution. As mentioned above, the optimization process will seek to cancel the value of the objective function, that is to say in other words to search for the variable constituted by all of the modulated beams (grouped in the variable x) which cancels its derivative:

$$F_{obj}(x)_{min} = \nabla F_{\mathrm{obj}}(\mathrm{x}) = 0 \qquad \text{(I.5)}$$

In its simplest form, the search for x, constituted by the bixels of the set of beams will be done according to the following relation [73]:

$$X^{k+1} = X^{k} - a\nabla F_{\mathrm{obj}}(\mathrm{X}^{\mathrm{k}}) \qquad \text{(I.6)}$$

Where, *k* indicates the iteration and has the size of the search step (variable or not).

The gradient of the objective function at iteration k can be expressed in the form:

$$\nabla F_{\mathrm{obj}}(\mathrm{X}^{\mathrm{k}}) = 2\left[\alpha.\textstyle\sum_{i\in Target\ volume}(D_i\,(x) - D_p\,)\ +\ \beta.\textstyle\sum_{i\epsilon\ organ\ at\ risk}(\,D_i\,(x) - D_t)\right] \qquad \text{(I.7)}$$

The iterative process by the gradient method is shown in Figure (I.17). The starting point is x^0. As iterations progress, the value of the objective function decreases to reach the minimum at the third iteration. When the starting point is badly located, optimization can lead to a local minimum of the objective function. The very principle of finding the optimal solution using the gradient technique prevents the process from extricating itself from this local minimum. Therefore, the optimization result is not optimal. The use of gradient search therefore involves a risk of finding a sub-optimal solution, it is then necessary to have recourse to stochastic search methods.

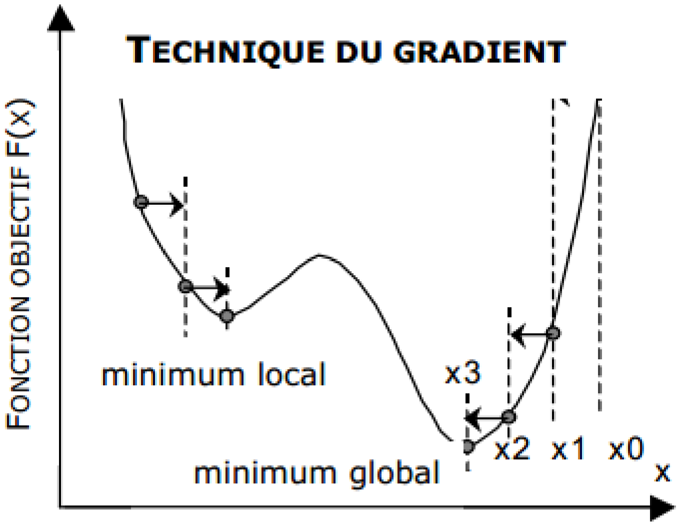

Figure I.17: The Gradient technique

An optimization of this technique is therefore sought. A significant improvement in the investigation of the optimal solution can be obtained by the use of conjugate gradient methods. In this algorithm, the direction taken for the next iteration takes into account the direction used in the previous iterations. Thus, the optimal solution is reached much faster. Knowing that the modulated profiles obtained by this technique are complex and can contain digital artefacts, their practical realization is sometimes difficult to achieve. Spirou et al. [13] have therefore developed a methodology to smooth beam profiles. They compared two techniques: the first is to smooth the profiles at each iteration of the optimization process. The second method consists in including a term in the objective function specifying the smoothing of the profiles as if it were an additional optimization criterion. The results showed that the second method was more efficient during optimization, since it required a lower number of iterations. On the other hand, it is less advantageous for dynamic irradiation because it generates a longer irradiation time [13].

B. Stochastic methods

Unlike deterministic algorithms, stochastic optimization algorithms incorporate random mechanisms for exploring the search space. These methods have the advantage of determining the global optimum, but the speed of convergence is lower, however their use is more suitable in the presence of constraints of biological type.

B.1 Simulated annealing

The simulated annealing method is a stochastic search method for the optimal solution, which was first developed by Metropolis et al. (1953), then applied to optimization by Kirkpatrick (1983); many variations exist. The solution space will be traversed by carrying out more or less important research steps (probability function) and the solutions found are preserved with a probability all the more important that they show a gain in optimization. Simulated annealing reproduces the way a thermal system with large number of degrees of freedom reaches a stable state when its temperature decreases slowly [13]. The analogy with reverse planning is found in the fact that we will randomly modify the weights of each elementary beam to achieve a stable equilibrium where the calculated dose distribution is equal to the prescribed dose distribution.

The advantage of this method is that it makes it possible to traverse the whole space of the solutions and to avoid stagnating the optimization process in a zone of local minimum as could the systematic optimization of the gradient (FigureI-18) [13]. However, if the optimization only relates to the weightings of the elementary beams, and not to the number and the angulation of the beams, the local minima can be considered as close to the overall minimum value and the results are entirely satisfactory [13].

Ideally, an infinite number of iterations is necessary to find the absolute minimum.

Consequently, in practice with a finite number of iterations, the best solution among all those examined will be retained. The quality of this solution will be much closer to the optimal solution that the number of iterations will be important which will require computing times all the more important. Despite these drawbacks, the simulated annealing method is used clinically [13].

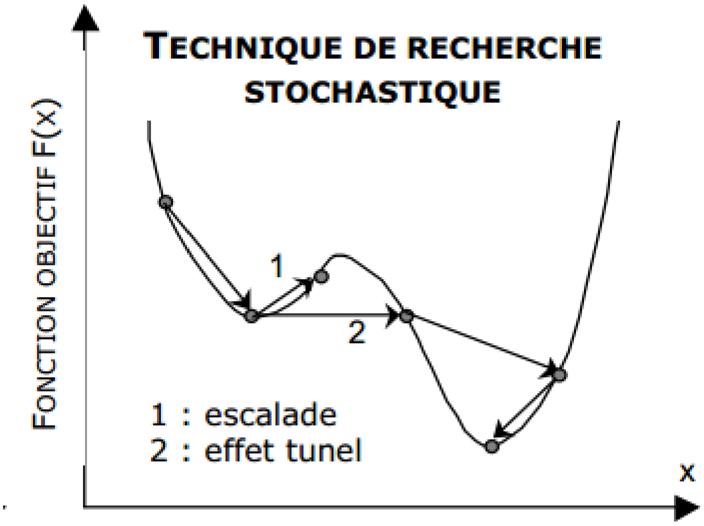

Figure I.18: Simulated annealing

B.2 The genetic algorithm

Genetic algorithms propose a stochastic technique alternative to simulated annealing. They are based on a natural process: the evolution of a population through natural selection. Genetic algorithms therefore take up Darwin's theory. The first step in the process is to create the initial population of individuals by randomly assigning 0 to 1 relative weights of bixels. Then each individual is evaluated, that is to say that a value of "quality" is assigned to them. From an objective function, this allows to classify the individuals. Then a selection of individuals is made. The fourth step in the process is the random modification of the population or individuals by overlapping (crossing of portions of individuals), cloning (duplication of the best individuals), mutation (change of a few bixels), creation of spontaneous generation, deletion, death of individuals (Figure I.19). The spontaneous generation of individuals or the mutation of some of them will allow, in particular at the end of optimization, to ensure a sufficient diversity of individuals to allow a sufficiently broad search for the optimal solution [13].

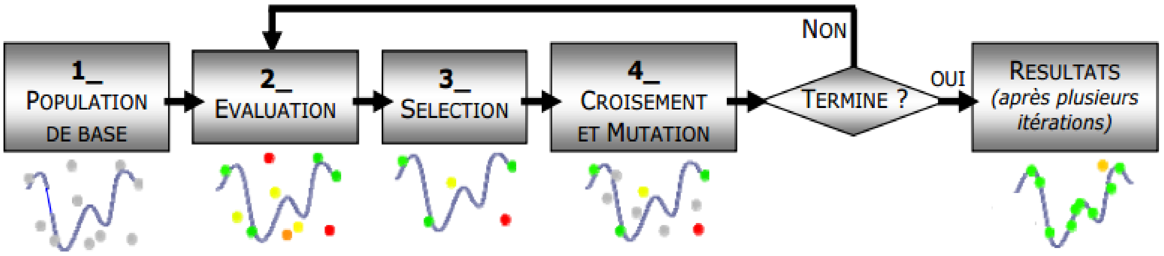

Figure I.19: The genetic algorithm

I.3.3 Stereotaxic radiotherapy

Stereotaxic radiotherapy (Figure (I.20) and (I.21)) is a very high precision image guided radiotherapy technique which allows:

- ✓ Deliver very high doses of radiotherapy in small volumes,
- ✓ To carry out so-called "radio-ablative" treatments, which destroy the tumor,
- ✓ To spare nearby healthy organs [16].

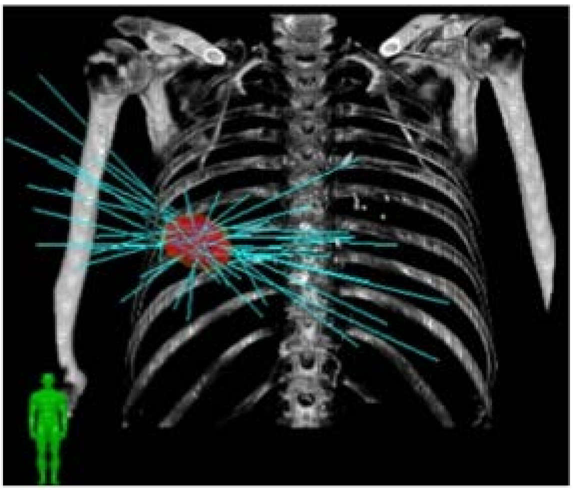

Figure I.20: Example of Cyber Knife treatment for lung cancer

Its main indications include:

For intracranial tumors:

- ➢ Brain metastases,
- ➢ Meningiomas,

- Acoustic neuromas.

For extracranial tumors:

- Small lung cancers, without affected lymph nodes and without metastasis in patients too fragile to be operated or who refuse surgery
- Metastases in so-called "oligometastatic" patients, that is to say who at most three metastases with a primary disease have controlled elsewhere:
  - Bones,
  - Pulmonary,
  - Hepatic.
- Prostate cancer in patients who cannot or do not wish to be operated on. It can be performed exclusively or as a boost of conformal radiotherapy,
- Inoperable hepatocellular carcinomas,
- Reirradiation of ORL, pelvic, etc. cancers [16].
-

Figure I.21: Cyber Knife stereotaxic radiotherapy system [17]

I.4 Steps of external radiotherapy treatment

I.4.1 Medical consultation

This consultation, the first contact between the radiotherapist and the patient, should be a privileged moment to inform the latter of the different therapeutic orientations proposed, expected benefits, possible side effects and therapeutic risks that these treatments entail. It is important to adapt the explanations to the patient and to ensure their understanding in order to provide fair, clear and appropriate information for that the patient gives informed consent to the initiation of treatment [18].

I.4.2 Treatment Simulation

Simulation is the first step in the radiotherapy journey. This is the preparation for treatment stage. It takes place between 2 and 7 days before the start of irradiation (Figure I.22). During the simulation, the patient is placed in the treatment position, generally lying on his back, using a means of restraint adapted to the location of the lesion to be irradiated and to the treatment machine (Figure I.23). For example, if the lesion is at the level of the thorax, the patient's arms will be placed above the head in order to separate them from the treatment beams. If the tumor is located at the level of the ORL sphere or the brain, the patient will benefit from the placement of a thermoformed compression mask to guarantee the reproducibility of the positioning [18].

Figure I.22: Patient undergoing a scanner simulation session. The patient is placed in a restraint system which will be used after the treatment.

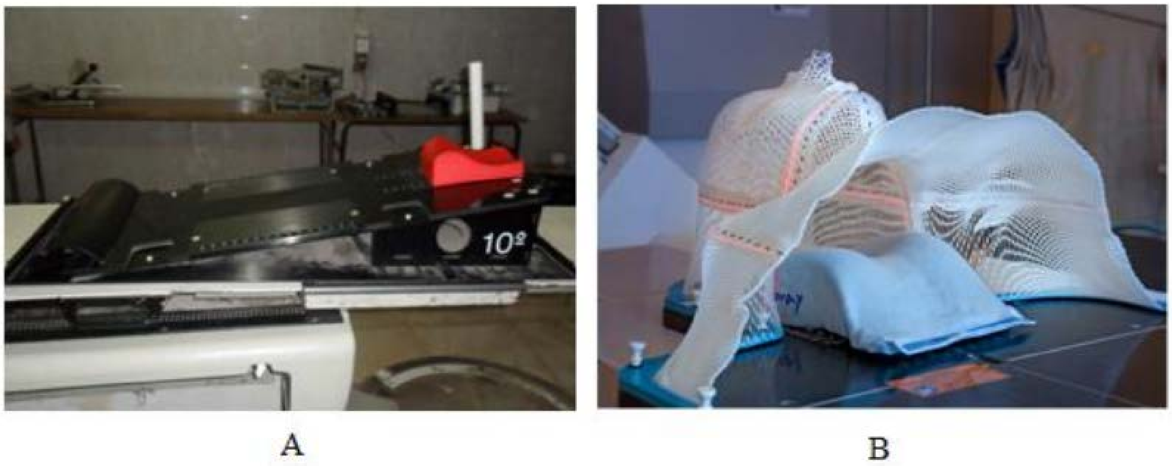

Figure I.23: Means of restraint, A: inclined plane, B: thermoformed mask.

Then, we proceed to the acquisition of anatomical data by imagery via a scanner dedicated to radiotherapy. Sometimes it is useful to inject a contrast medium to facilitate the delimitation of the areas to be irradiated and to differentiate the vessels from other structures (for example, the ganglionic structures). As soon as a comfortable and reproducible position is defined, we tattoo the patients at precise reference points. These points are find at the intersection of laser beams that represent the three axes of the Cartesian space (x,y,z). The treatment rooms are equipped with this same laser device which therefore allows positioning during processing with millimeter precision. Information concerning the type of compression, the position of the various elements of this compression and the position of the patient are also recorded on an individual file which will follow the patient throughout his treatment.

I.4.3 Definition of target volume and Organs at Risk

The definition of target volumes and organs at risk is also a preparatory step for irradiation. She is often called "contouring". In reality, on each section of the scanner acquired during the simulation, the different volumes (to be treated and avoided) are delimited. This meticulous work is the responsibility of the radiotherapist and is carried out on a computerized planning system. The Treatment Planning System (TPS) allows 2D visualization (section by section) and 3D reconstruction of the volumes of interest.

The contouring of the target volumes is done according to the recommendations of the International Commission on Radiation Units (ICRU). We mainly define three target volumes: GTV, CTV and PTV. GTV (Gross Tumor Volume) or gross tumor volume includes all measurable, palpable or visible tumor lesions on imaging. The second, the CTV (Clinical Target Volume) or anatomoclinical target volume includes the GTV to which a margin corresponding to the microscopic extension invisible to imaging is added. This margin comes from literature data illustrating the possible microscopic extension described by pathologists beyond what is macroscopically visible.

Finally, the PTV ("Planning Target Volume") or forecast target volume includes the CTV to which a safety margin is added corresponding to the positioning uncertainties of the patient as well as the "mechanical" uncertainty specific to the machine. In some cases, we also define an ITV ("Internal Target Volume") or internal target volume instead of a CTV, which takes into account the physiological movements of the organs. We will then move from ITV to PTV. Going through an ITV considerably increases the volumes to be treated. In order to reduce this volume, and thus reduce the risk complications in healthy tissue, so-called "gating" and "tracking" techniques are used in radiotherapy. In the principle of "gating", the patient's breathing is controlled by the machine while, for "tracking", the machine must adapt to the movement respiratory. From the acquisition of the initial imagery during the simulation, so-called 4D techniques (addition of the time factor in the acquisition) will be used to allow "gating" or "tracking" to execute the processing.

The organs at risk are also defined and then, can start the treatment planning phase, also called predictive dosimetry [18].

I.4.4 Treatment planning approval

The planning stage is the penultimate stage prior to effective treatment by dose delivery. It is a question of imagining the treatment best suited to the patient while respecting dose constraints for organs at risk. This stage is carried out by the physical team of the service composed of a dosimetrist and a medical physicist who will work in concert with the radiotherapist. The treatments are delivered by machines called linear accelerators. In order to deliver a homogeneous dose to the entire tumor and protect the critical organs, the dosimetrist and the physicist must find the right combination of converging beams. They will therefore iteratively vary dimension, position and weighting to optimize the distribution of the dose.

The iterative optimization process is limited by the time required for this process and by the limits of the human mind to imagine different possible combinations.

In the 1990s, “Intensity-Modulated Radiation Therapy” (IMRT) radiation therapy was developed. It's about a radiotherapy in which the fluence of the beams is modulated during treatment using the multi-blade collimator. Therefore, an optimization performed by the dosimetrist is no longer conceivable given the multitude of modifiable parameters. In this case, a reverse dosimetry. It consists in "imposing" dose targets for volume and dose constraints for organs at risk. The reverse planning software then performs iterative calculations, based on the objectives and constraints set. It adjusts, at each iteration, the combination of the different technical parameters to converge towards the expected end result. These iterations continue until the specified dose criteria are met.

As soon as the planning is complete, this forecast dosimetry will be discussed with the radiotherapist. When several treatment options ensure the same degree of tumor coverage, the choice is made in favor of the plan which saves the better the organs at risk. We will also take into account the ease of execution of the processing because this has a connotation, on the one hand, of security and quality of execution and, on the other hand, of responsible use of human and technical resources. In order to compare qualitatively and quantitatively different plans possible, we will use a tool called DVH (“Dose Volume Histogram”). This tool is a graphical representation of the distribution of the dose at the level of the various target or non-target tissues. At the risk organ level, it makes it possible to assess the probability of the acute and late effects of radiotherapy. The ideal objective is to deliver 100% of the dose homogeneously in 100% of the target volume and 0% of this dose in the adjacent organs. Risk factors for complications of healthy tissue are known and closely depend on the volume irradiated, the total dose and the dose per fraction. Dose constraints have been described which should not be exceeded in order to reduce complications in healthy tissue. This tolerance dose depends on the dose distribution and the architecture of the organ. There are two types of organs: organs with tissue structure in series and organs with tissue structure in parallel.

In tissues with a serial structure (spinal cord, digestive tract, nerves), the destruction of a subunit of the organ alters the whole function of this organ. A high dose in a small volume is toxic.

The tolerance dose is represented by the maximum dose delivered to a few cm^3, i.e. 2-3% in the volume of the organ at risk. This is called the D2 of *x*Gy, which means that the dose received by 2% of the volume of the organ must be less than or equal to *x*Gy. For tissues with parallel structure (lungs, kidneys, liver), the organ consists of independent subunits between them. The function is then altered when a certain number of subunits is destroyed. The tolerance dose depends on the dose distribution within the organ and is expressed as follows: V*x* less than or equal to y%. This means that the dose of *x*Gy should not be delivered in more than y% of the volume of the organ at risk. We also speaks of average dose for the average of the point doses calculated by calculation software in each element of the volume of the organ at risk.

All data relating to the patient's treatment is transmitted in a secure and computerized manner. In this potentially paperless universe, some paper documents persist for verification. [18].

I.4.5 Effective treatment and dose delivery

Once started, the treatment is delivered daily except in special cases, and this, weekends. During the first three days of treatment, the patient's position is checked by a portal imaging system on the linear accelerator. This device makes it possible to compare the planning images from the calculation software and obtained by digital reconstruction from the simulation scanner with the images being processed. A comparison of planar (2D) or solid (3D) images allows positioning control and correction of systematic errors if it takes place. Then, during the treatment, this repositioning check is carried out once a week. The images are analyzed by technologists and approved by the radiotherapist. During treatment, consultations are carried out weekly by the radiotherapist. They aim to appreciate the clinical tolerance on a general level (weight, fatigue, general condition) and on a regional level (appearance of acute local complications). The patient is also supported by psychologists and advised on dietetics by a consulting nurse [18].

I.5 General Description of linear radiotherapy accelerator

The accelerators used for the treatment of cancers by radiotherapy are linear accelerators (Linac) of electrons emitting ionizing radiation of energy greater than Mega-electron-Volt (MeV). The accelerated electrons can be directly used for the treatment of superficial or semi deep tumors (skin cancer, chest wall after mastectomy, etc.), or they can interact with a material of high density to produce mainly by braking radiation of high energy X-rays (from 4 to 25 MV) for the treatment of deep tumors (prostate, lung cancer, etc.) [19].

The electrons are produced by thermo-electronic effect from a cathode which is composed of a spiral tungsten filament brought to high temperature by Joule effect. The emitted electrons are focused in a beam brush by a wehnelt or concentration electrode. The action of a pulsed electrostatic field accelerates the electron beam towards the anode, drilled in its center to allow the passage of electrons. The assembly constitutes an electrostatic accelerator which is called electron gun (Figure I.24). The electrostatic field used to accelerate the electrons is provided by a pulsed modulator acting on the cathode of the gun. The electron beam thus created escapes from the barrel and enters the accelerating section formed by several cavities (Figure I.25) where it will undergo a succession of accelerations until it obtains the kinetic energy desired.

These accelerations are produced by high frequency electromagnetic waves or microwaves (≈ 3 GHz) supplied by a klystron or a magnetron (Figure I.26). The pulsed modulator also intervenes on the microwave generator which ensures synchronization between the electromagnetic wave and the electrons which are sent in packets in the tube of acceleration. The latter consists of several cylindrical cavities which allow the electrons to be in phase with the electromagnetic wave to overlap it throughout of the tube. An auxiliary pump generates vacuum in the accelerating section until a pressure of around 10^{-6} Torrs is reached to allow a free propagation of the electrons. This is done at a slight angle to the horizontal axis of rotation of the accelerator arm. The electron beam must then be deviated from its path to come hit the target and produce x-rays that will escape from the accelerator's head through the crosshairs. Beam deflection is ensured by electromagnets positioned inside the electron transport system from the accelerating section to the target (Figure I.27) [19].

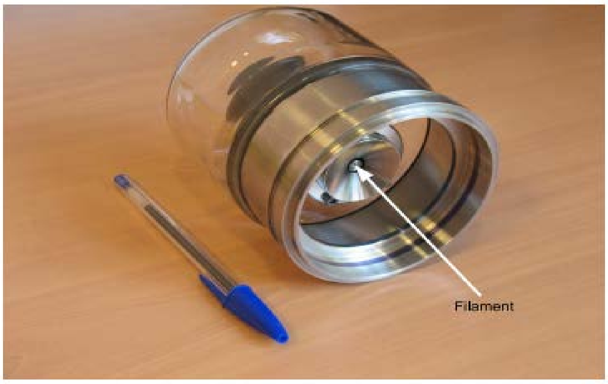

Figure I.24: Electron gun of a Philips SL75/5 type accelerator

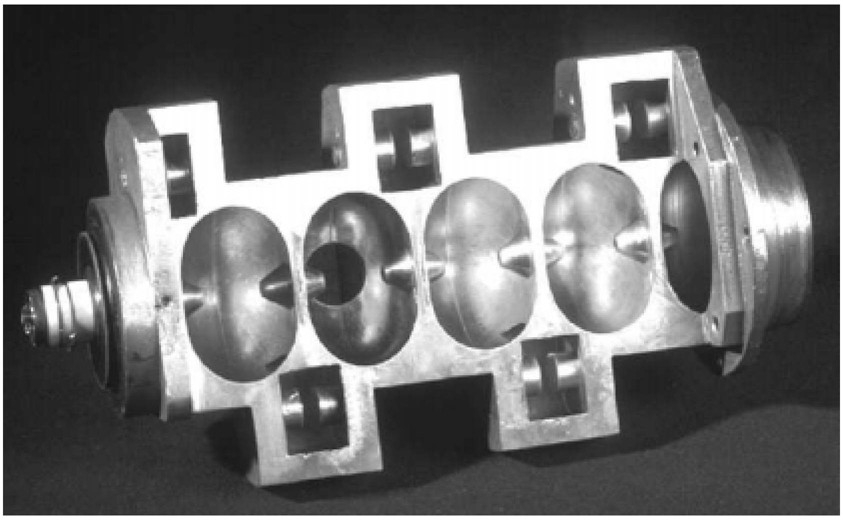

Figure I.25: Axial section of the accelerator section of a 6 MV accelerator

Figure I.26: Magnetron, seen from the front, of an accelerator type SL75 / 5 from Philips

X-rays are produced by the interaction of accelerated electrons with the target of the accelerator’s head. This produces two types of X-ray: characteristic X-ray (or fluorescence) and Bremsstrahlung X-ray (or braking radiation) [19].

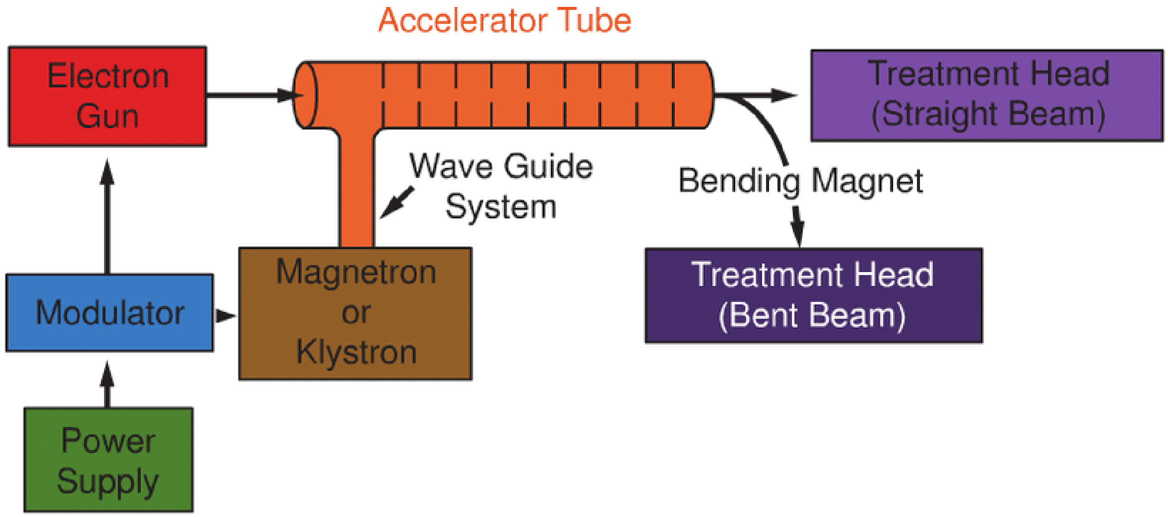

Copyrigth 2010 Wolters Kluwer Healt | Lippincott Williams & Wilkins

Figure I.27: Diagram-of-a-typical-medical-linear-accelerator [20]

The accelerator head consists of the following elements (Figure I.28):

- **The target** allowing the production of X photons by braking radiation and characteristic emissions;

- **The primary collimator** surrounding the target and delimiting a conical exit beam;

- **The vacuum window** providing the interface between the vacuum inside the primary collimator and the air of the rest of the irradiation head;

- **The equalizing cone** to standardize the dose in the irradiation field. The cone is a function of the energy (or rather of the accelerating voltage) of the photon beam used;

- **The monitor chambers** continuously measuring the output dose rate of the device as well as the symmetry and homogeneity of the beam. Two rooms are present in order to level onepossible malfunction of one of them;

- **The mirror** reflecting the light of a bulb making it possible to visualize the treatment field by a light beam;

- **The jaws X and Y** ensuring the secondary collimation in order to produce square or rectangular fields;

- **A multi-leafs collimator** (MLC) enabling a complex form of irradiation to be produced, more in line with the shape of the target volume;

- **TheMylar plate** comprising the reticle allowing to materialize the central axis of the light beam [21].

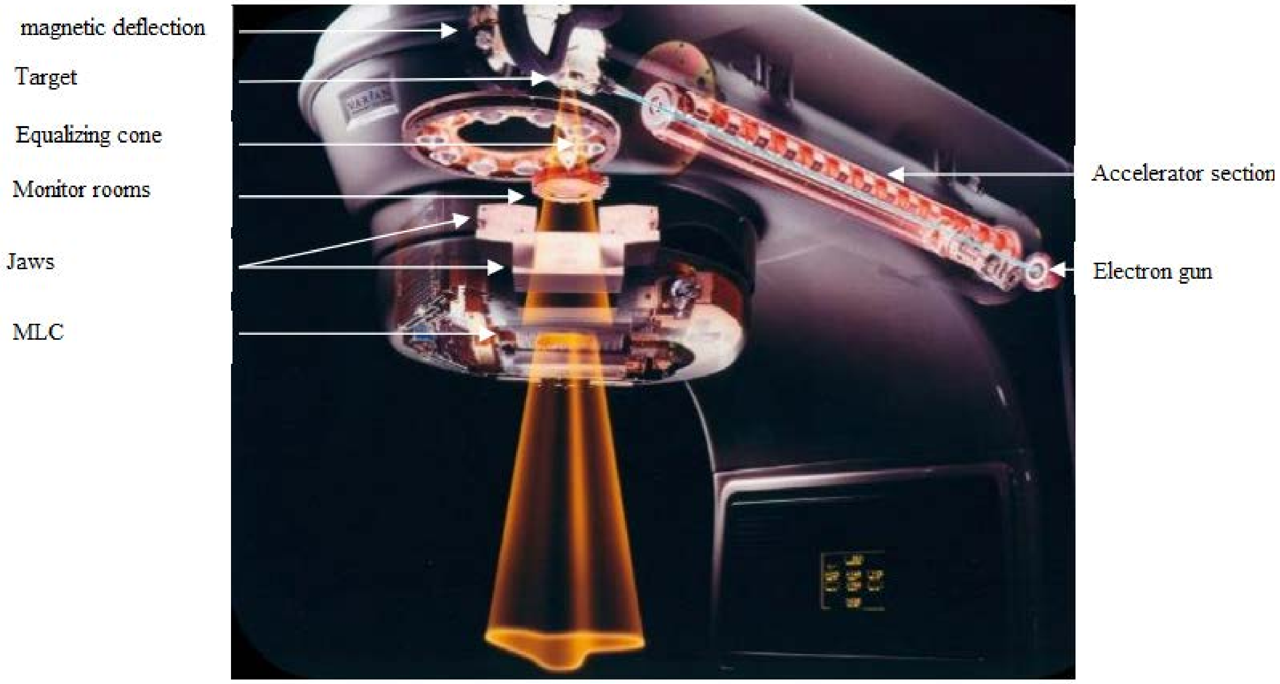

Figure I.28: Diagram of the Varian CLINAC 2100C linear electron accelerator

References

[1] *Modelisation et validation de la version 7.4f du TPS (Treatment Planning System) PINNACLE* : https://cyrilvoyant.pagesperso-orange.fr/Pinnacle_7.4.pdf, Accessed 25 March 2019.

[2] International atomic energy agency, *Radiation oncology physics: a handbook for teachers and students,* ISBN 92–0–107304–6, Vienna, 2005.

[3] E.B. Podgorsak, *Chapter 1: Basic Radiation Physics Slide set of 195 slides based on the chapter authored by of the IAEA publication*: *Review of Radiation Oncology Physics*: *A Handbook for Teachers and Students*. ISBN 92-0-107304-6.

[4] Ervin. B. Podgorsak, *Radiation Physics for Medical Physicists*". Edition: Springer, 2éme edition (2010), ISBN 978-3-642-00874-0.

[5] Russell K. Hobbie, Bradley J. Roth, I*ntermediate Physics for Medicine and Biology*. Edition: Springer, 4éme edition (2007). ISBN-13: 978-0-387-30942-2.

[6] L Meherchi, *Système de double calcul dosimétrique*. Mémoire de master, Université Aboubakr Belkaid, Tlemcen, 2011. : http://dspace.univ-tlemcen.dz/handle/112/318

[7] Chauvet I, *Contrôle de qualité et mise en œuvre d'un logiciel de planification inverse pour la radiothérapie conformationnelle avec modulation d'intensité*. Thèse de Physique Radiologique et Médicale: Ecole doctorale GEET - Université Paul Sabatier - 2004, Toulouse, France.

[8] Rosenwald J.C., Gaboriaud G., et al., *la Radiothérapie Conformationnelle : principes et classification*. Cancer Radiother, 1999,Vol. 3(5): p. 367-377.

[9] H.A.S (Haute Autorité de Santé), *Radiothérapie conformationnelle avec modulation d'intensité*. www.has-sante.fr , 2006, Accessed 14 October 2019.

[10] Adams E.J., Nutting C.M., et al., P*otential role of intensity-modulated radiotherapy in the treatment of tumors of the maxillary sinus*. Int J. Radiat. Oncol. Biol. Phys., 2001, Vol. 51(3): p. 579-588.

[11] Cozzi L., Fogliata A., et al., T*hree-dimensional conformal vs. intensity-modulated radiotherapy in head-and-neck cancer patients: comparative analysis of dosimetric and technical parameters*. Int J. Radiat. Oncol. Biol. Phys., 2004, Vol. 58(2): p. 617-624.

[12] Contrôles de qualité en radiothérapie conformationnelle avec modulation d'intensité, Rapport SFPM N° du 26 Janvier 2010. http://documents.sfpm.fr/docs_sfpm/sfpm_2010-26_assurance-qualite-rcmi.pdf.

[13] Fleur Kubs, *Apport de la modulation d'intensité et de l'optimisation pour délivrer une dose adaptée aux hétérogénéités biologiques*. Thèse de doctorat en Traitement du signal et de l'image. Institut National Polytechnique de Lorraine - INPL, 2007. https://tel.archives-ouvertes.fr/tel-00182354.

[14] https://www.slideserve.com/jena-sykes/image-reconstruction-and-inverse-treatment-planning-sharpening-the-edge-thomas-bortfeld. Accessed 11 January 2020.

[15] Conformal Therapy and Intensity-Modulated Radiation Therapy: Treatment Planning, Treatment Delivery, and Clinical Results, Oncohema Key. https://oncohemakey.com/conformal-therapy-and-intensity-modulated-radiation-therapy-treatment-planning-treatment-delivery-and-clinical-results/. Accessed 11 January 2020.

[16] La radiothérapie stéréotaxique : http://www.radiotherapie-hegp.fr/index.php/cancer-traitement/la-radiotherapie-externe?id=67. Accessed 11 January 2020.

[17] UNICANCER - Inauguration du système de radiothérapie stéréotaxique CyberKnife® au centre François Baclesse de Caen : http://www.unicancer.fr/actualites/actualites-centres/inauguration-du-systeme-de-radiotherapie-stereotaxique-cyberknife%C2%AE-au-centre-francois-baclesse-de-. Accessed 11 January 2020.

[18] La radiothérapie : le parcours du patient, de l'information au traitement : https://orbi.uliege.be/bitstream/2268/165470/1/LA%20RADIOTH%C3%89RAPIE-%20le%20parcours%20du%20patients%2C%20de%20l%27information%20au%20traitement.pdf. Accessed 20 March 2020.

[19] Contrôle dosimétrique des traitements de radiothérapie par simulation Monte Carlo de l'image de dose portale transmise : https://www.creatis.insa-lyon.fr/~dsarrut/phd/JeanNoelBadel_PHD_2009.pdf. Accessed 20 March 2020.

[20] https://www.researchgate.net/figure/A-block-diagram-of-a-typical-medical-linear-accelerator-46_fig14_260887128. Accessed 20 March 2020.

[21] Nicolas Garnier, *Simulation d'un accélérateur linéaire d'électrons à l'aide du code Monte-Carlo PENELOPE : métrologie des traitements stéréotaxiques par cônes et évaluation de l'algorithme eMC* : https://tel.archives-ouvertes.fr/tel-02272122. Accessed 14 April 2020.

CHAPTER II:

Quality assurance, quality control, and heterogeneity correction in external

In this chapter

II.1 Quality assurance and quality control in external radiotherapy

II.2 Dose calculation and heterogeneity correction in external radiotherapy

II.1 Quality assurance and quality control in external radiotherapy

II.1.1 Quality assurance of the TPS

The treatment planning system TPS is a key element in the radiotherapy treatment planning process. Its precise and stable operation conditions the safety of treatments and their success, hence the absolute need to set up a quality assurance program at the level of all stages of treatment planning performed on the TPS. Before tackling the different aspects of quality assurance (QA), it is important to quote and define rigorously certain terms.

Quality Assurance in radiotherapy [1]: all procedures whose objective is to verify that:

- The dose at the target volume respects the medical prescription,
- The dose to healthy organs is at the lowest possible level,
- The exposure of the personnel is minimal,
- Patient monitoring is operational.

Quality Control (QC): this is the process by which the performance of a system is measured and compared to the standards in force. It includes all of the actions necessary to maintain or regain system compliance with standards. It is part of global quality assurance and has the following objectives [1-2]:

- ✓ Check that the quality requirements are met,
- ✓ To adjust and correct the initial performances in case of drift.

The overall objective of these concepts is to ensure that the clinical quality requirements of a radiotherapy treatment are met: to target an optimal treatment by maximizing the probability of tumor control, while maintaining a dose of healthy tissue within the limit clinically acceptable levels. The implementation of a quality assurance program will minimize errors and reduce possible accidents.

The quality control of the TPS must make it possible to verify the conformity of their performance, to monitor any drift in the initial performance and to know the limits of validity of the software used on these systems.

In general, the QC is integrated into the life cycle of a TPS [1-2]: upon receipt, during commissioning and during routine clinical use, covering all stages of the planning of the treatment, from the anatomical definition to the calculation of the dose. Reference documents for this quality control have been drawn up successively by various commissions and reports: AAPM 1995 and 1998, ESTRO 2004, IPEMB 1996, IAEA 2004, 2007 and 2008, NCS 1997 and 2006, and SSRMP 1997, SFPM 2010 report. We will detail their respective contents later.

II.1.1.1 Acceptance testing of TPS

These are test procedures implemented upon receipt and installation of the TPS to ensure that it conforms to the specifications given by the manufacturer [3-4]. No measurement at this stage is necessary; it is only a qualitative assessment.

The TPS acceptance tests concern the verification:

- ✓ The equipment (screen, central unit, etc.) and its proper functioning,
- ✓ From the network (transfer of CT images to TPS, export of treatment plans, etc.),
- ✓ Basic features of the TPS:
    - ➢ Reading of CT images and other modalities (MRI, PET…),
    - ➢ Anatomique description (external contours, anatomique structures, etc.),
    - ➢ Description of the radiation beams,
    - ➢ Dose calculation (use for example the basic data supplied with the accelerator),
    - ➢ 2D / 3D display (BEV, HDV ...).

II.1.1.2 Commissioning of TPS

This is the set of procedures required before clinical use, in the event of installation or major upgrade of the TPS. These procedures must cover all dosimetric (dose calculations) and non-dosimetric (image acquisition, contouring of organs, definition of beams, etc.) possibilities of the TPS. It is the most critical and time consuming and expert step. It can take several weeks or even several months before being completed [5].

The "commissioning" includes:

a. The configuration of the device library that will be used routinely from basic data measured in specific situations, hence the need to verify that the TPS is capable of accurately calculating this basic data. For this it is recommended to compare the basic data measured to supply the TPS with those calculated by the latter,

b. The implementation of specific tests and procedures to determine the accuracy of the TPS in dose calculations and to identify its limits [3-4].

II.1.1.3 Periodic TPS checking

QA does not end with the commissioning of the TPS. QC tests performed periodically must be implemented to confirm the integrity of the input / output devices used (imaging systems, transfer software to the TPS, software to transfer data to the R&V system and then to the device …) and to verify the consistency and reproducibility of the dose calculations protecting the user against any accidental drift induced for example by a minor update or patch [3-4].

II.1.2 State of the art on the dosimetric QC methods for the TPS

The TPS regroup virtual simulation consoles allowing the optimization of the treatments from the geometric point of view, and the dosimetry consoles which optimize the dosimetric treatments. The different reports described below distinguish two classes of tests, the 1st to assess the geometric performance and the second to assess the dosimetric performance. Most QC procedures for dose calculations are based on comparisons between data calculated by the TPS and the reference data obtained for test configurations ranging from a simple variation in the size of the radiation field to the use of anatomical ghosts.

We recall below the definition of some terms common to all reports dealing with the subject:

- The basic data: these are the mostly experimental data (yields, profiles, etc.) that characterize a clinical beam of irradiation in the TPS; they feed the algorithm deployed on the TPS so that the latter can perform dose calculations.

- Reference data: this is data designed to be used as reference data in order to test the TPS. In general, they are provided with the corresponding uncertainties.

- Tolerance: is defined in booklet N°7 of ESTRO as the maximum acceptable difference between a calculated physical quantity (to be evaluated) and measured (reference).

In our case (dosimetric QC) it can be expressed as a percentage dose deviation in areas of low dose gradient, or a spatial deviation in distance in areas of high dose gradient [6]. There are comparison tools like the Gamma-index which can mix these two deviations; in this case the tolerance is 1 because it is based on acceptability criteria including tolerances in dose and distance.

QC methods can be classified according to the origin of the reference data:

- Reference data obtained by experimental measurements:
    - ✓ locally under the service processing devices
    - ✓ generics from a reference center and made available to other centers
- Reference data obtained by numerical simulations using a Monte Carlo code locally adapted to the treatment devices of the service.

II.1.3 Dosimetric QC using measured reference data

II.1.3.1 Reference data measured locally

In this method it is not necessary to measure additional basic data other than those already in place within the TPS and for tested beams to commissioning because these data are the same as those used for treatments. It consists in making comparisons between dose calculations carried out by the TPS to be tested and dosimetric reference measurements, for certain test cases, carried out under the processing devices of the service. Baseline data vary in complexity and generally attempt to be representative of current clinical situations.

The following bibliographical references that we will present in this section are for the most part the reports of national or international commissions responsible for defining methods QC or more generally dealing with QA in radiotherapy.

1. AAPM Report No. 62 (1998)

In this document the "Task Group" N°53 (TG-53) of the AAPM (American Association of Physicists in Medicine) develops the QA to be implemented in radiotherapy (in photons and electrons modes) and in brachytherapy [7]. The TG-53 distinguishes dosimetric QA from non-dosimetric QA, provides the full description of the tests to be performed in each case and issues recommendations on their frequency. At the "commissioning" stage, the AAPM recommends checking:

- the basic data implemented in the TPS by ensuring that the TPS is capable of accurately reproducing the dose distributions included in the basic data,
- Dose calculations in the TPS by implementing simple, intermediate and complex tests more or less close to clinical situations.

TG-53 gives an exhaustive list of tests to reproduce experimentally in the TPS to verify the dose calculation; this list is summarized in (Table II.1) in the case of photon beams. Each radiotherapy center must adapt this list according to its needs and means.

The calculated and measured dose distributions are normalized with respect to the calculated or measured dose at the reference depth under reference conditions (10 × 10 cm² irradiation field defined at the isocentre). The reference depth chosen by AAPM (1998) is the maximum dose depth. The tool to be used to compare the results obtained is the relative dose difference.

In this report, the AAPM suggests some evaluation and acceptability criteria depending on the tests and the region of interest (Table II.2).

Table II.1: Summary of the various tests for the photon beams in report 62 of TG-53

0. Verification of basic data

- TPR[1] and TMR[2] for several openings: 5x5, 10x10, 20x20, 30x30 and 40x40 cm²
- “Outputs factors[3] (SSD[4] = 85 cm with fixed field of 10x10 cm²):
    - o The diffusion factors of the phantom (Sp) and the collimator (Sc)
    - o The factors of the plates (where the covers are fixed)

1. The shape of the radiation field

- Squares (3x3, 5x5, 10x10, 20x20, 30x30 and 40x40 cm²)

• Rectangular • Complexes, caches: o Central 5x5, 10x10 and 20x20 cm^2 (field of 30x30 cm^2) and 4x15 cm2 (field of 15x15 cm^2) o “C” shaped, oval and wavy (“squiggle”) • Asymmetrical, 10x10 cm^2: o Without corner filter / MLC[5] o With corner filter / MLC
2. Variation of the SSD • Standard SSD, 90 and 110 cm with fields of 5x5, 10x10, 20x20 and 30x30 cm^2
3. Corner filters • Fields of 5x5, 10x10 and 20x20 cm^2 • Variable SSD: 80 and 110 cm
4. The heterogeneities of the environment • Use of a phantom with variable density, use of heterogeneous geometry
5. The inclination of the radiation beam relative to the entry surface • 40° obliquity, 10x10 cm^2 and 30 °, 30x30 cm^2
6. Lack of diffusing medium • Use of compensators
7. Anthropomorphic phantom • Use of anthropomorphic phantoms (full dose calculation tests)

[1]Tissue-Phantom Ratio, [2]Tissue-Maximum Ration, [3]Express the variation of the dose measured under any conditions compared to the reference dose,[4]source to surface distance,[5]MultiLeaf Collimator.

The irradiation beam is segmented into several geometric zones:

- The points located inside the geometric limits of the beam after the region of electronic equilibrium (build-up): region with low dose gradient,
- The points located in the half-light of the beam: region with strong dose gradient which is defined by 0.5 cm on either side of the beam limits,
- The points located outside the geometric limits of the beam and beyond the penumbra: region at low dose and at low dose gradient,

- The points located in the region of electronic equilibrium (build-up): region of strong dose gradient which extends from the entry surface to the depth of electronic equilibrium.

Table II.2: Tolerances published for photon beams in report 62 for tests of Table II.1.

Tests	**Relative dose difference in (%)**			
	Beam interior		**Outside the beams**	**Build-up**
	On the axis	**Off the axis**		
Homogeneous media				
Square fields	1	1.5	2	20
Rectangular fields	1.5	2	2	20
Asymmetric fields	2	3	3	20
Complex fields (caches)	2	3	5	50
Complex fields (MLC)	2	3	5	20
Corner filter	2	5	5	50
Surface obliquity	1	3	5	20
SSD variations	1	1.5	2	40
Heterogeneous media (outside the region of electronic equilibrium)				
Simple (plane geometry)	3	5	5	-
Complexes (anthropomorphic geometry)	5	7	7	-

2. IAEA TRS-430 (2004)

The IAEA (International Atomic of Energy Agency) published in 2004 a very complete guide the TRS-430 for the implementation of QA in radiotherapy (beams of photons and electrons) and in brachytherapy [8]. The proposed tests relate to the hardware and software included in the treatment planning system. The software tests concern the dosimetric and non-dosimetric parts. The report recommends to identify the configurations which must be tested according to the means of the center of radiotherapy while at the level of the techniques of treatment that of the equipment of dosimetry and provides, in photon mode, two lists of tests to be implemented (Table II.3): one exhaustive and the other basic.

To compare the measured and calculated doses, the IAEA recommends the use of either:

- the dose difference relating to the reference conditions, as in TG-53, the acceptability criteria for this evaluation criterion are given in Table II.4,
- the relative dose difference proposed by Venselaar et al. [9], normalization is done in relation to the local reference dose except for areas of low dose and low dose gradient where it is done in relation to the reference dose measured at same depth on the beam axis. The acceptability criteria for photon beams are based on the segmentation of the region of interest (Table (II.4) and Figure II.1).

Table II.3: The complete list of the various tests proposed for the photon beams in the TRS-430, SSD used in the service

1. The shape of the radiation field • Squares * (5x5, 10x10 and 40x40 cm^2) • Rectangulars * (5x30 and 30x5 cm^2) • Complexes (caches or MLC) at 20x20 cm^2: o central cover, not central o MLC: convex in “o” and concave in “c” • Asymmetrical *, 10x10 cm^2: o Without and with corner filter
2. Change in SSD * • With fixed field of 10x10 cm^2
3. Corner filters • Mechanical *: variation of the SSD (90 and 80 cm) and the opening (5x5, 10x10 and 20x20 cm^2) • Automatic: variation of the SSD (90 and 80 cm) and the opening (5x5, 10x10 and 20x20 cm^2)

• Dynamic *: variation of the SSD (90 and 80 cm) and the aperture (5x5, 10x10 and 20x20 cm^2)
4. The heterogeneity of the environment • Equivalent tissue heterogeneity lung *
5. The inclination of the radiation beam relative to the entry surface * • 30 ° obliquity, 10x10 cm^2
6. Lack of diffusing medium * • At the edge of a phantom, 20x20 cm^2
7. The build-up region * • Fields 5x5, 10x10 and 30x30 cm^2, with and without covers, with and without corner filter
8. Special techniques • Develop tests to assess: o Taking account of compensators o IMRT

* The different basic tests offered in the TRS-430.

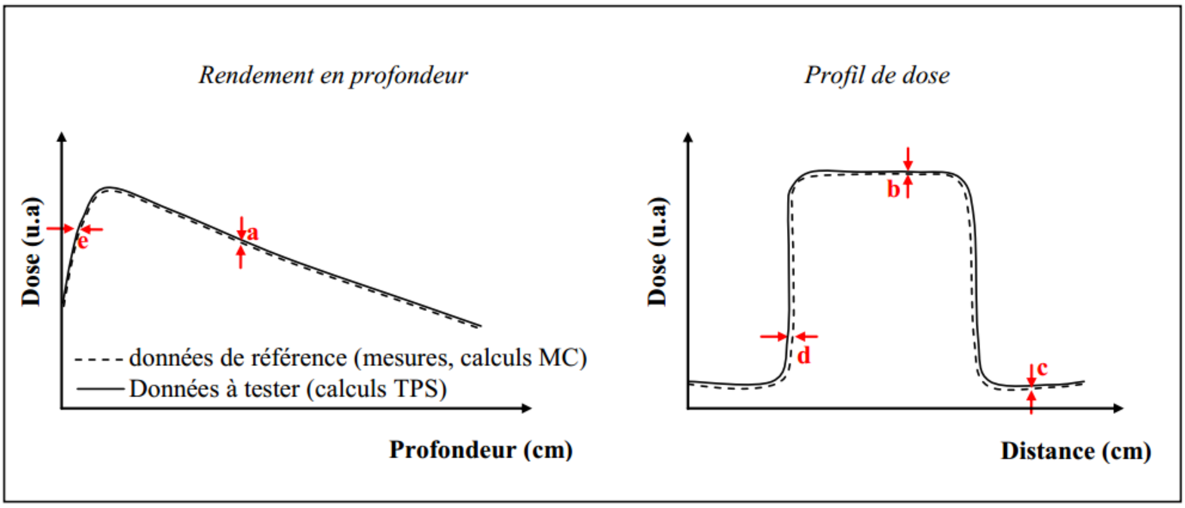

Figure II.1: The segmentation of the region of interest into several geometric zones with the evaluation and acceptability criteria specific to each zone

Table II.4: Acceptable tolerances of relative dose differences for photon beams according to TRS-430 for the tests of Table II.3. In regions with strong dose gradient, a relative distance difference is recommended. Regions a, b, c, d and e are defined in Figure II.1

Symbols	**Regions**	**Simple and homogeneous Geometry**	**Complex Geometry (filters, Covers, MLC…)**	**Geometry much more complex**
a[1]	Central beam axis	2%	3%	4%
e[1],d[1]	Build-up and penumbra regions	2mm or 10%	3mm or 15%	3mm or 15%
b[1]	Outside the beam axis	3%	3%	4%
c[2]	Outside the beam axis	30%	40%	50%

[1] Normalization in relation to the local reference dose, [2] Normalization with respect to the reference dose at the same depth and on the axis of incidence of the beam.

II.1.3.2 Generic measured reference data

The concept of generic data means that the basic data as well as the reference data come from processing devices other than those used locally.

This approach is taken up in report No. 55 of the AAPM TG-23 [10], in the work of Venselaar et al. [11] and more recently in IAEA TECDOC-1540 [12]. These authors provide the basic data and the benchmark results measured for various proposed tests.

The test user configures his TPS for a treatment device of no clinical interest to him from the generic basic data provided and he models the different irradiation beams available for this generic device. Once this "commissioning" is complete, the user reproduces in his TPS the test configurations proposed in the "package" and compares the dose distributions obtained on his TPS in these configurations with generic measured reference data also provided.

1. AAPM TG-23 Report No. 55 (1995)

The AAPM has published a “package” dedicated to the dosimetric QC of TPS, the description of which is given in report No. 55 of the Task Group 23. In this “package”, it provides basic and reference data measured for two beams of photons under two different linear accelerators (4 MV on a Clinac-4 Varian and 18 MV on a Therac-20 AECL). This “package” also includes, in the form of tables, for 15 different tests (Table II.5) the measured doses relative to the "treatment times" used in 15 to 24 specific points. These different points are found at depths between 1 and 35 cm on the axis of the radiation beam and outside the axis. The comparison between the calculated and measured doses is carried out using an absolute dose difference: in fact the doses are normalized with respect to the dose measured on the beam axis in a 10x10 cm^{2}fieldunder reference conditions (for 4MV: maximum dose depth (1 cm) and SSD = 80 cm, for 18MV: maximum dose depth (3 cm) and SSD = 100 cm).

Report No.55 of TG-23 does not provide the tolerances to be used or the frequency of testing.

Table II.5: Various tests proposed in report 55 of TG-23 in order to carry out the CQ of TPS, the SSD is fixed at 80 cm for 4 MV and 100 cm for 18 MV

1. The shape of the radiation field • Squares (5x5, 10x10 and 25x25 cm^2) • Rectangular (5x25 and 25x5 cm^2) • Complexes, caches: o 1x4x7 cm^3 central: 16x16 cm^2 o Non-central "L" shaped: 16x16 cm^2
2. Variation of the PSD • SSD variation (SSD = 70 cm for 4 MV and SSD = 85 cm for 18 MV)
3. 45 ° corner filter • 9x9 cm^2 square field
4. The heterogeneities of the environment • Lung equivalent (0.29 g / cm^3): 6x6 and 16x16 cm^2 • Bone equivalent (1.4 g / cm^3): 16x16 cm^2

5. The inclination of the radiation beam relative to the entry surface
• 45 ° obliquity, 10x10 cm^2
6. Outside the beam plane
• 4cm offset, 10x10 cm^2

Although dedicated only to QC of dose calculation, certainly due to the technical difficulty of dose measurements, this "package" fails to test clinical situations important, in particular the presence of 3D heterogeneities in the irradiated volume. The inclusion of 3D tests is essential because the patient can no longer be modeled by a 2D object. In addition, during treatments for thoracic localizations, the beams pass essentially through soft tissue, bone, and lungs, but the Task Group 23 of the AAPM in its report 55 does not offer tests at this level (interface). The corner filter test uses only a 45 ° filter and a beam perpendicular to the surface of the ghost. The other filters would need to be tested and in particular with an oblique beam which corresponds to its most common clinical use. Recent technological developments such as multi-blade collimators cannot be incorporated into these tests because the accelerators which were used did not offer these accessories at the time.

An upgrade was therefore proposed in 2001 by Venselaar et al. [11]. The dosimetric verification method is similar; this revision includes the same tests proposed in report 55 of TG-23 and other complementary tests. On the other hand, the experimental data set is obtained for two modern accelerators (Elekta SL-15 and SL-20) equipped of a multi-blade collimator. This new data set makes it possible to test the dose calculation of the TPS in the case of new techniques closer to the treatments: field of complex shape, asymmetry of the jaws with and without corner filter, lack of diffusing volume.

II.2 Dose calculation algorithms and heterogeneity correction in external radiotherapy

II.2.1 General Considerations

Photons are indirectly ionizing particles; they transfer their energy to charged particles by interactions with matter (Compton, photoelectric, production of pairs). In this case, the probability of interaction is proportional to the attenuation coefficient μ (in cm^{-1}) and depends on the energy of the incident particle energy E in MeV, the density mass ρ in g.cm^{-3} and the atomic number Z in the middle. Charged particles, on the other hand, gradually deposit their energy by succession of ionizations and excitations along their trajectory (locally or remotely).The deposition of the dose in the patient is therefore linked to four main components which it will be essential to take into account:

- ✓ The primary dose, characterized by the dose deposited by the electrons created by the primary photons during their first interaction after entering the phantom (70 to 95%);
- ✓ The dose diffused in the medium defined by the dose deposited by the electrons created by the primary photons having interacted more than once in the medium (5 to 30%);
- ✓ The dose scattered by the treatment head defined by the dose deposited in the patient by the photons scattered by the treatment head (<5%);
- ✓ The dose due to contamination electrons (<0.5%) [13].

The dose absorbed at a point "P", whose unit is Gray (Gy) corresponding to Joules per kilogram (J/kg), is defined by the energy deposited E (J) by the particles in a very large volume of small mass m (kg). It is expressed by the following relation:

$$D[Gy] = \frac{E[J]}{m[kg]} \tag{II.1}$$

There are three types of formalism for dose calculation:

- ➢ Based on the direct use of measured data;
- ➢ Based on so-called primary/diffuse separation methods;
- ➢ Based on the convolution/superposition methods of kernels (only this method will be detailed because it is the method implemented in used TPS (Eclipse).

The kernel is a model of energy deposition of secondary particles around an interaction site which is in a homogeneous medium independent of location. If we consider this kernel directly, we speak of a kernel point. The kernel points are generated by Monte-Carlo methods. By integrating all the kernels in one direction we get the pencil kernel.

The methods of convolution/superposition of kernels provide models of dose calculations are more precise than the primary/diffuse separation method by responding to the complexity of current radiotherapy treatments. The convolution/superposition methods separate the energy transport and deposition processes into two phases: the primary photons and the secondary particles, both translated by kernels and then convolving them. The irradiated volume is broken down into small volume elements, each receiving a part of the energy deposition model (kernel). Then, each contribution of each kernel is summed up in all the volume elements.

II.2.1.1 Definition of the energy deposition kernel for photons

The energy depositing nucleus, called a kernel, is defined as the distribution of energy transferred to each volume element in a medium, usually water, as a result of the interaction of a narrow beam of photons. This concept has been known since the 1950s [14-15]. It was not used until the 1980s that it was applied to the radiotherapy planning system thanks to Ahnesjö et al. [16] and Chui and Mohan [16]. Thus the kernel point describes the energy deposition of secondary particles in an infinite medium around a site of primary interaction. It is important to note that the principle of the method based on the superposition of kernels is based on the fact that the energy deposited by the secondary particles around an interaction site is independent of the position of the site. Two types of kernel are considered here (Figure II.2):

- ✓ The point kernel (on the left of Figure II.2) for which the dose distribution results from a point interaction between photon and matter in an infinite homogeneous medium (Collapsed Cone) [17-18];
- ✓ The pencil kernel (on the right of Figure II.2) [Ahn5, Moh1] for which the dose distribution results from the interaction of an elementary pencil beam in a homogeneous semi-infinite medium (Pencil Beam and Analytical Anisotropic Algorithms) [19-20].

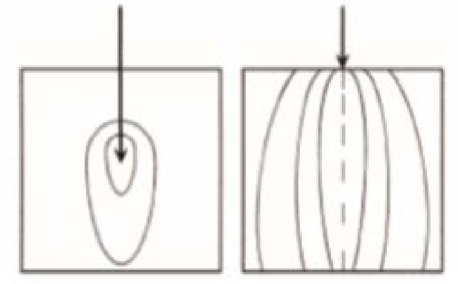

Figure II.2: Representation of the kernel point (left) and the pencil kernel (right)

The kernel points are generated by Monte-Carlo methods from the spectrum of primary photons. The latter is either calculated by these methods, or approached iteratively by comparison with a depth yield measured experimentally. When the kernels are spatially invariant, the superposition can be carried out after a pre-convolution of the kernels. Thus pencil kernels are obtained by pre-convolution of kernel points in a preferred direction (beam direction).

II.2.1.2 Point kernel model

The calculation of the dose (in J/kg) from point kernels can be divided into two stages as illustrated in Figure II.3 [17-18]:

- ✓ The first consists in calculating what is defined by TERMA (Total Energy Released per unit MAss) which corresponds to the total energy released by the primary beam per unit mass (in J/kg) in the patient taking into account the variations in electronic density, provided by CT imaging. This calculation is carried out using the so-called ray-tracing technique which consists in defining the radiological path of the particles along a line drawn through a series of voxels.
- ✓ The second consists in superposing on TERMA the response of each kernel. The kernel point is the calculation of the resultant dose of a photon having interacted at a point determined beforehand by Monte-Carlo methods for primary mono-energetic photons. The kernels are then superposed according to the spectrum of the machine.

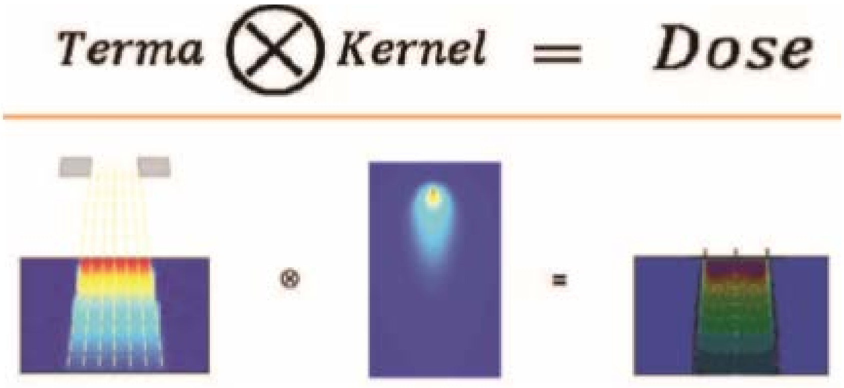

Figure II.3: Representation of the dose calculation from a kernel point.

A point kernel is determined by energy, called a mono-energy point kernel, upstream by Monte-Carlo simulations. The dose is expressed in Gray (Gy) and is determined by the following relationship:

$$D(r) = \iiint_v T(s)k(r-s)d^3 s \qquad \text{(II.2)}$$

With:

$$T(s) = \frac{\mu}{\rho}(r').\Psi\,(r'), \qquad \text{(II.3)}$$

where: $T(s)$ is the TERMA of the primary beam in (J/kg), Ψ is the energy fluency of the primary beam (in J/m^2), $\frac{\mu}{\rho}$is the mass attenuation given by CT images (in m^2/kg), $K(r–s)$ represents the pre-calculated kernel point corresponding to the energy deposited in r in a semi-infinite medium from a primary interaction point s (this term has no unit because it corresponds to a distribution of l energy, i.e. the transfer of a fraction of the energy depending on the primary energy of the interaction) and $d^3s$is the volume element.

The dose at point *r* (receptor) located in a homogeneous phantom is obtained by adding the dose contributions, throughout the medium, of each interaction site s (source).

The transfer of energy from the primary photon interaction site to the point of energy deposition depends on the medium crossed. The heterogeneities are taken into account by scaling the kernels by the average density between the voxel *s* (source) and the voxel *r* (receiver) according to the following equation:

$$K_{het}\,(s,r) = \frac{\rho(r)}{\rho\ hom} c^2 k_{hom}[c(r-s)] \qquad \text{(II.4)}$$

With:

$$c = c\,(s,r) = \int_0^1 \rho_{rel}\,[s-(l(s-r)]dl, \qquad \text{(II.5)}$$

Where:

- ✓ $K_{het}(\,s,r)$ is the kernel corrected by the average electronic density,
- ✓ $\rho(r)$is the density at point *r* (in g/cm^3),
- ✓ $\rho_{hom}$is the density in a homogeneous medium, that is to say the density of water (in g /cm^3),

- ✓ *C(s,r)* is the average electron density between the source s and the reception point r,
- ✓ $K_{hom}[c(r\text{-}s)]$ is the kernel pre-calculated in a homogeneous medium of density mass ρ_{hom}.

II.2.1.3 Pencil beam kernel model

In order to further simplify and speed up dose distribution calculations, kernels can be pre-convolved in one direction. In this case, the calculation is made from pencil kernels which define the energy deposited along a fine beam by integration of several kernel points along this beam. Variations in the spectrum of the primary beam (off axis, filter, modulation, etc.) are taken into account by changing the quality of the Pencil beam according to the input position. This results in the following relation:

$$D(r) = \int_E \iint_s \frac{\mu}{\rho} \Psi_E(x',y') k_{pk}(E, x-x', y-y', z) dx'dy'dE, \qquad \text{(II.6)}$$

where:

- ✓ *D(r)* is the dose at point *r* (in Gy).
- ✓ $\frac{\mu}{\rho}$ is the mass attenuation coefficient in (m^2 / kg)
- ✓ Ψ_E *(x', y')* is the energy flow of the primary photons at the point s of coordinates (x ', y') at the entry of the phantom (in J/m²).
- ✓ K_{pk} corresponds to the pre-calculated mono-energetic pencil kernel for a given medium.

This pre-convolution of the kernels in a direction allows a notable saving of time for the calculation of the dose distributions, but leads to a degradation of the lateral distribution of the dose, especially at the level of heterogeneities.

The energy deposition for a photon beam differs in two stages: locally by the secondary electrons and at a distance by the scattered photons. The integration in 2D brings a clear advantage compared to the kernel point from a point of view of the computation time while being adapted to the irregular fields and to a non-uniform fluence. The pencil beam remains the method of choice for intensity modulation.

The pencil beam method allows the shape of the field to be taken into account (by integration of the actual shape of the field or by equivalent field calculation). This algorithm can be improved by taking into account electronic contamination, the scattering of the collimator, the transmission of the caches, the transmission of the collimator, but also by spectral corrections, surface obliquity corrections and partial heterogeneity corrections [18].

II.2.2 Dose calculation methods and models

II.2.2.1 Methods of convolution/superposition

In this type of model, the dose distribution is seen as a superposition of adequately weighted (kernels) responses for each incident photon. The kernels are classified according to the geometry of the elementary beam which delivers the incident energy. They can be “kernels point” describing the way in which energy is deposited in a medium around the interaction site of the primary photon beam or “pencil kernels” describing the deposit of energy in a semi medium -infinity of a unidirectional beam [21].

We expose below the basic convolution technique, called "kernel point", before presenting two other alternative methods which give it approximations in order to obtain a faster computation.

The calculation of the dose by “kernels points” can be described in two stages. First the calculation, at any point of the phantom, of the number of interactions of primary photons coming from the accelerator, precisely the energy released by the primary photons calculated at each point. This energy is called Terma (Total Energy Released per unit Mass), then the dose is calculated by superimposing weighted kernels. For a mono-energetic beam, the dose at a point is given by [23]:

$$D(r) = \int_V \frac{\mu}{\rho} . \psi(s) h(r-s) d^3 s = \int_V T(s) h(r-s) d^3 s, \qquad \text{(II.7)}$$

Where μ/ρ is the mass attenuation coefficient, the energy fluence of the primary photons and the convolution kernel (a dose distribution matrix deposited by the scattered photons and the electrons set in motion in the interaction site of primary photons). The product of the mass attenuation coefficient and the primary energy fluence is called TERMA; it is the total energy released per unit mass.

Convolution kernels can be generated on the basis of measurements, but most often obtained by Monte Carlo codes which make it possible to simulate a large number of primary photons and to determine the deposition of the dose in all directions by electrons and scattered photons.

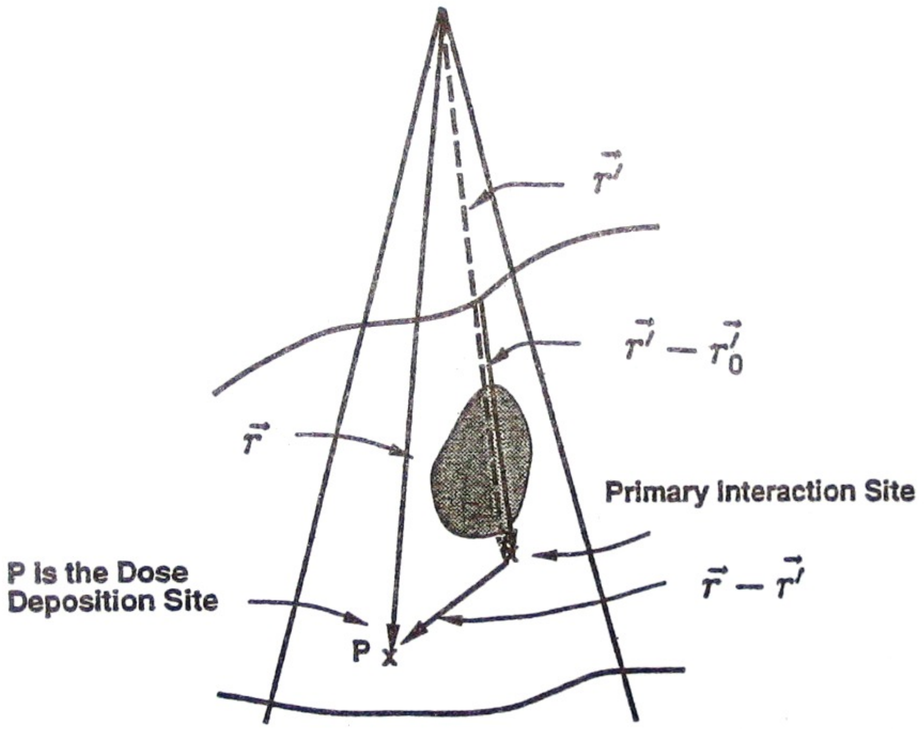

Figure.II.4: Geometry of a photon interaction with matter and the transport of radiation from the interaction site [22].

The X-ray beams used in radiotherapy are not mono-energetic but have a continuous energy spectrum. A generalization of the equation (II.7) is necessary, for a polyenergetic beam [23]:

$$D(r) = \int_E \iiint_V T_E(s) h(E, r-s) d^3 s . dE \tag{II.8}$$

The energy dependence is included in the kernel as TERMA takes shape. The resolution of the energy-dependent equation (II.8) requires a fairly large and long computation time. A series of approximations was then attempted, and it turned out that the separation of the energy diffusion process in separate convolutions for the primary dose and the dose diffused in the medium led to good results. The primary dose here shows the contribution to the dose by the primary photons as well as by the secondary photons created in the head of the accelerator. The dose diffused in the medium takes into account all the photons which have interacted at least once with the medium [24].

As the attenuation coefficients, and therefore the Terma, depend very little on energy. Equation (II.8) therefore becomes:

$$D(r) \approx \iiint_V P(s)\tilde{h}_p(r-s)d^3s + \iiint_V S(s)\tilde{h}_d(r-s)d^3s, \qquad \text{(II.9)}$$

Where: $P(r) = \int T_E(r)\frac{\mu_{én}}{\mu}(E)dE$ $S(r) = \int T_E(r)\left(1 - \frac{\mu_{én}}{\mu}(E)\right)dE$ with kernels $\tilde{h}_p(r)$ (primary dose) and $\tilde{h}_d(r)$ (dose disseminated by the patient) weighted by TERMA and renormalized. μ and $\mu_{én}$ are the linear attenuation coefficient and the energy absorption coefficient respectively.

The energy transfer of the first scattered photons depends on the composition of the medium between the primary interaction site and the place where the dose is deposited. This is why it is customary to use the concept of radiological depth, defined as the geometric depth multiplied by the average attenuation coefficient ($\bar{\mu}$) with respect to water, evaluated along the path of the ray to the calculation point. TERMA is thus calculated at the radiological depth of the site of interaction of the primary photon, while the kernel is weighted by the average electronic density between the site of interaction and the site of deposit of the dose. This method, called “density scaling”, avoids the difficult task of calculating the exact kernels for each situation [23].

The direct resolution of equation (II.9) is called "direct convolution/superposition" [23]. The latter thus takes up in the same convolution the kernels, the TERMA and the correction of heterogeneity, all dependent on energy. This algorithm, as powerful as it is, cannot be used in the clinic because of the large number of operations it requires.

It is therefore necessary to make approximations in order to solve equation (1.4) within reasonable time limits. We will thus describe the “Pencil Beam” and briefly talk about the “Collapsed Cone” which are both used in the clinic.

II.2.2.2 Pencil beam

The dose calculation using the Pencil Beam (PB) algorithm is broken down into four kernels:

- ✓ The primary dose kernel corresponds to the distribution of the energy transmitted to the charged particles released by photons interacting for the first time;
- ✓ The dose kernel scattered in the phantom corresponds to the distribution of the energy transmitted to the charged particles released by photons which have interacted with the medium more than once, photons scattered or created in the medium;
- ✓ The kernel of contaminated particles defined on the patient's surface including the charged particles released by the incident photons after passing through filters, collimations and air;
- ✓ And the kernel of the photons diffused in the head including the diffused of the direct head and the diffused of the head in the phantom [25].

Beforehand, it is necessary to configure the source. This consists in characterizing the beam by defining an effective spectrum. It is derived from the depth yields calculated and measured by adjustment. From this spectrum, a poly-energetic kernel pencil is deduced by superimposing mono-energetic kernel pencils. This poly-energetic Pencil Kernel is defined at each depth z by a sum of two exponentials belonging respectively to the primary and to the diffused:

$$\frac{pk}{\rho}(r,z) = \frac{A_z\, e^{-azr}}{r} + \frac{B_z\, e^{-bzr}}{r}, \qquad \text{(II.10)}$$

where: pk is the pencil kernel (in J / cm^3), ρdensity mass (kg / cm3) and r is the radius from the PB axis (in cm). A_z, a_z, B_z, b_z are depth-dependent adjustment parameters determined by the method of least squares with az$>$ bz stored in the OMP physical database for each depth between 0.075 cm and 50.025 cm in 0.15 cm steps.

The energy deposit of the third component is defined in the patient by a Gaussian pencil kernel (*pk*) whose radius is independent of the depth. It is expressed per unit of energy of incident photons (valid for energies below 30 MeV) by the following relationship:

$$\frac{PK_{cpc}}{\rho}(r,z) = \alpha . e^{-\beta z} . e^{-\gamma r^2}, \qquad \text{(II.11)}$$

where: ρ is the density mass (in kg/cm^3), *r* is the radius of the Gaussian Pencil Kernel (in cm), *z* is the depth of the calculation point (in cm), and $\alpha, \beta \ and \ \gamma$ are parameters depending on the accelerator.

As for the dose due to the photons scattered in the head, it is applied only outside the primary beam generally taking its source at the level of the equalizing cone, the beam being more divergent than the primary beam.The pencil kernel of the photons of contamination (pk_{pc}) is estimated by the difference between the dose profiles measured and the profiles calculated with the convolution method:

$$\frac{pk_{pc}}{\rho}(r,z) = d_z \, \xi e^{-\zeta r^2}, \qquad \text{(II.12)}$$

where: ρ is the density mass (in kg/cm^3), d_z is the depth dose per unit of fluence in primary energy of the field (in cm^2/ kg), ξ and ζ Pencil Kernel parameters, and *r* is the radius of the Pencil Kernel (in cm).

To calculate the dose at an arbitrary point r, the PB algorithm transfers this point to a water phantom with the same lateral position and the same radiological depth (i.e. the equivalent water depth to obtain the same attenuation). Then, it performs a linear interpolation between the pre-calculated dose kernels $d_{p,inf} \ et \ d_{p,sup}$respectively at the lower depth d_{inf} and at the upper depth d_{sup} surrounding the depth of a point *r*:

$$D_p(r) = \frac{Z_0^2}{(r\zeta)^2} . \frac{A_z}{a_z} . ((1-q) \frac{d_{p,inf}(r_{inf})}{\frac{A_{inf}}{a_{inf}}} + q \frac{d_{p,sup(r_{sup})}}{\frac{A_{sup}}{a_{sup}}}), \qquad \text{(II.13)}$$

where: Z_0 is the depth of the calculation point (in cm), *r* is the distance between the source of the interaction and the calculation point projected on the beam axis (in cm), *A* and *a* are the parameters of the kernel at radiological depth, *q* is a linear interpolation coefficient.

This equation is used in the same way for the scattered dose of the phantom by replacing the parameters A and a by parameters B and b and by using the geometric depth when changing the medium instead of the radiological depth.

The correction for heterogeneity is taken into account differently depending on the dose component. For the primary dose, contaminated particles and contamination photons, the equivalent path length method is used:

$$Z_{rad} = Z_{geom}\frac{\mu}{\mu_{eau}} \qquad \text{(II.14)}$$

where: Z_{rad} is the equivalent radiological depth in water (in m), $Z_{geom.}$ is the geometric depth between the surface and the calculation point (in cm), $\mu$is the average attenuation coefficient along Z_{geom} (in cm^{-1}), μ_{eau} is the water attenuation coefficient (in cm^{-1}).

For the phantom scattering, the algorithm uses a correction factor CF with respect to the homogeneous medium which is easier to implement than the Batho method:

$$CF = \frac{z_{rad}}{z_{geom}} . e^{-0,8\mu(z_{rad}-z_{geom})} \qquad \text{(II.15)}$$

Where: 0.8μ is the average effective attenuation coefficient (in cm^{-1}) determined empirically between the depths Z_{rad} and $Z_{geom.}$

II.2.2.3 Collapsed Cone

The kernel point leading to significant computation times, the Collapsed Cone (CC) algorithm was developed to simplify this model. The main process is to separate the primary dose from the scattered dose, taking into account beam hardening, softening beam softening and divergence in the form of kernels. These kernels being poly-energetic, they can only be defined at precise depths thanks to the sum of mono-energetic kernels describing the spectrum of the machine.

The principle of this algorithm, proposed by Ahnesjö [17], is based on an angular discretization of the kernels according to an angular sector defining a cone. Energy is transported in all directions, the CC type approximation favors energy transport in one direction. In OMP, the kernel is discretized on 10^6 directions distributed mainly towards the front. For each of these directions, the variation of the energy deposit according to the distance r is modeled by a double exponential function defined by the following relation:

$$h(r,\Omega) = (A_\Omega.e^{-a\Omega r} + B_\Omega.e^{-b\Omega r})/r^2, \qquad \text{(II.16)}$$

Where: r is the radius of the collapsed cone depending on the diffusion angle (in cm), Ω is the scattering angle (in rad), A_Ω, a_Ω, B_Ω and b_Ω are parameters which depend on the angle of diffusion Ω.

The first exponential component expresses the energy given up by the primary component and the second exponential; the component of the scattered photons. The accuracy of the calculation is based on the number of preferred directions or angular sectors chosen to perform the calculation.

II.2.2.4 Monte Carlo method

1) Principle of the Monte-Carlo method

The photons, electrons and positrons that enter matter undergo many interactions during which energy is transferred to matter [26]. Analytical methods, such as solving the Boltzmann equation, can be used to account for particle transport. Unfortunately, it is not always possible to solve this type of equation, especially in the case of complex geometries.

On the other hand, Monte-Carlo methods are statistical simulation methods which correlate random processes with physical processes. The transport of particles in matter can be "tracked", by determining the trajectory and interactions of each particle (primary and secondary) from its point of entry to its exit or absorption in the medium. According to the principle of the MC method, the trajectory of each particle is simulated, individually, by randomly drawing the physical parameters of the interactions (position of the interaction, nature of the interaction, type of secondary particle created, energy transfer, scattering angle ...), according to the probability distributions which describe the physical processes involved. These probability distributions are determined from the different cross sections of the interactions which are specific to the type and energy of the incident particle as well than the materials involved.

The transport of the particle (story) is reproduced by performing a succession of interactions. At the end of the simulation of a desired number of particles, the value of a quantity of macroscopic interest (absorbed dose, etc.) is obtained. The number of primary particles is chosen according to the precision sought. An MC simulation result will always be expressed "by primary particle".

The generation of random numbers is the basis of any MC simulation. A mathematical algorithm generates these random numbers. It should therefore be noted that, by the very fact of their production, these numbers are not strictly random and that they are therefore called "pseudo-random"[27-28].

2) Accelerator's head modeling

In order to properly model the accelerator head, it is important to know how it works. Linear accelerators for medical use accelerate electrons to produce radiation beams (electrons or photons) energetic enough to be used in radiotherapy for the treatment of superficial or deep tumors. Electrons are produced, by thermoelectronic effect, from a tungsten filament and accelerated to the electron gun.

The electrons exit from the latter with a Gaussian distribution. Through a magnetic field, they acquire a normal incidence on a target with a high atomic number, in order to make the electron beam clinically acceptable. All the diffusing elements being beyond the target (See Figure II.5), it is a question of:

- the X-ray target,
- the equalizing cone and the electron diffuser,
- adjustable primary and secondary collimator,
- the multi-leafs collimator,
- the monitoring ionization chambers,
- the mirror,
- retractable corner filters.

Once the accelerator head has been modeled, the Monte Carlo code can provide a theoretical beam supposed to have physical characteristics similar to the accelerator beam. First of all, note that this beam will be valid only for the modeled accelerator, the modeling being based on data and measurements specific to the accelerator. In addition, in-depth yield and profile measurements are still necessary to validate the code and adapt the basic characteristics of the source if necessary.

Note also that any change in the performance of the accelerator over time will require an adaptation of the code.

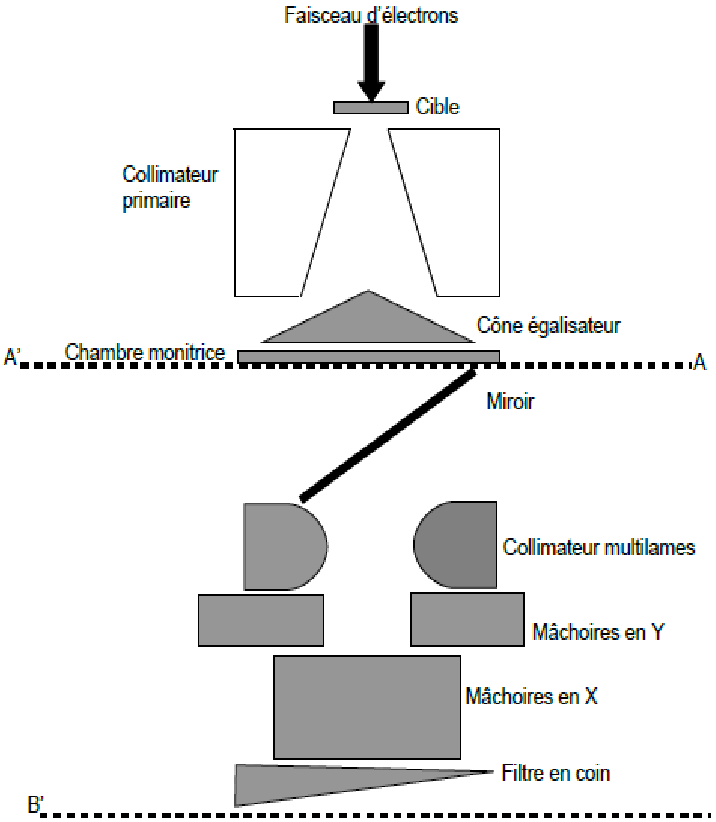

Figure II.5: Block diagram of a linear accelerator head for medical use

3) Monte Carlo in clinics

Monte Carlo codes now offer the possibility of importing scanner images and therefore of carrying out complex clinical treatment plans using real electronic densities. The Monte Carlo stands out as the weakest way to calculate a dose distribution for a patient, despite the excessive calculation time it requires. The clinical plans simulated by Monte Carlo have shown significant gains in the accuracy of the dose calculation, especially for small fields at the interfaces of heterogeneous tissues and in the lung where situations of electronic imbalance can occur. With technological advances in IT, it seems that the Monte Carlo technique will be routinely implemented in TPS in the not too distant future [28].

II.2.3 Algorithms of Varian Eclipse TPS

II.2.3.1 Anisotropic Analytical Algorithm

The AAA algorithm [29], developed by the Varian firm in order to implement it in its Eclipse planning system, is a dose calculation algorithm of the convolution / overlay type. It uses data derived from Monte Carlo simulations to model primary photons, scattered photons as well as contamination electrons. For each clinical beam, Monte Carlo data is optimally adapted in order to build a phase space that defines fluence and the energy spectrum for each processing unit.

The modeling of the dose deposition is carried out by means of six exponential curves. The functional form of the fundamental physical expressions in the AAA allows an analytical convolution, which significantly reduces the computation time. The AAA takes into account the heterogeneities of the tissues in an anisotropic manner (three dimensions) in the vicinity of an interaction site.

The AAA is divided into two algorithms:

1) The configuration algorithm: it determines the physical parameters fundamentals required for dose calculation.

2) The dose calculation algorithm: it calculates the dose deposition using fundamental physical parameters to characterize the particle fluence and the energy spectrum of the photons and electrons that define the clinical beam.

- ✓ **Calculation of the dose for photon beams:**

The attenuation of the photon beam is modeled by a function I_β (z, ρ) defining the energy deposition density, while the lateral diffusion of the energy of the beam is defined by a kernel $K_\beta (x, y, z)$. These two functions are defined individually for each β beamlet. The convolution of the dose is carried out in the AAA in terms of energy. The contribution of primary and extra-focal photons is calculated in an analogous manner, with the exception of their spectral composition and the position and size of their sources.

The main approximation used by the AAA lies in the calculation of the scattered radiation in a voxel which is carried out by superimposing the contributions of the scattered in the direction of the depth (along the beamlet) and the contributions of the scattered coming from the surrounding voxels located in the plane perpendicular to the direction of the beamlet.

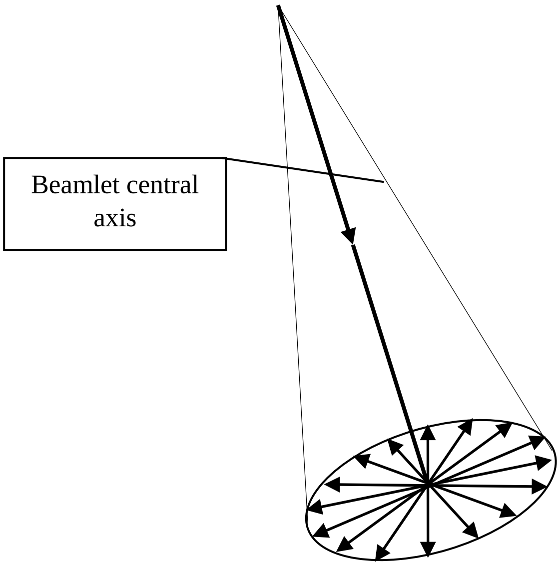

Figure.II.6: Diagram of the taking into account of the scattered in the AAA in the direction of the depth and perpendicular to the direction of the beamlet.

The energy distribution due to photons and resulting from a β beamlet in a sufficiently large homogeneous medium is calculated as follows:

$$E_{ph,\beta}(\tilde{x},\tilde{y},\tilde{z}) = \Phi_\beta \times I_\beta(z,\rho) \times \iint_{(u,v)\in\beta} K_\beta(u-x,v-y)\,du\,dv \qquad \text{(II.17)}$$

In this convolution, the calculation point is represented by in the coordinate system centered on the beamlet. The fluence is assumed to be uniform over the intersection surface defined by the β beam. The function, determining the surface integral of the energy deposited at a depth z, is a poly-energetic function constructed by superimposing pre-calculated mono-energetic energy deposit density functions. It takes into account the heterogeneities of the tissues using the concept of radiological depth *z* ’:

$$I_\beta(z,\rho) = I_\beta(z').\frac{\rho(x;y,z)}{\rho_{eau}} \qquad \text{(II.18)}$$

With $z' = \int_0^z \frac{\rho(x;y,t)}{\rho_{eau}}dt$, where ρ is the electron density.

The "photon scatter kernels" are composed of a weighted sum of six exponential functions:

$$K_\beta(x,y,z)=\sum_{k=0}^{5} c_k(z')\frac{1}{r}e^{-\mu_k(z')r} \quad , \quad r=\sqrt{x^2+y^2} \qquad \text{(II.19)}$$

The value *z'* is used instead of z in order to take into account heterogeneities between the calculation point and the beam entry point. The parameters $c_k(z')$ and $\mu_k(z')$ of the poly-energetic kernel $K_\beta(x, y, z)$ are determined by performing a least squares adjustment of the function $\frac{1}{r}e^{-\mu_k(z')r}$ on the kernels determined by Monte Carlo simulation.

To account for heterogeneities laterally for each beamlet, the energy is weighted by the average density between the calculation point and the origin of the kernel. In practice, this is achieved by dividing the kernel of equation (II.20) into a finite number (16) of rays emerging from the origin.

$$K_\beta(x,y,z)=\frac{\rho_{eau}}{\rho(x,y,z)}\sum_{k=0}^{5} c_k(z')\frac{1}{r}e^{-\mu_k(z')r_d(x,y,\rho)} \qquad \text{(II.20)}$$

Where: $r_d(x,y,\rho)$ is the radiological distance from the original kernel *(0,0, z)* to *(x, y, z)* according to the radius R which passes through (x, y): $r_d(x,y,\rho)=\int_R \frac{\rho(\vec{p})}{\rho_{eau}}\left|d\vec{t}\right|$

- ✓ **Calculation of total dose distribution:**

The total energy absorbed at an arbitrary point of the patient is obtained by superposition of the various energy contributions coming from the primary photons (ph1), the extra-focal photons (ph2) and the electron of contamination for all the individual beamlets:

$$E(\tilde{x},\tilde{y},\tilde{z})=\sum_\beta\left(E_{ph_1,\beta}(\tilde{x},\tilde{y},\tilde{z})+E_{ph_2,\beta}(\tilde{x},\tilde{y},\tilde{z})+E_{cont,\beta}(\tilde{x},\tilde{y},\tilde{z})\right) \qquad \text{(II.21)}$$

The final dose is given by the expression:

$$D(\tilde{x},\tilde{y},\tilde{z})=E(\tilde{x},\tilde{y},\tilde{z}).\frac{\rho_{eau}}{\rho(\tilde{x},\tilde{y},\tilde{z})} \qquad \text{(II.22)}$$

- ✓ **Calculation of Monitor Units (MU):**

The final calculation of MU depends on the prescribed dose, the normalization of the plan, the weight of the field, the normalization of the field and the normalization factor determined by the dose calculation algorithm. This normalization factor determined by the AAA is the number of MUs for a Gy at 100% of the current field. The AAA calculates this UM norm normalization factor using the following equation:

$$UM_{norm} = CBSF(X,Y) \times \left(\frac{UM_{calib}}{D_{calib}} \right) \times \left(\frac{D_{ref}}{D_{norm}(x,y)} \right) \qquad \text{(II.23)}$$

with:

- ✓ *CBSF (X, Y)* = The “Collimator Backscatter Factor” for an open field (X, Y)
- ✓ MU_{calib} = the reference dose in MU at the calibration depth
- ✓ D_{calib} = the reference dose in Gy at the calibration depth
- ✓ D_{ref} = the dose calculated by the AAA for the reference conditions
- ✓ D_{norm} *(X, Y)* = the dose calculated by the AAA at the point of normalization of the field, which depends on the method of normalization of the selected field.

The calculation of *CBSF* depends on the scattering in the ghost, the scattering in the accelerator head and the Output Factors (OF). The “Phantom Scatter Factor” (PSF) is the contribution to the dose due to the diffuse coming from the ghost [30]. It is derived from calculations based on Monte Carlo kernels. The Head Scatter Factor (HSF) represents the change in photon fluence by UM on the surface of the phantom depending on the opening of the jaws, thus taking into account the backscatter in the monitor chamber and secondary photons coming from the head of the accelerator [30]. The HSF is calculated using the parameters of the secondary source. The OFs were measured and entered into the beam configuration for different field sizes. The CBSF in the monitor room will therefore follow the following formula:

$$OF = (PSF + HSF).CBSF \qquad \text{(II.24)}$$

II.2.3.2 Basic PB algorithm

Eclipse differentiates the beam into three sources, the main parameter of which is the energy fluence:

- The primary source (at the target) including the primary photons created in the target.

- The so-called extra-focal source (at the leveling cone), of Gaussian form, containing the scattered photons of the primary collimator and the equalizing cone. This radiation is more divergent than the primary radiation.

- The source of the contamination electrons (including contamination photons) deep in an environment (the patient), describing the amount of dose due to the contamination (electrons and photons) which is calculated at different depths.

These three sources are modeled in the form of kernels according to the energy spectrum of photons depending on the radius (because of the equalizing cone). The multi-blade collimator (static or dynamic) and the dynamic filter which modify the fluence in energy of the beam are taken into account by correcting the extra-focal source.

The dose is calculated in a matrix of divergent voxels, taking into account the average electronic density of the tissues in each voxel according to the conversion curve of the CT. The open beam is divided into a beamlets (elementary beams) with a size of a voxel. The energy distribution by a beamlet is the result of the convolution of the three sources. The energy deposited by the primary source is calculated by the equation:

$$E_{\beta,ph}(x,y,z) = \varphi_\beta \times I_\beta(z,\rho) \times k_\beta(x_\beta, y_\beta, z_\beta) \qquad \text{(II.25)}$$

where:

- φ_β is the fluence of the supposed uniform beamlet,
- $I_\beta(z,\rho)$ is a function of the energy deposit taking into account heterogeneities,
- $k_\beta(x_\beta, y_\beta, z_\beta)$ represents the photon scattering kernel defined by the relation:

$$k_\beta(x_\beta, y_\beta, z_\beta) = \sum_{k=0}^{5} c_k\,(z').\frac{1}{\sqrt{x^2+y^2}}.e^{-\mu_k\sqrt{x^2+y^2}}, \qquad \text{(II.26)}$$

where:

- ✓ $x_\beta, y_\beta, z_\beta$ are the coordinates of the beamlet (in cm).

- x,y,z are the coordinates of the calculation point in the patient's coordinate system (in cm).
- $c_k(z')$ is the kernel weighting factor to ensure the unitary normalization of the energy of the total kernel
- μ_k is the attenuation constant (in cm^{-1})
- z' is the radiological depth between the entry point of the beamlet and the calculation point (in cm).

The energy of the extra-focal source is calculated by the same way with the corresponding kernel while the source of the electrons of contamination is given by the equation:

$$E_{cont,\beta}(x,y,z) = \varphi_{cont,\beta} \times I_{cont,\beta}(z,\rho), \qquad \text{(II.27)}$$

where:

- $\varphi_{cont,\beta}$ is the fluence of the supposed uniform beamlet linked to contamination.
- $I_{cont,\beta}$ is the function of the energy deposition taking into account the heterogeneities linked to contamination.

❖ Lateral scaling:

Energy is scaled to take into account the average density laterally. For this, the beamlet diffusion kernel $k_\beta(x_\beta, y_\beta, z_\beta)$ of equation (II.26) is replaced by the following equation (II.17):

$$k_\beta\left(x_\beta, y_\beta, z_\beta\right) = \frac{\rho_{water}}{\rho_{x,y,z}} \sum_{k=0}^{5} c_k\,(z').\frac{1}{\sqrt{x^2+y^2}}.e^{-\mu_k(z').r_d(x,y,\rho)}, \qquad \text{(II.28)}$$

where:

- $x_\beta, y_\beta, z_\beta$ are the beamlet coordinates,
- x,y,z are the coordinates of the calculation point in the patient's coordinate system (in cm),
- ρ_{water} is the density of water (in g/cm^3),
- $\rho_{x,y,z}$ is the density at the point of calculation (in g/cm^3),
- $c_k(z)$ is the kernel weighting factor to ensure unit normalization of the energy of the total kernel,
- μ_k is the attenuation constant (in cm^{-1}).

- ✓ *z'* is the radiological depth between the entry point of the beamlet and the calculation point (in cm).
- ✓ $r_d(x, y, \rho)$ is the radiological distance to the original depth *z* from the kernel point to the point (*x*, *y*, *z*) along a radius *R* (in cm).

❖ Heterogeneity correction:

The heterogeneities are taken into account by a 1D diffusion kernel according to the local electronic density:

$$k_z(z) = \frac{\rho(z)}{\rho_{water}} \sum_{i=1}^{2} c_i \, . \, \mu_i . \, e^{-\mu_i(z')} \qquad \text{(II.29)}$$

where:

- ✓ $u_i$and c_i are determined by Monte Carlo kernels for each beamlet.
- ✓ $\frac{\rho_z}{\rho_{water}}$ is the local electronic density.
- ✓ *z'* is the radiological distance from the origin of the kernel (in cm).

The energy distribution for the coordinate point (*x*,*y*,*z*) is converted by convolution with this 1D diffusion kernel:

$$E'_{\beta h}(x, y, z) = E_{\beta, ph}(x, y, z) \times \ k_z(z) \qquad \text{(II.30)}$$

The density used here is the electron density of the material compared to that of water. The maximum value by AAA algorithm is 15 electrons/cm^3. The average electronic density of the voxel is determined from the Hounsfield number conversion curve of the scanner. Scaling in the presence of heterogeneities is done for photons and contaminating electrons. This allows the AAA algorithm to accurately predict the effect of build-down and build-up at the interfaces of the lungs.

❖ Dose conversion:

Throughout the calculation, Eclipse convolves kernels in terms of deposited energy *E*. Thus, the energy absorbed at the calculation point is the superposition of the three components of the dose. The energy distribution is then converted into dose *D*, thanks to the density correction factor and the factor *c* allowing passing from J/m^3 to Gray (Gy):

$$D\left(x_\beta, y_\beta, z_\beta\right) = c.\, E(x_\beta, y_\beta, z_\beta) x \frac{\rho_{water}}{\rho(x_\beta, y_\beta, z_\beta)} \qquad \text{(II.31)}$$

Where ρ_{water} and $\rho(x_\beta, y_\beta, z_\beta)$ are the electronic densities of water and voxel material respectively.

In the presence of heterogeneities, the term $E(x_\beta, y_\beta, z_\beta)$is replaced by equation (II.19).

The “Collapsed Cone” has brought great improvements in the dose calculation in heterogeneous medium. It makes it possible to model with much more precision than the other algorithms of the convolution/superposition type of interfaces including large differences in density, even if it does not have the same level of precision as Monte Carlo.

II.2.4 Heterogeneity correction in external radiotherapy

II.2.4.1 Relevant parameters in the delivery of the dose in radiotherapy

a) Dose in homogeneous medium

Any beam of photons is characterized by its performance in depth in a homogeneous medium (water or equivalent). It represents the energy deposition by quantity of matter, expressed in Gy or Joules per kilogram, in the depth of the medium crossed (see Figure (II.8)). He has remarkable points:

- ✓ the dose at entry,
- ✓ the increase in dose or build-up corresponding to the increase in the creation of secondary electrons,
- ✓ The maximum corresponding to the electronic equilibrium, that is to say when there are as many secondary electrons created as secondary electrons depositing their energy.
- ✓ The decrease in the dose due to the attenuation of the beam by the quantity of material.

The shape of the percentage depth dose (PDD) depends on the energy and the size of the beam and the distance from the skin source. Due to the greater path of the secondary electrons from the high energy photon beams, the depth of the maximum is greater (see Figure II.8).

Figure.II.8: Percentage depth dose (PDD) 6, 10 and 18 MV beams (Precise, Elekta®). The maximum depth is 17 mm, 24 mm and 32 mm respectively, for the energies mentioned above.

Electronic equilibrium is a three-dimensional phenomenon which implies a longitudinal equilibrium (along the beam axis) and a lateral equilibrium (perpendicular to the beam axis). At electronic equilibrium, the relationship between TERMA (or photon energy fluence) and the dose is linear.

The ideal conditions for energy deposition are met in the presence of a wide beam, at the axis of the beam, just after the build-up and in a homogeneous medium with a density equal to 1, therefore water. Indeed, under these conditions the diffusion and the backscattering are maximum with a less proportion of attenuation. While at the beam edges, the dose decreases due to the geometric half-light of the beam (dose decay zone linked to the geometry of the collimator) and of the lateral electronic imbalance (see Figure II.9).

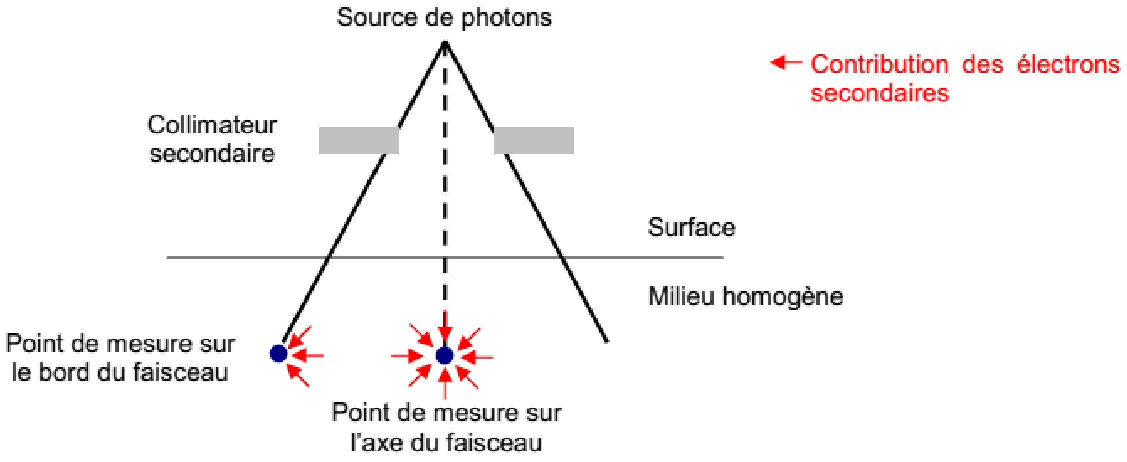

Figure II.9: Contribution of secondary electrons to the dose measurement at a point.

Apart from the conditions mentioned above, electronic disturbances (case of tissue interfaces and the edges of the photon beam) are noted: the dose calculation becomes relatively more complex and the two stages of the photon-matter interaction stated above must be treated separately. They contribute to unwanted overdoses or underdoses.

b) Dose in heterogeneous medium

In this part, we are only interested in low density media. Indeed, the lung, on which we are interested, constitutes a medium of low density due to the air contained in its alveoli.

We found in a population of 16 patients, 8 treated in free breathing and 8 patients treated with respiratory blocking, that the average mass density of the two lungs was 0.20 and 0.13 respectively. The increased flux of scattered photons and of secondary electrons in low density media leads to a loss of electronic balance and a decrease in the dose in adjacent tissues. This dose reduction is strongly dependent on the energy and the size of the beam as well as on the geometry of the air cavity [31]. In fact the heterogeneities modify the attenuation of the ionizing radiation, that is to say its absorption and diffusion; it becomes important to study as precisely as possible the behavior of radiation through these heterogeneities. The correction of the primary dose is obtained in a relatively simple way by considering the linear coefficients of attenuation of the radiation used in water (µwater) and in heterogeneity (µ bone or µ lung) and the thickness thereof. However, calculating the dose delivered is tricky (and it's precisely on this point that many dose calculation algorithms differ depending on how they take it into account) because:

- Diffusion by heterogeneity is different from that produced by an equal volume of water.

- And multiple diffusion is disturbed throughout the irradiated volume.

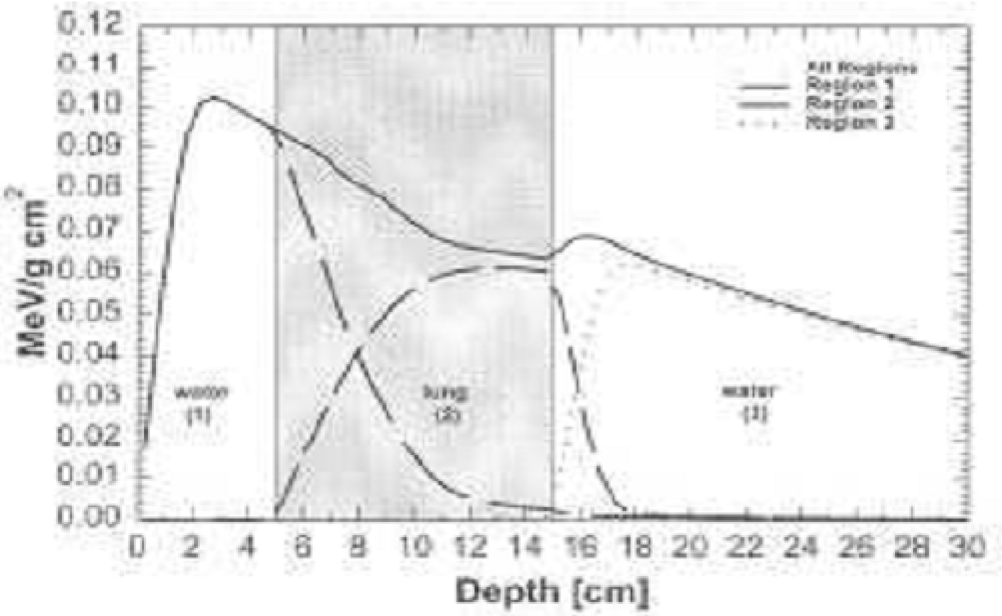

Figure II.10: Effects of electron contributions in media of different densities (water-lung-water) [32].

Figure II.10 illustrates the physical phenomena taking place at the soft tissue / air cavity interfaces. The thick line curve is the depth yield measured on the axis of a photon beam passing through a medium made up of the layers of water, lung and water. The first area in water corresponds to the increase in dose (build-up) until the establishment of electronic equilibrium; the dose is then gradually attenuated in depth. In the central are presenting the lung, the thick line curve is the result of two phenomena. The dotted curves show on the one hand the secondary electrons set in motion in the layer of water which will be attenuated slowly (because their journey is longer in the air) and on the other hand other electrons set in motion in the lung. This therefore results in a decrease of the dose absorbed at this level. At the distal interface, the electrons having been set in motion in the lung will be more quickly attenuated in water, medium denser than air and again electrons are generated in the water (light dotted curve). This results in the establishment of a new electronic equilibrium in the last layer of water [33]. We can note that this second electronic balance is located at a depth less important than that of the first electronic balance.

The flow of electrons is lower in air than in soft tissue, and the contribution of backscatter is smaller. Because of this, the flow of electrons in the last layers of the tissues lack is reduced by "default" backscattering: it is an underdosing zone; therefore a tumor located precisely in this area may be underdosed. Likewise the passage from the air cavity to the soft tissue will be done with an under-dosage in the first layers of the soft tissue because there are less electrons emitted by the air towards this soft tissue. And in the fabric soft there is a build-up again. In the air there is also "setting in motion of electrons" even if the incident beam does not lose practically any energy there. This justifies the "build-down" seen in Figure 13 above. In each case (high energy, small field, low density) the heterogeneity corrections only based on photon fluence or attenuation, prove to be inaccurate.

II.2.4.2 Correction methods and heterogeneity modeling

The purpose of any dose calculation algorithm in radiotherapy is to restore as precisely as possible the energy deposited in each voxel constituting the patient.

II.2.4.2.a Correction-based methods

In the presence of heterogeneities, these methods only correct the fluence of the primary beam; they do not take into account modifications due to the "broadcast" component.

a/ One-dimensional correction of heterogeneities - Batho (power-low Method)

This method uses the densities along the primary beam where the patient is seen as "a set of slices". It does not generate a 3D heterogeneity correction. Described by Batho in 1964, this empirical method takes into account the attenuation of the primary beam and changes in the scattered in water and under a slice of a lung equivalent material (relative density with respect to water of 0.35). Unsuitable in cases where significant heterogeneities are present with an electronic density greater than the tissue (water) and large beams, it can lead to errors in dose overestimation of more than 10%. The same is true for lower density environments than water, large layers and large fields. El-Khatib's studies have shown significant errors in lung irradiations with small high energy photon fields (limit of lateral electronic equilibrium) [34].

b/ One-dimensional correction of heterogeneities - Equivalent Path Length (EPL)

The EPL method links the dose in two media of different density but of identical atomic composition, irradiated by the same beam of photons [35].

It is based on the density scaling theorem of O'Connor stating that the ratio of scattered photons to primary photons is inversely proportional to the densitymass. It makes it possible to connect the dose of two media of different density but of identical atomic composition irradiated by the same beam. A corrective factor FC is defined as theratio of the TAR (Tissue Air Ratio) of the medium of interest (specific density) to the TAR of a medium of density equal to 1, for a circular field. This amounts to correcting the effects of heterogeneities in terms of water thickness equivalent.

c/ Three-dimensional correction - Tissue Air Ratio Equivalent (ETAR)

It was the first method for the treatment plans exploiting the tomodensitometric data. It is also based on the theorem of O ’Connor which allows to correct the influence of variations in densities between a source point of diffusion in the patient and the point of calculation of the dose. It consists of a “scaling” of the dose distribution in a medium other than water and taking into account the changes in depth of the fluence of the primary in this medium compared to water. The EPL correction only applies to primary photons; lateral transport of electrons and scattered photons are ignored.

According to Yorke et al., The Batho and ETAR methods underestimate the dose at the air cavity interface of 55% for 6MV photons [36].

II.2.4.2.b Modeling methods

They refer to the Superposition-Convolution, for which the contributions of the primary and the diffused to the total dose are modified in the presence of fabrics of variable compositions. Here, the variation in energy deposition of the kernel considers both the primary and the diffused for precise angular directions.

- ✓ Superposition: each of the components (primary and diffused) is transported separately, taking into account the variations in density encountered on the route.

- ✓ Collapse Cone: in a given direction axis, the emitted particles, centered on the axis, are transported on the axis of the cone. The emitted particle deposits its energy in this cone.

These methods are the closest to the calculations provided by Monte Carlo, which has become almost a reference in terms of dose modeling.

II.2.5 In-vivo Dosimetry: Principle and Objectives

In vivo measurements consist of taking dose measurements on the patient during irradiation using detectors placed in easily accessible sites such as the skin or natural body cavities. It should be remembered that in radiotherapy, 5% accuracy is desirable and a 10% dose variation at target volume can significantly modify local tumor control or the rate of complications. The ideal treatment would be to deliver a dose for all patients equal to the prescribed dose. In reality, the dose delivered to the patient has a greater or lesser dispersion centered on the prescribed dose in the absence of systematic error.

Human error is one of the main factors constituting the incidents or accidents observed (80 %). Indeed, it is practically impossible to verify everything, and it is usually accepted that the risk of error in any human activity is 1 to3%. From this point of view, in vivo dosimetry can detect systematic errors and - if used daily - random errors, thereby ensuring that the dose delivered to the patient does not differ from the prescribed dose significantly.

When implementing dosimetry in vivo, it is possible to assign two main objectives to this technique:

- Detection and correction of systematic and / or random errors that may occur during the preparation and implementation of radiotherapy. The principle is to have a system capable of generating warning signals to the treatment team.

- Evaluation of the overall quality of a particular treatment technique or service. It is the "quality" indicator of the irradiation performed.

The main sources of uncertainty are (non-exhaustive list):

- Thedosimetry of the radiation beams by the dose planning system (beam data, algorithms, heterogeneity corrections, etc.),
- the patient's anatomical data (contours, heterogeneities, organ movements),

- data transfer,
- the reproducibility of the patient's daily placement,
- The reproducibility of operation of the processing device.

II.2.5.1 Input dose measurement

In this case, the detector is placed on the axis of the beam, or at a point representative of the dose delivered by it (at a distance from the beam limits, far from the shadows), directly on the patient's skin. The measured input dose value is then a function of the characteristics of the beam emitted by the machine, the positioning of the patient and the presence of accessories placed in the beam. This measurement of the dose at the input makes it possible to control the irradiation time or the number of monitor units delivered, the correct consideration of accessories and the correct positioning of the patient at the correct distance from the treatment source.

The measurement of the input dose on the beam axis is compared to the input dose calculated by the dose distribution calculation system or by the independent software for calculating the monitor units. The difference between the dose measured at entry and the calculated dose is then determined and compared to the intervention threshold defined in the quality assurance program of the radiotherapy department.

II.2.5.2 Outgoing dose measurement

The value of the dose measured at the beam exit, on or off the axis, is a function, in addition to the beam characteristics mentioned above, of the patient anatomical data used for the calculation of the number of monitor units.

It therefore makes it possible to validate parameters such as the patient's thickness and the correct consideration of heterogeneities. When the measurement of the dose at the outlet is coupled with a measurement of the dose at the inlet, it is then possible to reconstruct by calculation the dose delivered at the specification point and to compare it with the prescribed dose.

II.2.5.3 Methodology of implementation

In vivo dosimetry is part of the quality assurance program of the radiotherapy service. Its objectives will be defined based on a risk analysis of the treatment methods implemented.

Communication work must be carried out within the teams in this direction.

The implementation of an in vivo dosimetry program requires specifying the scope and the timetable for deployment in the short and long term.

Today, the main programs used are gradually:

1. Measurements of the dose at the input for all the photon beams, when this is technically feasible, at the 1st or second session and for any significant change in the treatment parameters. The measured intake dose is compared to the calculated intake dose.

2. Measurements of the exit dose in addition to the entry dose in the same way as above. The dose at the prescription point is then calculated from the values of the doses measured at the inlet and at the outlet.

The doses reconstructed by beam are added in order to compare the total dose delivered to the target volume with the prescribed dose.

3. The in vivo dosimetry as described above in 1 may also be carried out for the electron beams.

Whatever the objective, the procedure for clinical implementation of in vivo dosimetry follows the same steps:

1) Calibration of detectors,

2) Measurement of influencing factors,

3) Phantom tests (under the accelerator), to validate the quality measurements.

4) Deployment of a service management system in the service in vivo dosimetry results (recording, evaluation, follow-up actions) [37].

References

[1] IAEA. Radiation Oncology Physics: A Handbook for Teachers and Students.

Chapitre 12, p.407: Podgorsak. 2005.

[2] Mayles, P, Nahum, A, Rosenwald, JC. *Handbook of Radiotherapy Physics: Theory and Practice*. Parties F (chapitre 26, p.549) et H (chapitre 37, p.793): Taylor &Francis. 2007.

[3] AEA. TRS No.430: *Commissioning and Quality Assurance of Computerized Planning Systems for Radiation Treatment of Cancer*. Vienna, International Atomic Energy Agency. 2004.

[4] Bruinvis, IAD, Keus, RB, Lenglet, WJM, et al. *The Netherlands Commission on Radiation Units: Quality assurance of 3-D treatment planning systems for external photon and electron beams.* . NCS, Report No. 15. 2006.

[5] Rosenwald, JC. *Sécurité en radiothérapie : le contrôle des logiciels et des systèmes informatiquesSafety in radiation therapy: quality assurance of computerized system*. Cancer/Radiothérapie 2002;6:180-189.

[6] Mijnheer, B, Olszewska, A, Fiorino, C, et al. *Quality Assurance of Treatment Planning Systems Practical Examples for Non-IMRT Photon Beams Practical Examples*. ESTRO, BOOKLET NO. 7. 2004.

[7] Fraass, B, Doppke, K, Hunt, M, et al. *American Association of Physicists in Medicine Radiation Therapy Committee Task Group 53: quality assurance for clinical radiotherapy treatment planning*. Med Phys 1998;25:1773-1829.

[8] IAEA. TRS No. 430: *Commissioning and Quality Assurance of Computerized Planning Systems For Radiation Treatment of Cancer*. International Atomic Energy Agency, Vienna. 2004.

[9] Venselaar, J, Welleweerd, H, Mijnheer, B. *Tolerances for the accuracy of photon beam dose calculations of treatment planning systems*. Radiother.Oncol. 2001; 60:191201.

[10] Miller, D. American Association of Physicists in Medicine Radiation Therapy Committee Task Group 23: *radiation treatment planning dosimetry verification planning,* American Institute of physics. 1995.

[11] Venselaar, J, Welleweerd, H. *Application of a test package in an intercomparison of the photon dose calculation performance of treatment planning systems used in a clinical setting. Radiotherapy and oncology*: Journal of the European Society for Therapeutic Radiology and Oncology 2001; 60:203-213.

[12] IAEA. TECDOC-1540: *Specification and acceptance testing of radiotherapy treatment planning systems*. International Atomic Energy Agency, Vienna. 2007.

[13] A. Ahnesjö, M.M. Aspradakis, *Dose calculations for external photon beams in radiotherapy*, Phys. Med. Biol. 44 R99-R155 (1999).

[14] R. Loevinger, *Distribution of absorbed energy around a point source of beta radiation*, Science 112 p 530-531 (1950).

[15] W.M.C. Roesch, *Dose for non-electronic equilibrium conditions*, Radiat. Res. 9 p399-410 (1958).

[16] C. Chui and R. Mohan, *Differential pencil beam dose computation model*, Med. Phys. 11 p392 (1984).

[17] A. Ahnesjö, P. Andreo and A. Brahme, C*alculation and application of point spread functions for treatment planning with high energy photon beams*, ActaOncol. 26 p49-56 (1987).

[18] A. Ahnesjö, C*ollapsed Cone convolution of radiant energy for photon dose calculation in heterogeneous media*, Med. Phys. 16(4) p577-592 (1989).

[19] A. Ahnesjö, M. Saxner, A. Trepp, *A Pencil Beam model for photon dose calculation*, Phys. Med. 19 p263-273 (1991).

[20] R. Mohan, C. Chui and L. Lidofsky, *Differential pencil beam dose computation model for photons*, Med. Phys. 13 p64-73 (1986).

[21] Ann Van Escha et al., *Testing of the analytical anisotropic algorithm for photon dose calculation*, Med. Phys. 33(11), November 2006.

[22] Andreas Ahnesjö, «Dose Calculation for External Photon Beams in Radiotherapy, Phys. Med. Biol, 44, pp. R99-R155, 1999.

[23] IAEA, TRS-398, «Absorbed Dose Determination in External Beam Radiotherapy: An International Code of Practice for Dosimetry based on Standards of Absorbed Dose to Water», 23 April 2004.

[24] Papanikolaou ET AL, «Tissue inhomogeneity corrections for megavoltage photon beams», Report of Task Group N°65 of the Radiation Therapy Committee of the American Association of Physicists in Medicine, 2004.

[25]Oncentra Master Plan v3.1, *Physics and algorithms reference manual,* 192.739ENG01, Nucletron.

[26] B. Davison, *Neutron Transport theory*, Oxford University Press, London (1957).

[27] A. Boston, *Introduction to MCNP - the Monte Carlo transport code,* University of Liverpool (2014).

[28] B. Serrano, A. Hachem, E. Franchisseur, J. Hérault, S. Marcié, A. Costa, R.J. Bensadoun, J. Barthe et J.P. Gérard, *Monte Carlo simulation of a medical linear accelerator for radiotherapy use*, Radiation Protection Dosimetry 119 p506-509 (2006).

[29] VARIAN, Planning reference guide for Eclipse algorithms, Eclipse 6.5, 29 June 2005.

[30] Gasteren et al., *The determination of phantom and collimator scatter compenents of the output of megavoltage photon beams: measurement of the collimator scatter part with a beam-coaxial narrow cylindrical phantom*. Radiotherapy and Oncology, 20, pp. 250-257, 1991.

[31] Hunt MA, Desobry GE, Fowble B, Coia LR (1997). *Effect of low-density lateral interfaces on soft tissue doses*. Int J RadiatOncolBiol Phys37: 475-482

[32] Papanikolaou N., Battista J., Boyer A., Kappas C., Klein E., Mackie T., Sharpe M., and Dyk J. *Tissue inhomogeneity corrections for megavoltage photon beams*. Task group No 65. 85. 2004. Ref Type: Report.

[33] Caneva S, Tsiakalos MF, Stathakis S, Zefkili S, Mazal A, Rosenwald JC (2006). *Application of the quality index methodology for dosimetric verification of build-up effect beyond air-tissue interface in treatment planning system algorithms*. Radiother Oncol79: 208-210.

[34] El Khatib E, Battista JJ (1984). *Improved lung dose calculation using tissue-maximum ratios in the Batho correction*. Med Phys11: 279-286

[35] Sontag MR, Cunningham JR (1978). T*he equivalent tissue-air ratio method for making absorbed dose calculations in a heterogeneous medium*. Radiology 129: 787-794

[36] Yorke E, Harisiadis L, Wessels B, Aghdam H, AltemusR (1996). *Dosimetric considerations in radiation therapy of coin lesions of the lung*. Int J Radiat. Oncol. Biol. Phys 34: 481-487

[37] Guide pour la pratique quotidienne de la Dosimétrie in Vivo en radiothérapie externe, Institut National du Cancer, France, Octobre 2008.

CHAPTER III :

Thermoluminescence Dosimetry

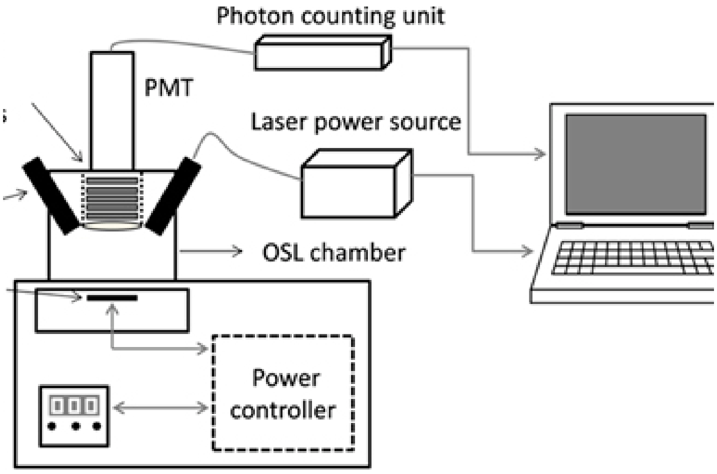

In this chapter

III.1 Thermoluminescence

III.1.1 Early history

The phenomenon of TL was discovered by Sir Robert Boyle who reported to the Royal Society of London on 1663, about "Experiments and Considerations upon Colors with Observations on Diamond That Shines in the Dark"(1663) and described the observation of a “glimmering light” in diamonds [1]. The phenomenon did not find a proper interpretation for about three quarters of a century. The first clear understanding of this observation was provided by Du Fay, who showed that this kind of emission was in fact a delayed phosphorescence. Henri Becquerel detected the occurrence of this phenomenon in certain phosphorescent samples toward the end of nineteenth century. He recognized the ability of certain minerals to retain the effect of irradiation from radioactive substances for a long period. Wiedemann and Schmidt used this phenomenon for the first time to detect the cathode rays and UV light [2]. While the property of thermoluminescence has been long understood, it was not until the early 1950s that Farrington Daniels proposed it as a method for radiation dosimetry [3].

III.1.2 Thermoluminescence producer

The term “thermoluminescence” (TL) consists of two words: thermo, meaning heat and luminescence, meaning emission of light. The primary agents for the induction of TL in a material are the ionizing radiations, namely the X-rays, or radiations from radioactive elements to which the sample is pre-exposed. In some materials, ultraviolet light also may excite TL.

The foundation of thermoluminescence is, that when ionizing radiation interacts with an insulator or semiconductor (usually crystal) (metals do not exhibit luminescent properties) [4], the change of the system from equilibrium to metastable state, it causes electrons in the crystal's atoms to jump to a higher energy state, where they stay trapped due to impurities, until heated. Heating the crystal causes the electrons to drop back to their normal ground state, relaxation of the system back to the equilibrium, releasing a photon of specific frequency [2]. If this energy is supplied by heating the crystal, the TL phenomenon is produced; this energy is known as activation energy or trap depth [5].

The energy required to deflate the electrons is provided by heating the crystal at a constant rate *q*. Figures (III.1.a) and (III.1.b) show respectively the heating ramp used and an example of thermogram. The thermogram represents the light intensity emitted by the crystal as a function of temperature.

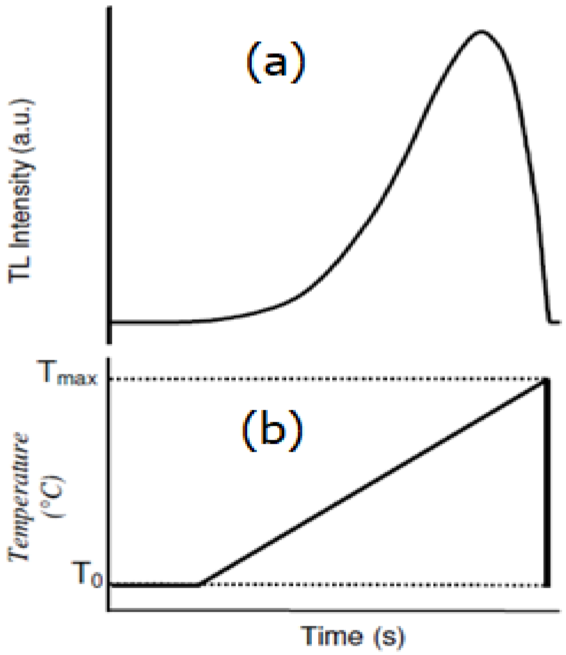

Figure III.1: Schematic presentation of athermogram (a) of a crystal andthe temperature dependence of the luminescenceoutput (b)(1).

Note that there is an important property of TL. It is a particular characteristic of TL that it does not refer to thermal excitation, but to stimulation of luminescence in a sample which was excited in a different way. This means that a TL material cannot emit light again by simply cooling the sample and reheating it another time. It should first be re-exposed to ionizing radiation before it produces light again [2].

III.1.3 Thermoluminescent material's applications

Thermoluminescent materials are used in several areas; we can set:

- ✓ **Radiation dosimetry**: it measures the dose that is absorbed by the sample which is exposed to irradiation.Radiation dosimetry has three subgroups; personnel dosimetry, medical dosimetry and environmental dosimetry [2].

- ✓ **Age determination**: thermoluminescence has been developed to date pottery, flints, rocks, lavas and several other non-pottery materials. If the rate of irradiation from the radioactive minerals is established, then the length of time which the rock has been irradiated "geological age" can be determined [2].

III.2 Theoretical background of Thermoluminescence

I.2.1. Defects

The necessary condition for the induction of TL in a material is that the concerned material should contain certain types of defects in its regular structure. This means that very pure and defect free materials would not show TL [5]. These defects should be capable of capturing electrons or holes during exposure to ionizing radiations.The defect centers may be divided into three categories [5]:

1. Intrinsic defects

2. Extrinsic defects

3. Defects caused by ionizing radiation

- ❖ The intrinsic or native defects. They can be:
- Vacancies or missing atoms (called Schottky defects). A vacancy is a defect obtained when one atom is extracted from its site and not replaced;
- Interstitial or Frenkel defect. It consists of an atom *X* inserted in a crystal *X* in a non-proper lattice site;
- Substitution defects: for example, halide ions in alkali sites;
- aggregate forms of previous defects;
- ❖ Extrinsic or impurity defects, like chemical impurities *Y* in a crystal *X*. They can be:
- Substitution impurity: an atom *Y* takes the place of an atom *X*.
- Interstitial impurity: an atom *Y* is inserted in an additional site not belonging to the perfect crystal.
- ❖ Defects caused by irradiation. The function of irradiating the material with ionizing radiations is to produce free electrons and holes in abundance by the interaction of the incident radiation with atoms of the bulk sample. The concentration of these defects at an ambient temperature may be increased by taking the sample to a higher temperature and then cooling it suddenly

(quenching). In this way, the increased number of defects present at higher temperatures may be frozen. This method is quite common in the preparation of TL samples [6].

The free electron is free to wonder in the crystal can be attracted by a Coulomb force to the localized positive charge and can be trapped in the vacancy. This system or center is called *F* center. Similarly, a positive ion vacancy represents a hole-trap and the system is called V center. Other types of hole-centers are possible:

- ✓ The V_k center is obtained when a hole is trapped by a pair of negative ions,
- ✓ The V_3 center which consists of a neutral halogen molecule which occupies the site of a halogen ion.

All the previous defects are shown in Figure (III.2).

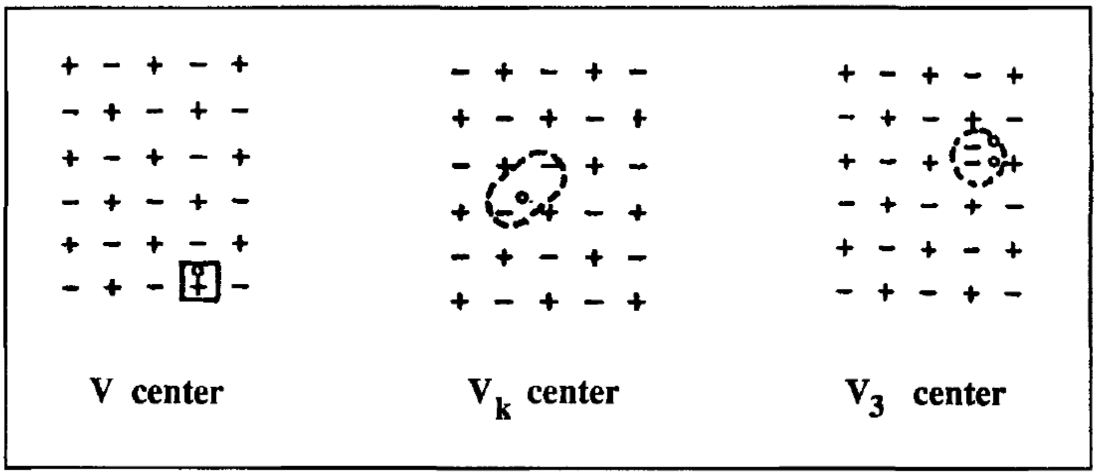

Figure III.2: *V*, V_k and V_3 centers in a real crystal [5].

III.2.2 Traps and recombination

The presence of defects results in the introduction of permitted energy levels in the forbidden band; two types of levels are thus introduced:

1- Trapping centers (or traps).
2- Recombination centers.

Figure (III.3) shows the energy levels of an insulator at equilibrium at 0 K: all levels below E_f (Fermi energy) are filled with electrons while the ones above are empty.

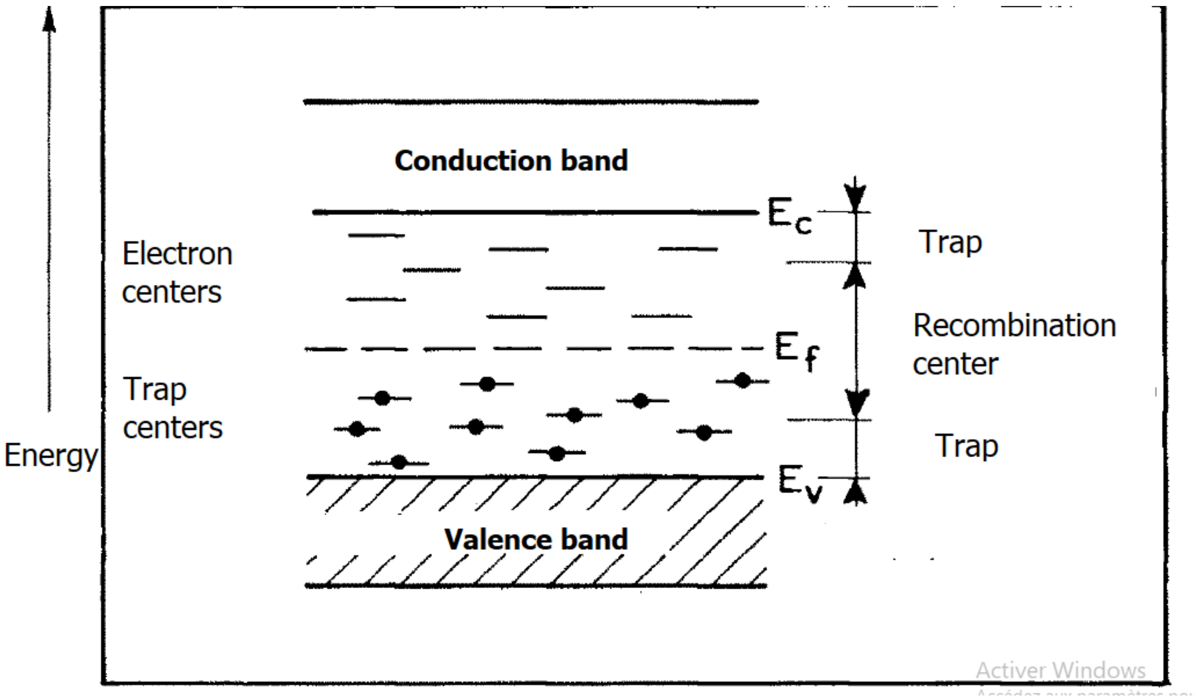

Figure III.3: Energy levels in an insulator in equilibrium ($T = 0\ K$). The levels below E_f are full of electrons, while those above are empty [2].

Electron traps (or holes), centers tend to attract electrons (or holes), are located near the conduction band (valence band) at an energy distance of less than 2-3 eV, whereas the recombination centers are generally located below.

The distinction between traps and recombination centers is essentially on the probabilities of capturing charge carriers.

- An electron trap (hole trap) is a so-called metastable level, which means that it will be necessary to provide a so-called activation energy *E*, which generally corresponds to the energy distance between the trap and the bottom of the conduction band (the top of the valence band) to delocalize the electron (hole) that would have been captured on this center;
- A recombination center: A recombination center is defined as the one in which the probability of recombination with an opposite sign charge carrier is greater than that of thermal excitation of the trapped carrier. The electron-hole recombination can be done; either radiatively or no radiatively [5].

III.2.3 Activation energy

Bombarding the solid with an ionizing radiation, this produces free charges which can be trapped at the metastable states [5]. Electrons and holes remain trapped until enough energy is supplied for liberating them returning the crystal to its original state before the irradiation. This energy is known as activation energy or trap depth [7]. Or, it's the energy needed to release an electron from the trap into the conduction band Figure (III.4).

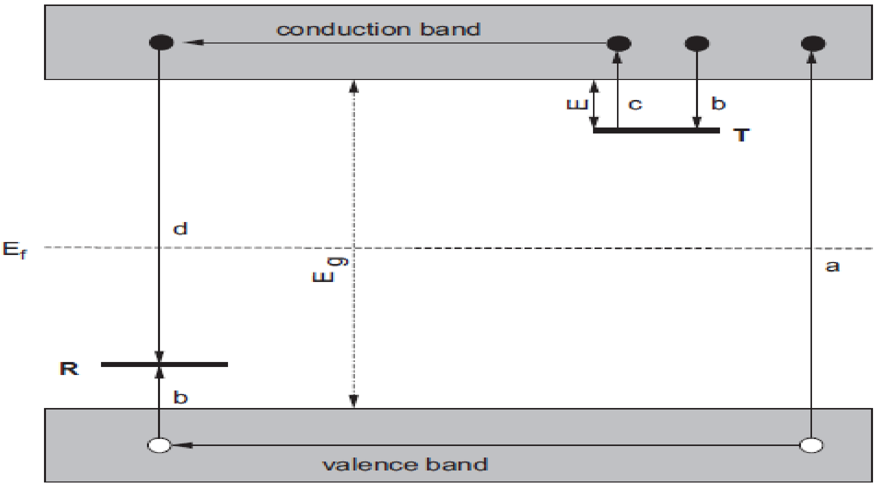

Figure III.4. Energy band model showing the electronic transitions in a TL material according to a simple two-level model: (a) generation of electrons and holes; (b) electron and hole trapping; (c) electron release due to thermal stimulation; (d) recombination. Solid circles are electrons, open circles are holes. Level T is an electron trap, level R is a recombination center, E_f is Fermi level, E_g is the energy band gap.(7)

The probability per unit time of release of an electron from the trap is assumed to be described by the Arrhenius equation [5],

$$p = s\,exp(-\frac{E}{kT}) \qquad \text{(III.1)}$$

Where *p* is the probability per unit time. The term s is called the frequency factor or attempt-to-escape factor. In the simple model '*s*' is considered as a constant (not temperature dependent) with a value in the order of the lattice vibration frequency, namely 1012x10^{14} s^{-1}. *E* is the activation energy. The other symbols have their usual meaning: *k*=Boltzmann's constant=8.617× 10^{-5} eV/K, and *T* the absolute temperature.

The Arrhenius equation gives the meantime, τ, that an electron spends in a trap at a given temperature T [5]. It is given by:

$$p = \tau^{-1} \quad \text{(III.2)}$$

It can be written as:

$$\tau = s^{-1}\exp\left(\frac{E}{kT}\right) \quad \text{(III.3)}$$

It is easily observed that *T* increases as *E* increases. In fact, for $E >> kT$, T increases almost linearly with *E*. For deeper traps, more energy and, in turn, a higher temperature is required to detrap the electrons [5].

Figure (III.5) shows the Properties of the Randall–Wilkins first-order TL equation the variation with the activation energy *E*.

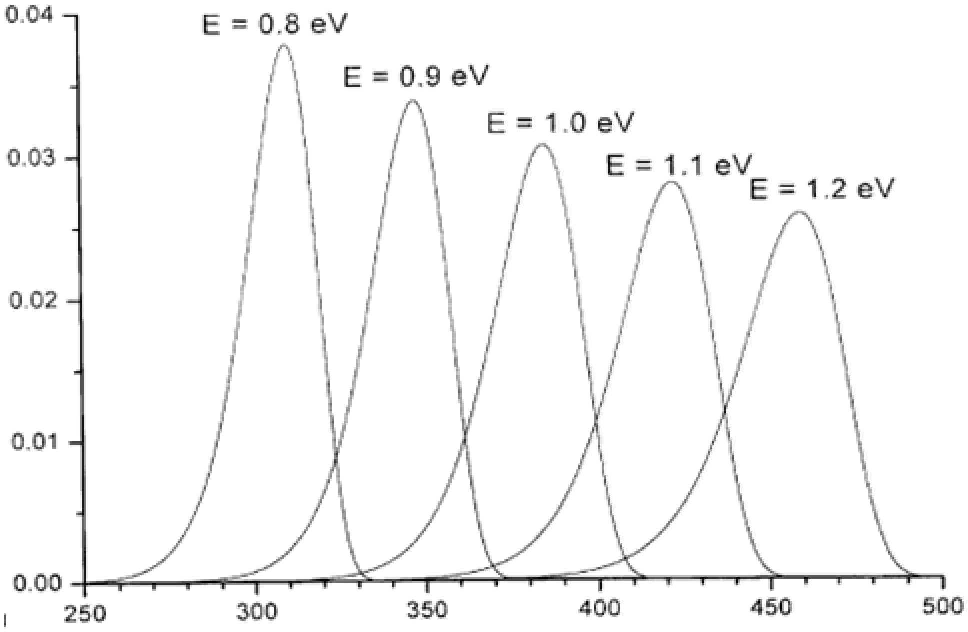

Figure III.5: Properties of the Randall–Wilkins first-order TL equation the variation with the activation energy E.(4)

In figure (III.5), the activation energy *E* has been varied from 0.8 to 1.2 eV. As *E* increases the peak shifts to higher temperatures with a decrease in the height and an increase in the width keeping the area constant. The shift to higher temperatures can physically be understood by realizing that for higher *E* values (deeper traps) more energy (higher temperature) is needed to release the charge carriers [7].

III.2.4 Mobile electron model

Until date, there is not a complete theory to explain this phenomenon. However, there are some models trying to explain it by using three main elements: recombination centers, mobile carriers or charge carriers, and traps.

In an ideal crystalline semiconductor or insulator most of the electrons reside in the valence band. The next highest band that the electrons can occupy is the conduction band, separated from the valence band by the so-called forbidden band gap. The energy difference between the delocalized bands is E_g. However, whenever structural defects occur in a crystal, or if there are impurities within the lattice, there is a possibility for electrons to possess energies which are forbidden in the perfect crystal [4].

The mobile electron model which is based on the energy band theory is used to explain the thermoluminescence, assuming the existence of energy excited states in the forbidden band. These energy states, having a relatively long lifetime (metastable states), are due to defects in the crystalline lattice of the material and can play the role of traps or recombination centers [8].

Figure (III.6) shows schematically the energy levels of an electron in an insulator.

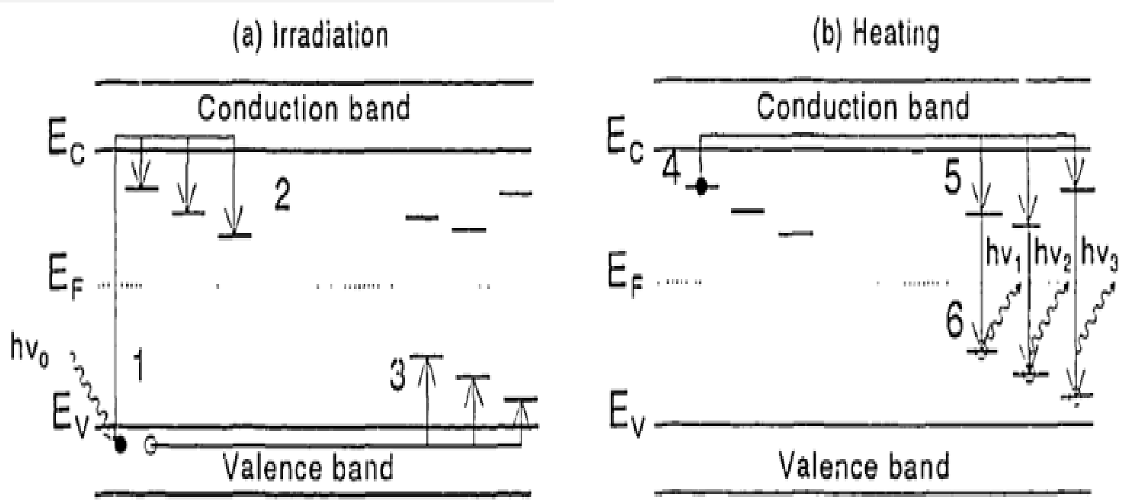

Figure III.6: Band model for thermoluminescence. Transitions are denoted by arrows, electrons by filled circles and holes by open circles.(1) ionization, (2) and (3) trapping, (4) thermal detrapping, (5) recombination, (6) radiative recombination.(8)

Ionizing radiation with $hv>E_g$ can supply the energy for creating the mobile carriers (electrons and holes). The electrons are transferred from the valence band to the conduction band, meanwhile, the holes remain in the valence band when the electrons aretransferred to the conduction band. These charges carrier wander along the crystal lattice until they recombine or they are trapped in metastable states. Later, during the heating, electrons and holes are released from their traps to wander along the crystal until they recombine emitting a visible light photon. Due that the light emission process involves the evacuation ofsome traps at different energies, the mobile carrier is released at different temperatures giving rise to a glow curve which is characteristic of the material and can exhibit one or more peaks [5].

A typical glow-curve for LiF, one of the most thermoluminescent materials, is shown in figure (III.7).

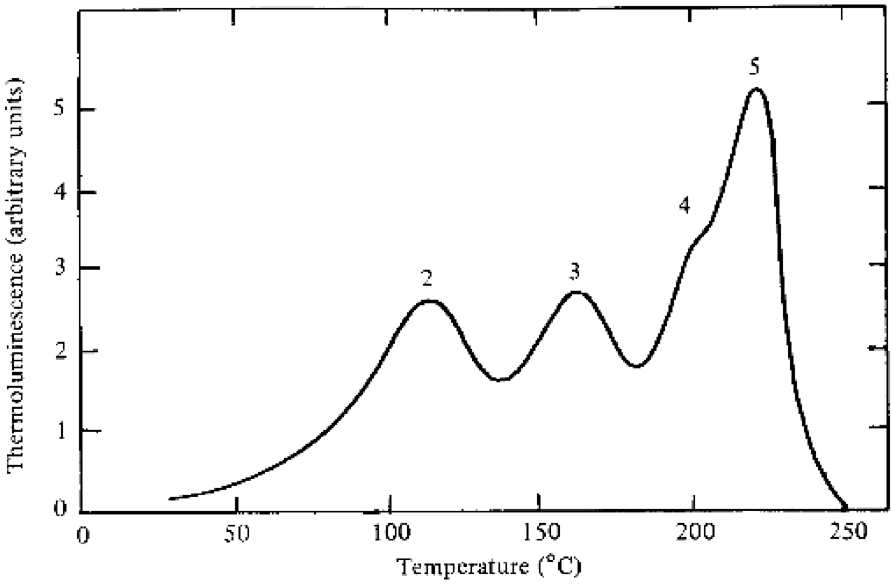

Figure III.7: A thermoluminescence glow-curve from LiF doped with Mg and Ti(2).

The number of radiative recombination in a TL material is proportional to the number of trapped ions, consequently to the number of electron-hole pairs created by ionization. Finally, the emitted luminescence is proportional to the absorbed dose. Besides, it has been demonstrated that the amplitude or the area under one peak, at a constant heating rate, is proportional to the total number of ions captured in the traps. So, the area under the glow curve is representative of the luminous energy released [8].

If the trap depth $E >> kT_0$, with T_0 the temperature at irradiation, then any electron that becomes trapped will remain so for a long period of time. Furthermore, because the free electrons and holes are created and annihilated in pairs, there must be an equal population of trapped holes at level R. Because the normal equilibrium Fermi level E_f is situated below level T(an electron trap), and above level R(a recombination center), these populations of trapped electrons and holes represent a non-equilibrium state [7].

The return to equilibrium can be speeded up by raising the temperature of the TL material above T_0. This will increase the probability of detrapping and the electrons will now be released from the trap into the conduction band. The charge carrier migrates through the conduction band of the crystal until it undergoes recombination at recombination center R. Return to the ground state is coupled with the emission of light. The intensity of TL *I(t)* in photons per second at any time t during heating is proportional to the rate of recombination of holes and electrons at R [5]. If *m* (m^{-3}) is the concentration of holes trapped at R the TL intensity can be written as:

$$I(t) = -\frac{dm}{dt} \qquad \text{(III.4)}$$

Where the negative sign indicates a decrease of holes.

Here, we assume that each recombination produces a photon and that all produced photons are detected. The rate of recombination will be proportional to the concentration of free electrons in the conduction band n_c and the concentration of holes *m*:

$$I(t) = -\frac{dm}{dt} = n_c m A_m \qquad \text{(III.5)}$$

With the constant A_m the recombination probability expressed in units of volume per unit time which is assumed to be independent of the temperature.

The rate of change of the concentration of trapped electrons *n* free and electrons n_c are the following [4].

$$-\frac{dn}{dt} = np - n_c(N-n)A_n \qquad \text{(III.6)}$$

$$\frac{dn_c}{dt} = np - n_c(N-n)A_n - n_c m A_m \qquad \text{(III.7)}$$

With N the concentration of electron traps and A_n the probability of retrapping (m^3 s^{-1}).

III.2.5 Randall and Wilkins model

The kinetics describing the thermoluminescence process was first proposed by Randall and Wilkins, and was based on a simple band model. In this simple model only one kind of trap (electron traps)and one kind of recombination center (trapped hole centers) is considered, along with mobile electrons. Another assumption is that no direct recombination takes place from the electron trap to the recombination center; electronic transport takes place only via the conduction band [5]. If n is the number of trapped electrons in T, and if the temperature is kept constant, then n decreases with time t according to the following expression:

$$\frac{dn}{dt} = -pn = \text{ s}\exp(-\frac{\text{E}}{\text{kT}}) \qquad \text{(III.8)}$$

Where p is the probability p Eq. (I.1), per unit of time, that a trapped electron will escape from the trap;

Integrating the previous equation, we obtain

$$n = n_0\exp\left[-s\ exp\left(-\frac{E}{kT}\right)t\right] \qquad \text{(III.9)}$$

According to the previous assumptions, the TL intensity I, at a constant temperature, is directly proportional to the detrapping rate, *dn/dt*:

$$I = -C\left(\frac{dn}{dt}\right) = Cpn\ , \qquad \text{(III.10)}$$

where C is a constant which can be set to unity.

Remembering Eq. (I.9), we obtain:

$$I(t) = Cn_0 s\ exp\left(-\frac{E}{kT}\right) exp\left[-s\ t\ exp\left(-\frac{E}{kT}\right)\right] \qquad \text{(III.11)}$$

In figure (III.8) are shown the profiles of change in the filled trap population n, the thermal excitation probability p and the TL intensity I as the as a function of temperature T when the sample goes through the heating cycle to read the glow curve [5]. The initial part of the glow curve rises exponentially. In this part, the change in n is not perceptible. On the other hand, the probability of thermal excitation p rises exponentially. The value of n may be considered constant at n_0 in this part. When the number of trapped charges n, is appreciably diminished, the TL intensity curve ceases to rise in the exponential fashion. It goes through a maximum before falling and ultimately falls to zero when all the traps are emptied.

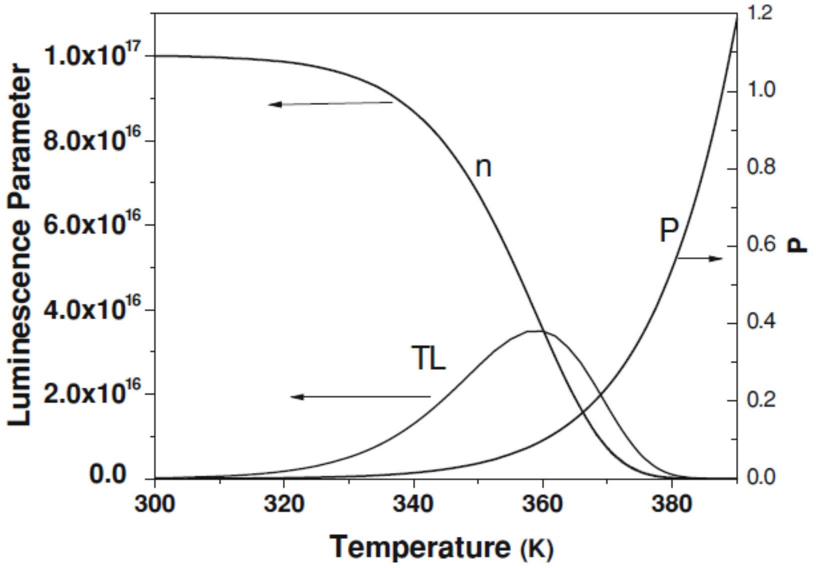

Figure I.8: Profiles of trapped electron population *n*, probability *p* of excitation and the glow curveas a function of temperature during heating. Intensity values plotted in the glow curve are 10 times of theactual computed values for better visibility. Calculations are carried out using the Randall-Wilkins model(6).

The intensity *I* being directly proportional to *n* (see Eq(I.10)), this model of *TL* comes under the category of first order (FO) kinetics [6].

III.3. Thermoluminescence dosimetry

One of the earliest suggested applications of TL was the detection and measurement of absorbed radiation. Dosimetry applications can be most conveniently divided into several general categories. The basic premise in the use of TL in dosimetry is that the intensity of the TL can be related, in a straightforward way, to the absorbed radiation dose. In an ideal system, the TL signal is directly proportional to the absorbed dose over a wide range of doses.

III.3.1 Thermoluminescent Dosimeters

Thermoluminescence is a fairly widespread phenomenon and there are a large number of thermoluminescent materials. Most solids exhibit thermoluminescence to some extent in a certain temperature range. Among these solids a wide variety of phosphor are now available for application to TLD [9].TLDs are available in various forms (e.g. powder, chips, rods and ribbons).

The presently available TL dosimetric materials can be grouped into two main categories: tissue equivalent phosphors, which in general show poor sensitivity (such as $Li_2B_4O_7$, LiF,BeO,etc.), and compounds with high sensitivity but no tissue equivalence (such as $CaSO_4$,CaF_2, etc.). Only a particular type of LiF, doped with Mg, Cu, P and recently introduced in the commercial use, seems to combine together tissue equivalence and high sensitivity properties.

III.3.2 General Properties of TLDs

TL dosimeters exhibit certain characteristics, such as linearity, dose range, energy response, reproducibility, stability of stored information, isotropy, effect of environment on dosimeter performance, batch inhomogeneity, and others.

- **Dose response**

In principal, a desirable dosimeter should have a linear response in relationship between the thermoluminescence intensity (*I*) to the absorbed dose (*D*). However, most conventional TL dosimeters exhibit a non-linear growth beyond a certain dose range, being either supralinearity or sub-linearity between TL intensity and absorbed dose [2], as demonstrated in figure (III.9).Linearity range and the non-linearity behavior depend on the type of dosimeter and its physical characteristics [10].

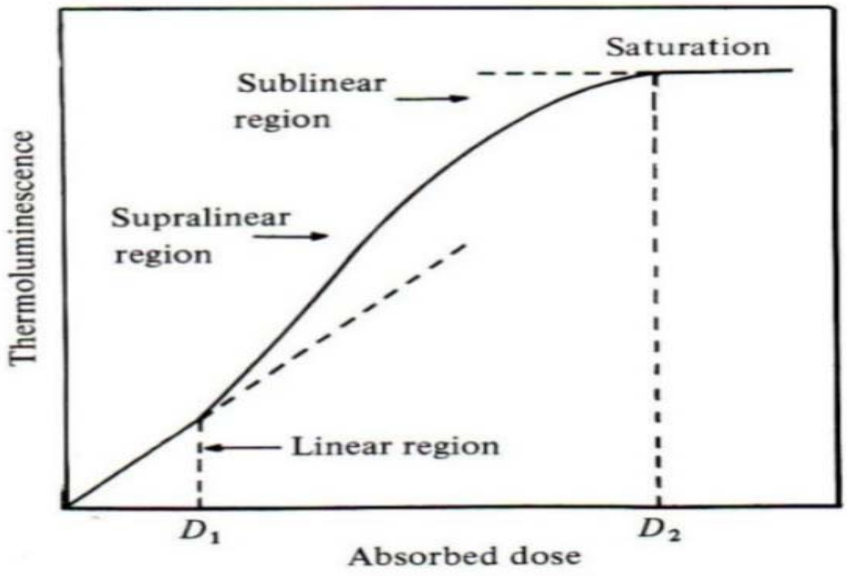

Figure III.9: Diagram of a typical thermoluminescence growth curve showing linear, supralinear, and sublinear regions of a phosphor-based TLD [10].

The occurrence of non-linear regions in the dose response curve of a detector does not preclude its use in TLD, but it does require careful calibration and correction from which additional errors may occur(2).

Supralinearity and saturation can both be affected by previous thermal treatments and exposure to radiation, consequently affecting the reusability of a dosimeter. Due to this, a dosimeter may exhibit a different response upon second and further subsequent use. Therefore, to overcome these sensitization and supralinearity problems, the annealing process is required to re-obtain the original characteristic properties to keep a dosimeter re-useable [2,10] .

Table (III.1) gives the dose ranges within which detectors show a linear behavior.

Table III.1: Linearity range [11].

TL Material	Linearity range for ^{60}Co gamma rays (order of magnitude) (rad)
LiF:Mg,Ti	10-^{2}- 10^{2}
$Li_2B_4O_7$:Mn	10^{-2}- 10^{2}
CaF_2:Mn	10^{-4} - 10^{3}
CaF_2:Dy	10^{-5}- 10^{3}
BeO	10^{-2} - 10^{2}
$A1_2O_3$	No linear characteristics

The TL signal is a function (F) of the absorbed dose D. The normalized dose response function (also called supralinearity index) $f(D)$ is defined as:

$$f(D) = \frac{F(D)/D}{F(D_1)/D_1} \qquad \text{(III.12)}$$

Where $F(D)$ is the dose response at a dose D and $D_1$is a low dose at which the dose response is linear. The ideal TLD material has $f(D) = 1$ in a wide dose rang. If $f(D) > 1$ the response is called supralinear, if $f(D) < 1$ the response is called sublinear [5].

Let us define N as the concentration of empty traps in the material. During irradiation at a dose rate dD/dt the filled traps are:

$$N_f = N - n, \qquad \text{(III.13)}$$

where n is the concentration of the remaining empty traps. So, the rate of decrease of n can be written as:

$$-\frac{dn}{dt} = A\,n\,\frac{dD}{dt}\,, \qquad \text{(III.14)}$$

where A is a constant of the material, called radiation susceptibility.

Making the assumption that no trapped electrons are thermally released during the irradiation, Eq.(I.13) can be integrated as follows, with the initial condition that at t=0,

$$\int_N^n \frac{dn}{dN} = \int_0^t -A\,\frac{dD}{dt}\,dt \qquad \text{(III.15)}$$

From which:

$$n = N\exp(-A.D) \qquad \text{(III.16)}$$

Where D is the total irradiation dose received by the material during the irradiation time t.

The filled traps at the end of the irradiation is given by:

$$N_f = N[1 - \exp(-A.D)] \qquad \text{(III.17)}$$

The heating phase of the irradiated sample, for obtained thermoluminescence, can be expressed as follows:

$$-\frac{dN_f}{dt} = p\,N_f = N_f.s.exp\left(-\frac{E}{kT}\right), \qquad \text{(III.18)}$$

and the intensity of thermoluminescence, *I(D,T)*, is then given by:

$$I(D,T) = -C\,\frac{dN_f}{dt} = C.s.N[1 - exp(-A.D)]\,exp\left(-\frac{E}{kT}\right) \qquad \text{(III.19)}$$

If *A.D*< 1 for small values of *D*, *1-exp(-A.D)* can be approximated to *A.D* and then Eq.(I.19) becomes:

$$I(D,T) = C.s.N.A.D.exp\left(-\frac{E}{kT}\right) \qquad \text{(III.20)}$$

From which it is easily observed that the TL intensity at a given temperature, the glow peak temperature, is proportional to the received dose *D* [5].

- **Energy Response**

Energy response is defined as a measure of the energy absorbed in the TL material. Since the intensity of thermoluminescence emitted from a material is proportional to the amount of energy initially absorbed by that material, it is important to assess the absorption coefficient of a material with respect to radiation energy. For photon irradiations (X- or γ-rays), this evaluation is made via the photon energy response *S(E)* of the system, derived by calculation of the ratio of the mass energy absorption coefficient for the particular material $(\mu_{en}/\rho)_m$ to the mass energy absorption coefficient of a reference material (air or tissue) $(\mu_{en}/\rho)_{ref}$, where μ_{en} is the linear absorption coefficient and ρ is the density in each case [10]. Thus:

$$S(E) = \frac{(\frac{\mu_{en}}{\rho})_m}{(\frac{\mu_{en}}{\rho})_{ref}} \qquad \text{(III.21)}$$

For dosimetry, it is desirable to have a constant energy response over a wide range of energies, thus low Z dosimeter materials are preferable. Additionally, the atomic number Z of a dosimeter is desirable to be close to that of tissue (soft tissue, with effective atomic number, Z_{eff}~ 7.4), known as a tissue equivalent dosimeter. Figure (III.10) represents the difference in energy response for three different Z_{eff} materials; it is notable that the lowest Z_{eff} has the more desirable energy response. CaF_2 (Calcium Fluoride), $CaSO_4$ (Calcium Sulphate), LiF (Lithium Fluoride) have effective atomic numbers of 16.9, 15.6 and 8.14, respectively.

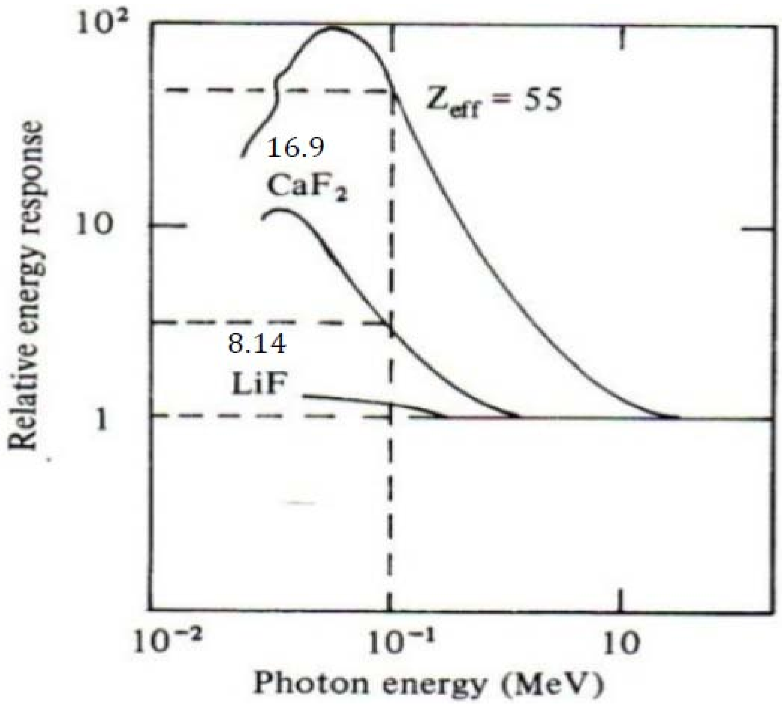

Figure III.10: Diagram of an energy response of TL materials of various effective atomic number [10].

❖ Fading and Stability

The number of electrons trapped in different trapping levels corresponds to the dose measured by the TL material. The inadvertent loss of TL signal occurs both during irradiation and between irradiation and readout is known as fading, depending in large part upon the depth of traps and the storage temperature. Therefore, it becomes necessary to assess the stability of a dosimeter within the environment in which the dosimeter is operated [12].

The half-life of the phenomenon is given by

$$\tau = 0.693\, p^{-1} \qquad \text{(III.22)}$$

Where p is the probability of detrapping.

Table (II.2) gives the temperature of the different peaks and information on the stability of the carriers in the corresponding traps at 20°C for some phosphors.

Table III.2: glow peak temperature and half-life/ fading [11].

TL Material	Peak Number	Emission Half-life	Fading Temp (ºC)
LiF:Mg, Ti	I II III IV V	70 130 170 200 225	5 min 10 hr. 0.5 yr. l yr. 80 yrs.
CaF_2: Mn	I	260	1% per day

It is easy to conclude from the table above that shallow traps have smaller half-lives and will fade more rapidly than deep ones due to a larger transition probability [11].

The fading can be affected by heat (thermal fading) or light (optical fading) [10]. Thermal fading occurs particularly if the trapping depth is rather small so that room temperatures can stimulate release of trapped electrons, during irradiation, between irradiation and during readout. Thermal fading is most apparent within the low temperature peaks of the glow curve. To minimize such effects, it is desirable for the dosimeter to be characterized by a glow-curve with a peak at around 200-250^{o}C, which is sufficiently large to avoid the fading peak but also sufficiently limited to avoid interference from the black-body signal [10].

Comparably, a proportion of the traps can be emptied by optical stimulation, referred to as optical fading. In other words, exposure of a dosimeter to sunlight, fluorescent lamps or to other energetic artificial light sources can liberate trapped electrons (emptying of traps) and consequently loss of a part of the TL signal.

III.3.3 Annealing procedures

Annealing is the thermal treatment needs to erase any irradiation memory from the dosimetry material. Following this annealing procedure for each irradiation has the effect of re-establishing the defect equilibrium, thereby allowing re-use of the material [2].

Some thermoluminescent material required a complex annealing procedure. LiF:Mg,Ti is one of them. It requires a high temperature anneal, followed by a low temperature anneal. Generally, speaking the high temperature anneal is required to clear the dosimetric traps of residual signal which may cause un wanted background during subsequent use of the dosimeters. The low temperature anneal is required to stabilize and aggregate low temperature traps in order to enhance the sensitivity of the main dosimetry traps and to reduce losses of radiation-induced signal due to thermal or optical fading during use [5] (see Figure (III.11)) The combination of these two anneals is termed standard anneal.

It is also true, in general, that more defects are produced at higher temperatures of annealing.

The number of defects also depends on the cooling rate employed to cool the phosphor to the ambient temperature [5].

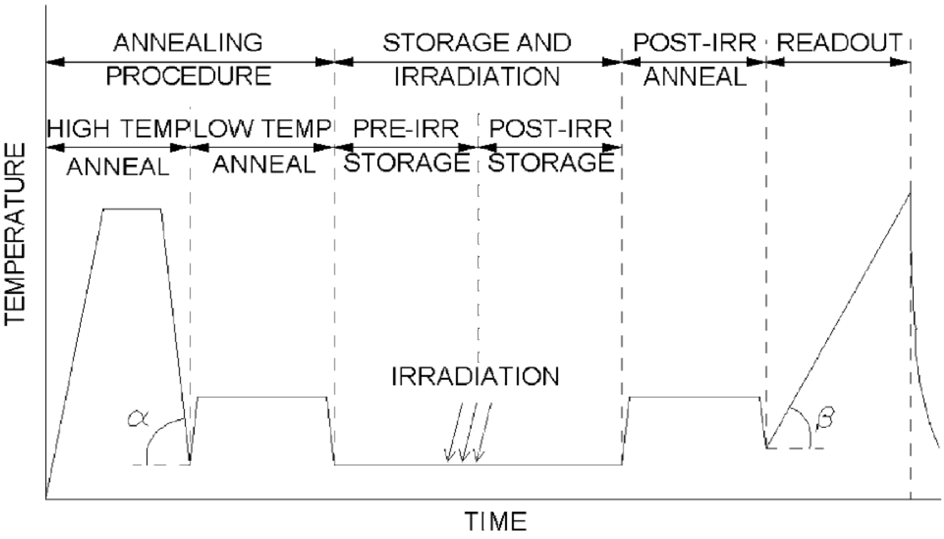

Figure III.11: Overview of the various stages of annealing, storage and read-out of a typical TLD material, where α is the cooling rate following pe-irradiation annealing, and β is the heating rate during TL read-out [7].

The thermal treatments normally adopted for the TLDs can be divided into three classes [5];

- **Initialization treatment:** this treatment is used for new TL samples or for dosimeters which have not been used for a long time. The aim of this thermal treatment is to stabilize the trap levels, so that during subsequent uses the intrinsic background and the sensitivity are both reproducible. The time and temperature of the initialization annealing are, in general, the same as those of the standard annealing.
- **Erasing treatment** or **standard annealing** (also called **pre-irradiation annealing** or **post-readout annealing):** this treatment is used to erase any previous residual irradiation effect

which is supposed to remain stored in the crystal after the readout. It is carried out before using the TLDs in new measurements. The general aim of this thermal treatment is to bring back the traps - recombination centers structure to the former one obtained after the initialization procedure. It may consist of one or two thermal treatments (in latter case, at two different temperatures).

- **post-irradiation** or **pre-readout annealing:** this kind of thermal treatment is used to erase the low-temperature peaks, if they are found in the glow-curve structure. Such low-temperature peaks are normally subjected to a quick thermal decay (fading) and possibly must not be included in the readout to avoid any errors in the dose determination.

III.3.4 Principle of measuring an irradiation dose

The theory shows, starting from the relation (III.5), that the TL peak area (and with a good approximation, its maximum intensity) is directly related to the number n_0 of trapped electrons that is the absorbed dose in the sample. It is this property that is used in TL dosimetry. The conventional device for TL measurement will have to include (Figure (III.12)); a heating device with temperature measurement, a device for detecting the TL and recording TL curves, coupled to an integrating system giving to the surface of the peak. A simplified diagram of a set up for measuring TL is shown in figure (III.12).

A typical TLD reader consists of the following significant components [10]: 1) a planchet (heater cup) for placing and heating the TLD, using a reproducible heating cycle in order to speed up the yield of phosphorescence; 2) photomultiplier tube (PMT) to detect the TL light emission and convert it into an electrical signal. The magnitude of the electrical signal is proportional to the relative light intensity; 3) electrometer for recording the PMT signal as a charge or current.

A nitrogen atmosphere (N_2) is connected to the TLD reader and made to flow at a steady well-controlled rate during the read-out process. The N_2 is used to suppress false light signals due to oxidation during the heating process, the O_2 acting as trapping centers [10].

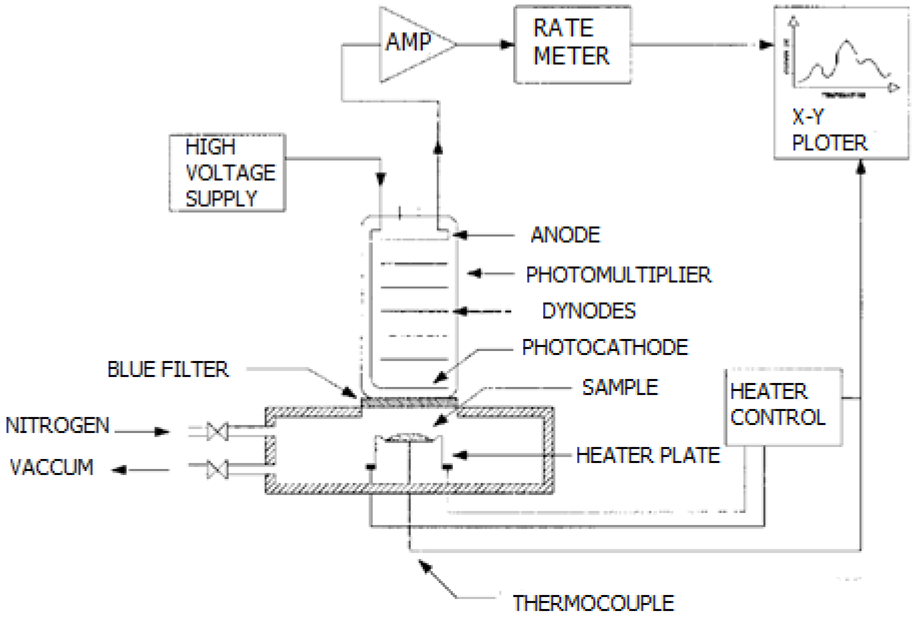

Figure III.12: Simple diagram of a TL reader system with heater plate, photomultiplier detector and readout electronics [13].

III.3.5 Thermoluminescence Dosimetry Applications

TLDs are applied in various fields each with its own demands and constraints (see table (I.3)). The application of thermoluminescent materials in dosimetry may be conventionally listed as personal dosimetry (dose estimated in body tissue) and environmental monitoring (dose estimated in air), with the special consideration for medical applications and reactor dosimetry [2].

Table I.3: Dosimetric requirements in some major application areas [7].

Application area	Dose range (Gy)	Uncertainty, 1 S.D. (%)	Tissue equivalence^{a}
Personnel	$10^{-5} – 5*10^{-1}$	-30, +50	+
Environmental	$10^{-6} – 10^{-2}$	±30	-
Clinical			
Radiotherapy	$10^{-1} – 10^{2}$	±3.5	++
Diagnostic radiology	$10^{-6} – 10$	±3.5	+
Radiation processing^{b}	$10^{1} – 10^{6}$	±15	-

[a] –less required, +required, ++more required, [b] involves sterilization, food processing, material testing, etc.

- **Personnel Dosimetry**

The primary objective of personnel dosimetry is to monitor the radiation dose delivered to personnel during routine occupational exposure. Examples include workers at nuclear reactors, hospital radiotherapy technicians, or naval personnel on nuclear powered vessels. The overall desired aim is to limit an individual's total exposure to below the maximum permissible dose values recommended by the regulatory agencies.

Broadly, personnel dosimetry covers: (i) Extremity Dosimetry - determination of the maximum dose equivalent to any part of the hands, arms or feet, (ii) Whole Body Dosimetry: The primary interest is in penetrating radiation (gamma rays, x-rays (>15 keV) and neutrons), (iii) Tissue Dosimetry (skin dose): this one is interested in non-penetrating radiation (beta particles, and (<15 keV) x-rays).(3)

In all such applications the primary requirement of a TLD material is that of tissue equivalency. That is, one seeks a TLD material that absorbs the same dose of radiation in a given position in a given radiation field as human tissue would absorb if placed at the same position in the same field.

- **Medical Dosimetry**

The small size and high sensitivity of TLD materials has long been exploited in clinical studies since the TLD samples can be inserted into appropriate openings in the human body before exposing the patient to ionizing radiations during diagnosis and/or therapy. The exposed TLDs are then retrieved and analyzed. The two areas of use for clinical radiation exposure of humans are diagnostic radiology (e.g. x-ray exposure in mammography, dentistry and general health screening) and radiotherapy (primarily cancer therapy of various types). Radiation types include X-rays (as slow as 10 keV), gamma-rays (from ^{137}Cs or ^{60}Co), beta particles (up to 40 MeV), protons and other heavy charged particles, and neutrons [3].

III.4 Lithium Fluoride (LiF) Dosimeters

While several materials are still in use for dosimetry applications, the lithium fluorides have been the dominant TL materials over the past 3 decades, starting with LiF:Mg,Ti and now moving to the high-sensitivity LiF:Mg,Cu,P [14].

Studies on LiF, a material of low atomic number and therefore low energy dependence for X-rays, began at the University of Wisconsin, USA, under the guidance of Daniels in 1940. This work, interrupted between 1956 and 1960 because of the poor dosimetry properties of this material, was continued by Cameron, who conceived the systematic regeneration of LiF and encouraged the commercial production, by the Harshaw Chemical Co., USA. of LiF: Mg, Ti dosimeters known as TLD-100, TLD-600, and TLD-700 depending on their preparation from natural lithium or lithium enriched with ^{6}Li or, ^{7}Li, respectively (1). These TLD materials can be produced in a wide variety of forms, from small rods to circular or quadratic chips [15].

Figure (III.13) depicts a TLD cards with the card holders.

Figure III.13: TLDs and TLD’s cards

III.4.1 Isotopic composition

Another possible variation is which isotopic composition is used for lithium, with TLD-100 using natural lithium whereas TLD-600 is enriched in Li-6 and TLD-700 enriched in Li-7. Table (III.4) gives a summary of the most important materials, including the different commercial names given to them.

Table III.4: List of LiF materials and their designation by the two manufacturers ThermoScientific and TLD Poland [15].

Composition	Li isotope	Thermo Scientific	TLD Poland
LiF: Mg, Ti	Natural	TLD-100	MTS-N
Lif: Mg, Ti	Li-6 enriched	TLD-600	MTS-6
LiF: Mg, Ti	Li-7 enriched	TLD-700	MTS-7

TLD 100's are composed from natural lithium which has an isotopic concentration of 92.6% ^{7}Li and 7.4% ^{6}Li [16]. Table (III.5) gives the detailed composition and the areas of usage.

Table III.5: Different isotope composition for TLD-100, TLD-600 and TLD-700 [15-16].

Type	Li-6 content	Li-7 content	Application
TLD-100	7.5%	92.5%	Health and medical physics
TLD-600	95.6%	4.4%	Neutron dosimetry
TLD-700	0.06%	99.93%	Gamma/beta dosimetry

III.4.2 Crystalline structure

The crystal structure of the Lithium Fluoride is therefore face centered cubic in which the fluorine and lithium ions alternate with the vertices of the cube [17]. Figure (III.14) shows the crystal structure of LiF.

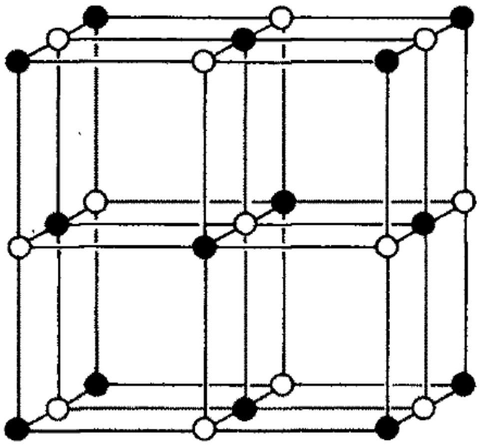

Figure III.14: Crystal structure of LiF: • Li, ° F [17].

III.4.3 TLD-700

Lithium fluoride doped with magnesium and titanium, known commercially as TLD-700, is still the most commonly used radiation dosimeter(personnel dosimetry and health physics) due to its approximately tissue equivalent response [15].

III.4.3.1 Preparation methods

The thermoluminescence of LiF is sufficiently high to detect low exposures, which are of concern in routine personnel monitoring. LiF can be produced in several versions, being manufactured by Harshaw as TLD-100, TLD-600 and TLD-700. The most widely used and also extensively studied version, TLD-100, consists of LiF doped with approximately 170-ppm Mg^{2+} ions and approximately 7 ppm Ti^{4+}ions [18-19]. Harshaw patent describes two preparation methods for LiF:Mg,Ti TL phosphor powders [14,17] : the solidification method and the single crystal method. In the solidification method, lithium fluoride (10^6 parts by weight), magnesium fluoride (400 parts by weight), lithium cryolite (200 parts by weight), and lithium titanium fluoride (55 parts by weight) are mixed in a graphite crucible. The mixture is homogeneously fused in vacuum and the product slowly cooled, then crushed and sieved between 60 and 200 µm. In the single crystal method, the above mixture is placed in a vacuum or inert-atmosphere oven to grow a single crystal at a temperature sufficiently high to obtain a homogeneous fusion mixture. The mixture is then slowly moved to a lower temperature zone to allow progressive solidification (about 15 mm/h). Once the material is cooled, it is crushed and sieved between 60 and 200µm.

TLD-700 has become popular because of several properties. Further characteristics of LiF:Mg,Ti are described in the following Table [15].

Table III.6: Characteristics of ^{7}LiF:Mg,Ti [15].

Material characteristic	**Value for LiF:Mg,Ti**
Effective Z	8.2 (tissue – 7.4)
Useful Radiation Types	Photons, Neutrons, Electrons, Heavy Charged Particles
Dose Range	10µGy – 10Gy (linear) 10Gy – 1,000Gy (supralinear)
Fading	Peaks 2-5: 20% at 3 months Peaks 3-5: 10% at 3 months Peaks 4-5: <5% at 3 months
Residual TL after readout	~0.2% without annealing

Repeatability	2% - 1 SD at 1 mGy
Lower Limit of Detection	10µGy (2.26 SD of zero)
Available forms	Chips, Micro-Cube, Square Rod, Rod, Unsorted Chips, Powder, Pelletized Chip, Pelletized Disk

III.4.3.2 Defects of the TLD-700

The TLD-700 has a face centered cubic crystalline structure. The main ions components of the TLD-700 are Li$^+$ and F$^-$. LiF is a member of the alkali halide group of ionic crystals [20]. In real crystals there will always be some liovalent metal ions present, either as background impurity or as intentional doping [20]. In the case of TLD-700, the two main defects are Schottky defects, where both an Li$^+$ and an F$^-$ ions are missing, and Frenkel defects, where a Li$^+$ or a F$^-$ are moved from a lattice position to an interstitial position. The dopants in TLD-700 are Magnesium and Titanium. Figure (III.15) depicts the previous mentioned defects.

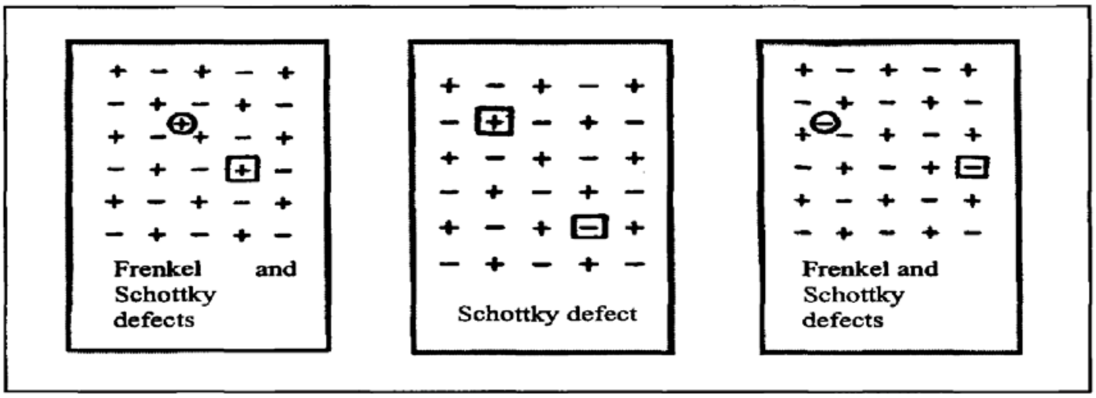

+ alkali ion (Li$^+$), - halide ion (F$^-$), ⊞ alkali ion vacancy, ⊟ halide ion vacancy,

⊕ interstitial alkali ion, ⊖ interstitial halide ion(4).

Figure II.15: Structures of a real crystal with intrinsic defects: LiF.

As an example, Figure (III.16) shows the behavior of the divalent cation Mg^{2+} in LiF: it substitutes a Li$^+$ ion.

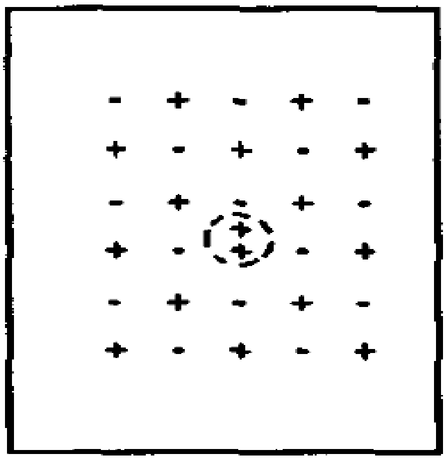

Figure II1.16: Substitutional divalent cation impurity Mg^{2+} [17].

Magnesium enters the lattice as Mg^{2+} and substitutes for a Li^+ atom. As charge neutrality has to be kept, this happens in combination with the appearance of a Li^+ vacancy (written as Mg-Li_{vac}). Titanium also enters the lattice by replacing a Li^+ atom. As it can be either Ti^{3+} or Ti^{4+}there are several ways to reach charge neutrality [20].

III.4.3.3 TLD-700 properties

A big advantage of all LiF materials is the tissue-equivalence of the effective atomic number Z_{eff} which is 7.4 for soft tissue (because of the water content) and 8.2 for TLD-700. Also, LiF has other properties, such as relative low fading and the possibility to manufacture the material with acceptable reproducibility. TLD-700 has some features that do not entirely suitable for use in low dose X-ray such as low sensitivity (which is why it is necessary to calibrate every use), poor detection threshold and disagreement in several reports about the fading [21].

III.4.3.4 TLD-700's Glow curve

The TL glow curve of LiF: Mg,Ti, showing at least five peaks, is quite complicated because of its complex trap dynamics (Figure (III.17)). The main peak (indicated as peak 5) normally used for dosimetric purposes, and then called the dosimetric peak, appears at a temperature of between 220 and 250 ºC (depending on the heating rate) corresponding to a very stable trap level [14].

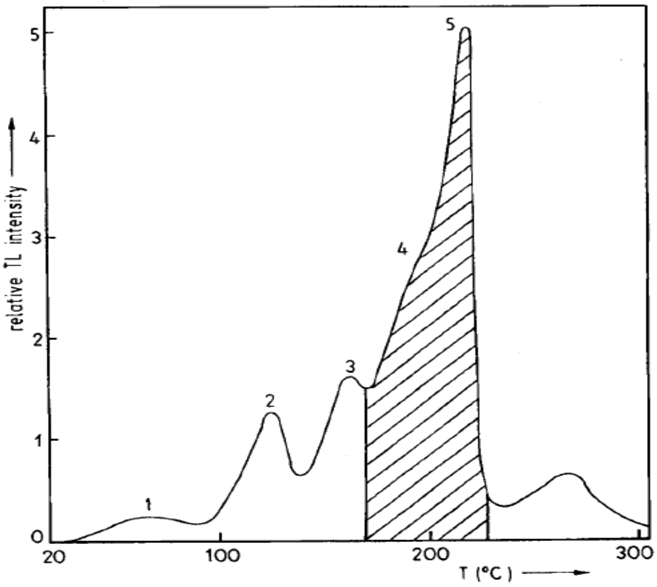

Figure II.17: A typical glow curve of LiF: Mg, Ti showing its complex structure [14].

The low temperature peaks 1, 2, and 3 are relatively unstable and must be suppressed by a thermal treatment. The emission spectrum of nominally pure LiF exhibits a main emission at 415 nm for all the glow peaks up to about 250 ºC when irradiated at room temperature. Such emission band in LiF: Mg, Ti (TLD-700) is variously reported to lie between 400 and 430 nm [14]. Table (III.7) gives a list of 5 important traps or peaks in the glow curve together with the activation energy and the lattice constant. These parameters vary depending on the source because on one hand different batches of the same material yield slightly different results and on the other varying measurement and treatment parameters, such as annealing temperatures and the heat ingrate, also have an influence on the parameters *s* and *E*. Furthermore, peaks 3 and 5 are sometimes, depending on the application and the way the parameters are calculated, split in to two peaks each.

Table III.7: Trap parameters of TLD-700 [14].

Peak	**E [eV]**	**s [s^{-1}]**
1	1.04	1. 10^{15}
2	1.24	1.14. 10^{15}
3	1.30	1.45. 10^{14}
4	1.52	2.6. 10^{15}
5	1.93	5.22. 10^{18}

It should be noted that the peak parameters vary between different publications. The reason is that they strongly depend on the model and the method with which they are calculated.

III.4.3.5 Fading

An important effect is fading, which means the decrease of stored information in a TL material over time. From the Randall and Wilkins model it is possible to derive a formula for the half-life by solving the differential equation (I.9) from the first chapter.

$$t_{1/2} = \frac{ln2}{s} exp\left(\frac{E}{kT}\right) \tag{III.23}$$

Table (III.8) gives the different fading values provided by the manufacturer for the materials mentioned. The fading is of course temperature dependent, as the probability of releasing an electron from a trap is higher if the temperature is higher.

Table III.8: Half-lifes of different traps in TLD-700 at room temperature [17].

Peak	Half-life	Peak temperature(°C)
1	10 min	65
2	1 day	120
3	3 months	160
4	8.5 years	195
5	80 years	210
6	several hundred years	275

The low half-lives of peaks 1 and 2 mean that these will basically be empty as electrons stored in the traps are continuously released again. The half-life of 3 months of peak 3 means that about 80% of the energy is still stored after one month of application. The long half-lives of peaks 4 and 5 make them suitable for use in dosimetry, as they are very stable. In Figure (III.18), fading of peaks of glow curves for the TLD-700 are shown in a period of one month. It is observed clearly the slight decrease in the intensity of the dosimetric peak for the material; the first peak had a higher fading, completely disappearing at the 288 h.

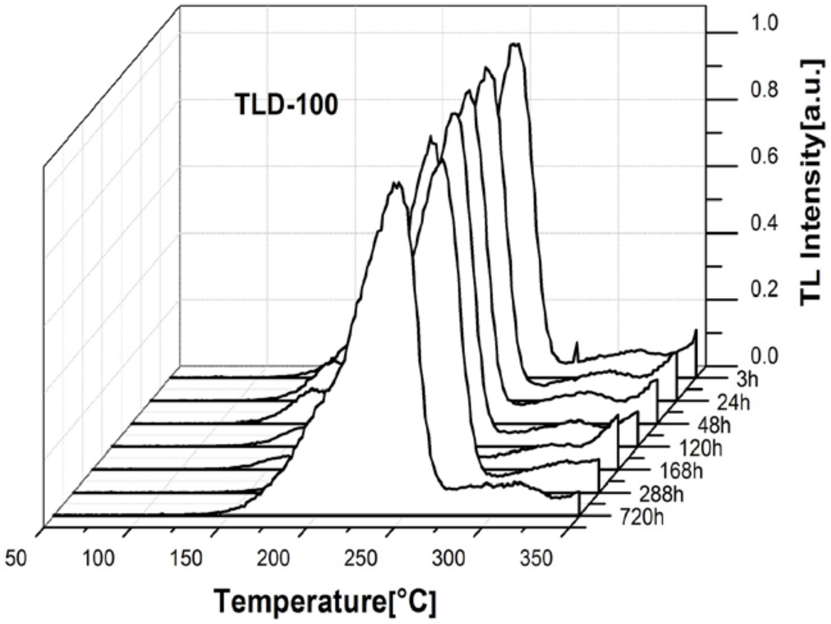

Figure III.18: Graphical representation of the evolution of the glow curves for TLD-700 from 3 hours to up to 1 month after irradiation [21].

The above-mentioned figure (III.18) shows a small shift to higher temperature are seen in the peak temperature of the main dosimetry peak. It is known that a glow peak with kinetic order greater than one (non-first-order TL glow peak) shifts to higher temperatures with decreasing the population of trapping states. Storing the TL dosimeter causes depopulation of trapping states due to fading [21]. Therefore, the TL glow peaks shift to higher temperature with increase in storage time.

III.4.3.6 Effect of Annealing on the LiF Glow Curves

LiF:Mg,Ti requires a high temperature anneal, followed by a low temperature anneal. For lithium fluoride the standard annealing consists of a high temperature anneal at 400ºC during 1 hour followed by a low temperature thermal treatment for20 hours at 80ºC. In some laboratories, annealing at 100ºC for 2 hours has be in used instead of the longer anneal at 80ºC. For dosimetric consideration speak 1 should be ignored and peaks 4 and 5 concentrated on. It has been discovered that by various combinations of pre- and post-irradiation annealing peaks 1 and 2 can be completely removed and those of 4 and 5 enhanced. In as much as most users of LiF as a dosimetric material follow one procedure a standard pre-irradiation anneals of 1 hour at 400°C followed by 24 hours at 80°C can't be adopted [20].

Figure (III.19) shows an over view of the annealing producer. It displays the various stages of annealing of the TLD-700.

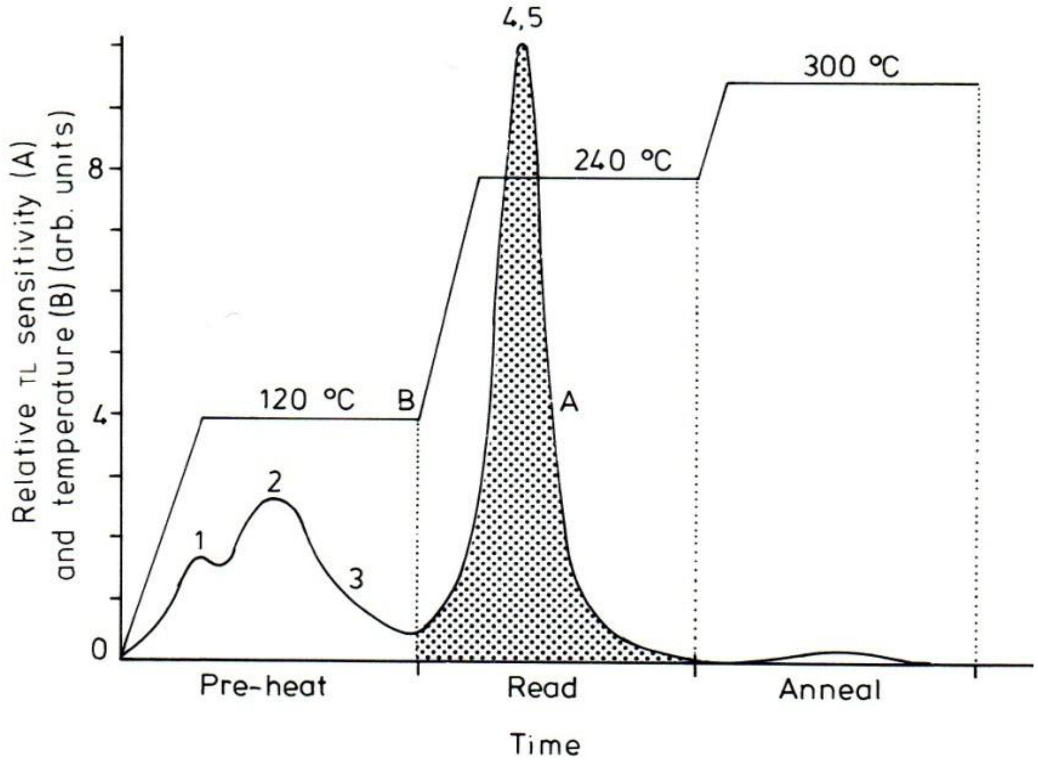

Figure III.19: Diagram of a heating cycle and glow curve used in the reading of LiF: Mg,Ti [22].

An example of the changes which can be induced in the TLD-700 low-curve as a result of various annealing treatments is shown in Figure (III.20).

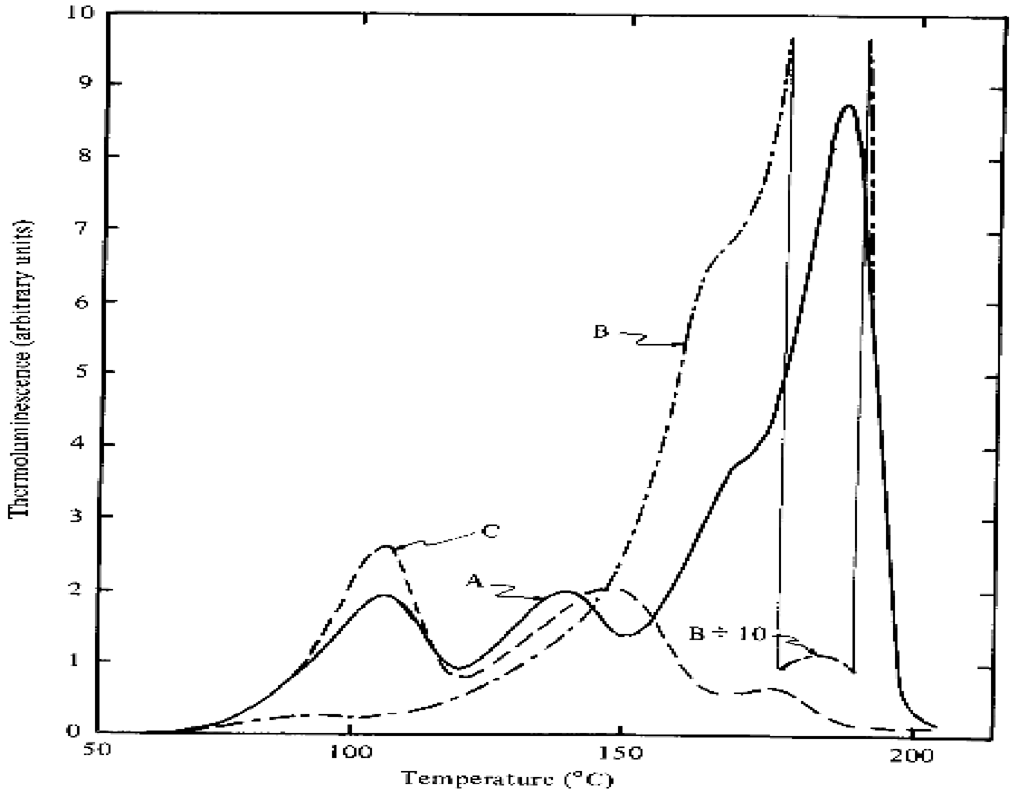

Figure III.20: glow-curves for TLD-700 after a pre-irradiation anneal at: A: 400°C for 1h. B: 400°C for 1h followed by an anneal at 80°C for 24h. C: 400°C for 1h followed by an anneal at 190°C for 10h [15].

A 400°C anneal for 1 hour gives rise to the characteristic glow-curve (curve A). If this heat treatment is followed by an 80°C anneal for 24 hours, the glow-curve change the shape into that shown in curve B, peaks 4 and 5 grow at the expense of peaks 2 and 3. A high temperature anneal at 190°C for 10 hours, cause a drastic reduction in the size of peaks 4 and 5. Clearly, the annealing treatments are inducing defect reactions which are in turn increasing or decreasing the sensitivities of the individual peaks [15].

III.4.3.7 Dose response

The thermoluminescence dose response of the TLD-700 is linear over a wide range of doses, it has a linear range of up to several Gy (100mGy up to about 10Gy) [17], followed by a supralinear region. The saturated region starts at about 1000Gy. Figure (III.21) shows the growth of TL with dose for LiF:Mg,Ti (TL peak 5). The dose response displays a linear-supralinear-sublinear growth.

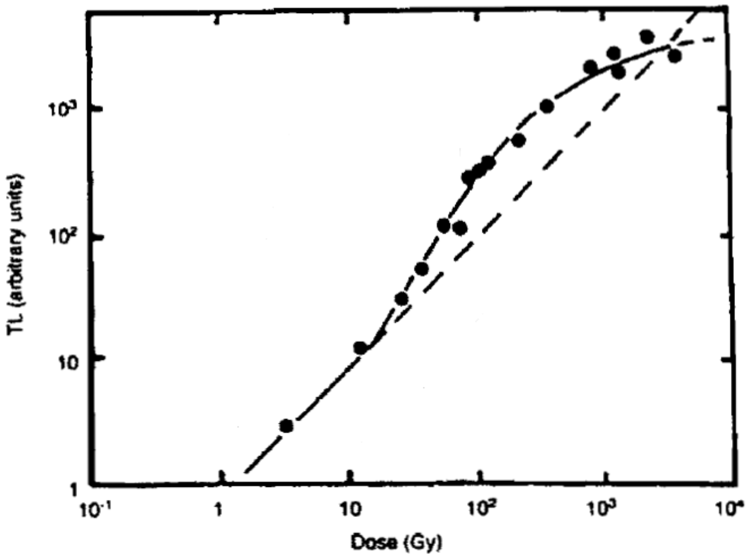

Figure III.21: Dose response curve of the peak 5 from TLD-700 (LiF:Mg,Ti) [23].

In LiF:Mg,Ti, decreasing the Mg content enhances supralinearity, while increasing the OH impurity content decreases supralinearity. All these factors indicate a dependence of *f(D)* on the nature of the host material and its defect structure, including the impurity content [24].

III.4.3.8 Energy dependence

Because of the low atomic number of both lithium and fluorine, the energy dependence of LiF thermoluminescence is small compared with that of other common dosimeters (11) (see Figure (II.10)). The TL response of TLD-700 to Co^{60}gamma radiation of different effective keV has been investigated between 30 keV effective and 1.2 MeV (Figure (III.22)).

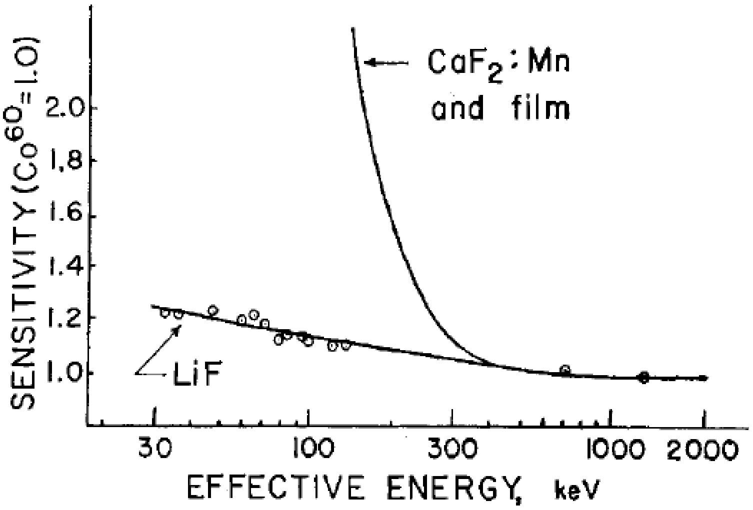

Figure III.22: Energy dependence of LiF compared with that of other dosimeters [25].

The sensitivity, measured in light emitted per r/mg, relative to Co^{60}gamma rays is notably constant especially compared to the responses of the other dosimeters. For dosimetry, it is obviously desirable to have a detector which exhibits a constant response over a wide range of energies, there for LiF (with low Z) is preferred [15].

References

[1] Es, Hendrickje Jacoba van. Thermoluminescence Dating of Sediments Using Mineral Zircon, submitted to University of Groningen, 2008.

[2] McKeever, S.W.S.Thermoluminescence of Solids; Cambridge University Press: Cambridge, UK, 1988;.

[3] S. W. S. McKeever, R. Chen.Theory of Thermoluminescence and Related Phenomena, World Scientific: Singapore, 1997.

[4] Bos, A.J.J., Theory of Thermoluminescence, Radiation Measurements, Vol 41, p45-56, 2007.

[5] Furetta, C.Handbook of thermoluminescence, New Jersy:World Scientific, 1987.

[6] Sunta, C. M.Unraveling Thermoluminescence, Springer Series in Materials Science; Springer: New Delhi, India, Vol 202, 2015.

[7] Bos, A. J. J.High Sensitivity Thermoluminescence Dosimetry, Nucleaire Instrument and Methods in Physics Rreaserch B, Vol 184, pp 3-28, 2001.

[8] Piters, T.M. A Study into the Mechanism of Thermoluminescence in a LiF:Mg,Ti Dosimetry Material, submitted to Interfaculty Reactor Institute, Delft University of Technology, 1993.

[9] M. Nahar, M. kamal, M. I. Chowdhury and M. N. Mustafa.Study on Thermoluminescence (TL) Properties of LiF (TLD-100) and Natural Silicate Stone as Radiation Dosimeters, Bangladesh Journal of Physics, Vol 16, 39-47, 2014.

[10] Sani, S.F. Abdul.Characterisation of Defects and Thermoluminescence Yield of Novel Tailor-Made Doped Optical Fibres for Dosimetry, submitted to Centre for Nuclear and Radiation Physics University of Surrey, 2015.

[11] Mathur, V. K.Properties of Principle TL Dosimetres, NSWC TR 83-382, MaryLand : Naval Surface Weapons Center, 1983.

[12] Chen, R. and Pagonis, V. Thermally and Optically Stimulated Luminescence—A Simulation Approach; JohnWiley: Chichester, UK, 2011.

[13] Bøtter-Jensen, Lars. Development of Optically Stimulated Luminescence Techniques using Natural Minerals and Ceramics, and their Application to Retrospective Dosimetry,pp 13, 2000.

[14] J. Azor, C. Furett , and A. Scacco. Preparation and Properties of Thermoluminescent Materials, phys. stat. sol. (a), Vol 138, pp 10-46, 1993.

[15] McKeever, S.W.S. Thermoluminescence of Solids; Cambridge University Press: Cambridge, UK, 1988.

[16] Boyd, Wesley Leon. Using Thermoluminescent Dosimeters to Measure the Dose From High and Low Energy X-Ray Sources, submitted to University of Nevada, Las Vegas, 2009.

[17] Furetta, C.Handbook of thermoluminescence, New Jersy : World Scientific, 1937.

[18] M. Nahar, M. Kamal, M. I. Chowdhury and M. N. Mustafa.Study on Thermoluminescence (TL) Properties of LIF (TLD-100) And Natural Silicate Stone as Radiation Dosimeters, Bangladesh Journal of Physics, Vol 16, 39-47, 2014.

[19] Mathur, V. K.Properties of Principle TL Dosimiters, 1983. NSWC TR 83-382, MaryLand : Naval Surface Weapons Center.

[20] Goodman, H.J. Structural Factors Influencing Thermoluminescence in Ionic Crystals, submitted to Imperial College of Science and Technology, England, 1977.

[21] S. Del Sol Fernández, n, R.García-Salcedo, J.Guzmán Mendoza, D.Sánchez-Guzmán, G. Ramírez Rodríguez, E.Gaona, T.Rivera Montalvo.Thermoluminescent Characteristics of LiF:Mg,Cu,P and CaSO4:Dy for Low Dose Measurement, Applied Radiation and Isotopes, Vol 111, pp 50–55, 2016.

[22] Sani, S.F. Abdul. Characterisation of Defects and Thermoluminescence Yield of Novel Tailor-Made Doped Optical Fibres for Dosimetry, submitted to Centre for Nuclear and Radiation Physics University of Surrey 2015.

[23] S. W. S. McKeever, R. Chen. Theory of Thermoluminescence and Related Phenomena, World Scientific: Singapore, 1997 .

[24] J. R. Cameron, F. Daniels, Noye Johnson, G. Kenney. Radiation Dosimeter Utilizing the Thermoluminescence of Lithium Fluoride, SCIENCE, Vol. 134, 1961.

[25] J. R. Camron, D. Zimmerman, G. Kenney, R. Buch, R. Bland, R. Grant. Thermoluminescent Radiaition Dosimetry Utilizing LiF, Health Physics Pergamon Press 1964. Vol 10, pp. 25-29.

CHAPTER IV :

Influence of wrong positioning of water phantom and ionization chamber on the accuracy of the treatment planning in external radiotherapy

In this chapter

IV.1 Introduction

Radiotherapy treatment outcome is directly related to the accuracy in the delivered dose to the patient that is dependent on the accuracy of beam data used in the treatment planning process. These data are obtained during the initial commissioning of the linear accelerator and are taken as the standard data for clinical use. In order to be able to operate the TPS in right clinical use routinely, it was imperative to proceed to a systematic checking of these basic data periodically through some dosimetric measurement performed by using suitable ionisation chamber and water phantom. Indeed, the basic necessary dosimetric data for treatment planning by the TPS are: percent depth dose (PDD) profiles for open field, the dose off-centre ratio (OCR) profiles for open fields, the collimator opening factors (FOC), diagonal dose profiles for open fields, transmission and dose calibration factors (monitor unit and dose unit correspondence (MU/Gy)) [1-4]. In this work, it was question to study the influence of an involuntary wrong positioning of water phantom and ionization chamber on the accuracy of the necessary beam data, namely: the PDD, the OCR and the absolute reference dose. Consequently, it was question of check if such bias conditions can affect the treatment planning accuracy in external radiotherapy around the ClinacIX accelerator of the fighting against cancer centre (CLCC) of Setif.

IV.2 Interest of water phantom in the measurement of beam data

The reference medium for dosimetry in radiotherapy is a phantom with material that can absorb and diffuse ionizing radiation in the same way as organic human tissue. For this purpose, the phantom must have electronic and volumetric densities that are approaching those of the human tissue. Indeed, water which has these peculiarities (the human body is more than 80% of water) is the most frequently phantom used. Such phantom is recommended by many and latest dosimetric protocols [5]. By using this phantom, there are many types of data that must be acquired during radiotherapy machine and treatment planning system (TPS) commissioning particularly the percent depth dose (PDD) profiles and the dose off-centre ratio (OCR) profiles for open field. Necessary dosimetric beam data are collected with a scanning water phantom; typically, a plastic tank filled with water to a level deep enough to allow PDD and OCR measurements to a maximum depth of 40 cm on the central axis. The size of the water tank should be large enough to allow scanning of beam profiles up to the largest field size required e.g., for photon beams, 40x40 cm^2 with sufficient lateral buildup 5 cm and over scan distance. Some planning systems require larger lateral scans and diagonal profiles for the largest field size and at a depth of 40 cm for modeling. To determine the appropriate size of the scanning tank, the over scan and the beam divergence at 40 cm depth should be considered. A factor of 1.6 times the maximum field size should provide a safe limit. Simple calculation shows that a tank size of 75x75 cm^2 is an optimum recommended size. If the scanning software does not have the ability to perform diagonal scans, the pedestal table should be rotated to acquire the desired data. In general, collimator rotation does not provide the flattening filter information that diagonal profiles are intended to provide, and hence, such data should not be taken with collimator rotation.

IV.3 Materiel and methods

IV.3.1 Materiel used and experimental setup

IV.3.1.1 Experimental setup N°1

This experimental setup is used for PDDs and OCRs measurement. It includes the following parts:

1. Automatic water phantom MP3 PTW 3D

The water tank represents one of the important measurement elements in radiotherapy. The measurements that can be performed on it are: the depth yield, the dose profile, the absolute dose... The water used is distilled water, thus making it possible to best represent human tissue. It is for this latter reason that the majority of the measurements required in radiotherapy are carried out in water. The water tank used in this work is made up of three motors and three potentiometers (for independent displacement) allowing the displacement of the ionization chamber in the three planes of space (3 directions) [6]. Thus, one can easily measure an absolute reference dose in the center of the field at 10 cm deep, a yield in depth as well as a lateral dose profile. The water tank is in the form of a cubic tank with a total capacity of 0.148 m^3 (length: 59.4 cm, width: 49.6 cm, depth: 50.25 cm) (Figure IV.1). The installation of the tank in the measurement position must be very accurate to avoid any wrong measurement.

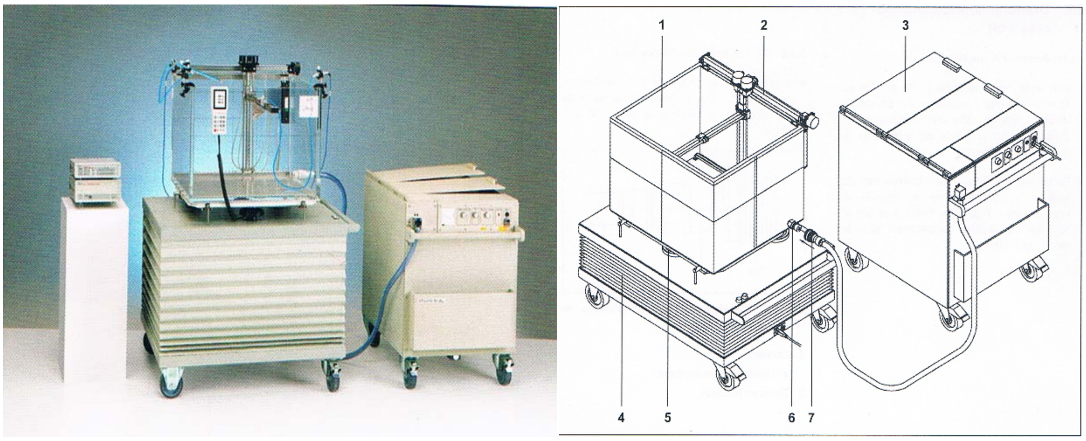

1 *Récipient en verre acrylique*
2 *Mécanisme de mouvement*
3 *Réservoir d'eau*
4 *Chariot élévateur*
5 *Dispositif d'ajustage*
6 *Raccord enfichable*
7 *Couplage*

Figure IV.1: Water tank MP3 PTW

2. Controller

This element is used for the data acquisition by controlling communication between the water tank (ionization chamber and positioning motors) and the data acquisition, display and storage software "*Mephysto*". When information on the next position of the ionization chamber is transmitted from "*Mephysto*", the controller sends a signal to the tank that start moving the ionizing chamber to this desired spatial position by stepper motors. The controller also allows that the charge measured (dose) by the electrometer is transmitted to the "*Mephysto*" software for storage and interpretation (Figure IV.2).

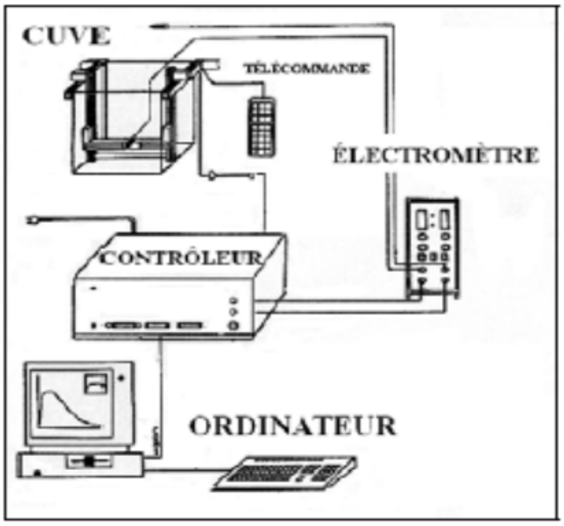

Figure IV.2: Controller illustration and mounting

3. MP3 Electrometer

The MP3S electrometer from PTW FREIBURG was used with the ionization chambers M 31010 PTW and M 31013 PTW for the measurement of PDDs and dose profiles. This electrometer measure electrical signal induced by the charges collected by the ionization chamber and then transmits the information to the "*Mephysto*" software through the controller for display and storage (Figure IV.3). The electrometer has a monitoring and control console. This control console is used to position the ionization chamber in the desired initial or final position. It can be connected either to the electrometer or to the water tank.

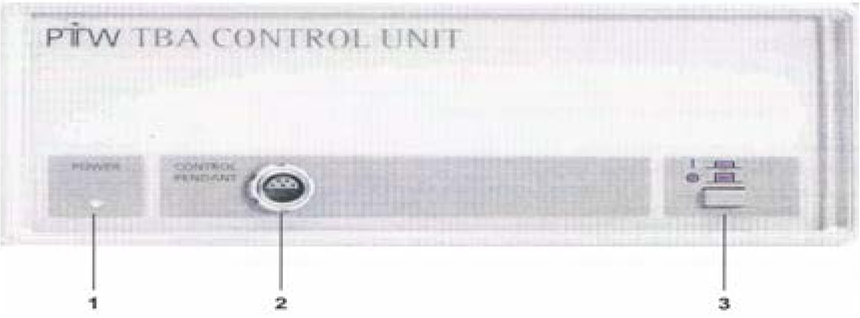

1 *DEL de mise en service (alimentation électrique)*
2 *Prise de raccordement pour le TBA CONTROL PENDANT (appareil de commande portatif)*
3 *Interrupteur Marche/Arrêt*

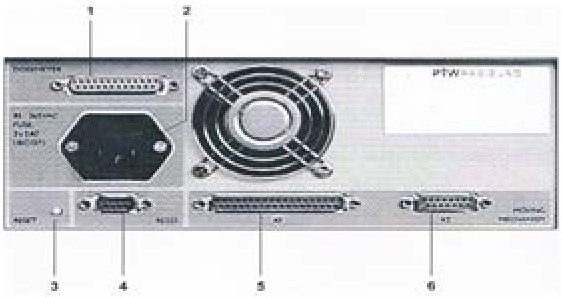

Face arrière de la TBA CONTROL UNIT

1 *DOSEMETER, prise pour dosimètre*
2 *Alimentation électrique et fusibles secteur*
3 *Touche RESET*
4 *Interface RS-232*
5 *K1 ; prise de raccordement du câble de commande pour mécanisme de mouvement*
6 *K2 ; prise de raccordement du câble moteur pour mécanisme de mouvement*

Figure IV.3: MP3 Electrometer

When installing the water tank, the control console is connected to it in order to position the ionization chamber at the isocenter of the linear accelerator. The three coordinates of the space are represented by the indications A, B, C, with a displacement precision of 0.1 mm. The movement of the three axes uses two speeds. The movement control can be done by a step varying from 0.1 mm to 1mm. It is possible to create limit displacement positions preventing the ionization chamber from coming to butter against the walls of the tank (Figure IV.4).

Figure IV.4: Portable control unit

4. Data acquisition software *Mephysto* PTW

This software collects data after an irradiation. The displacement of the ionization chamber via the controller and the displacement motors is carried out from this software. After defining the field size, the energy, the source / water surface distance (SSD, Skin Source distance), we can perform our measurements on the PDDs and dose profiles OCRs (Figure IV.5).

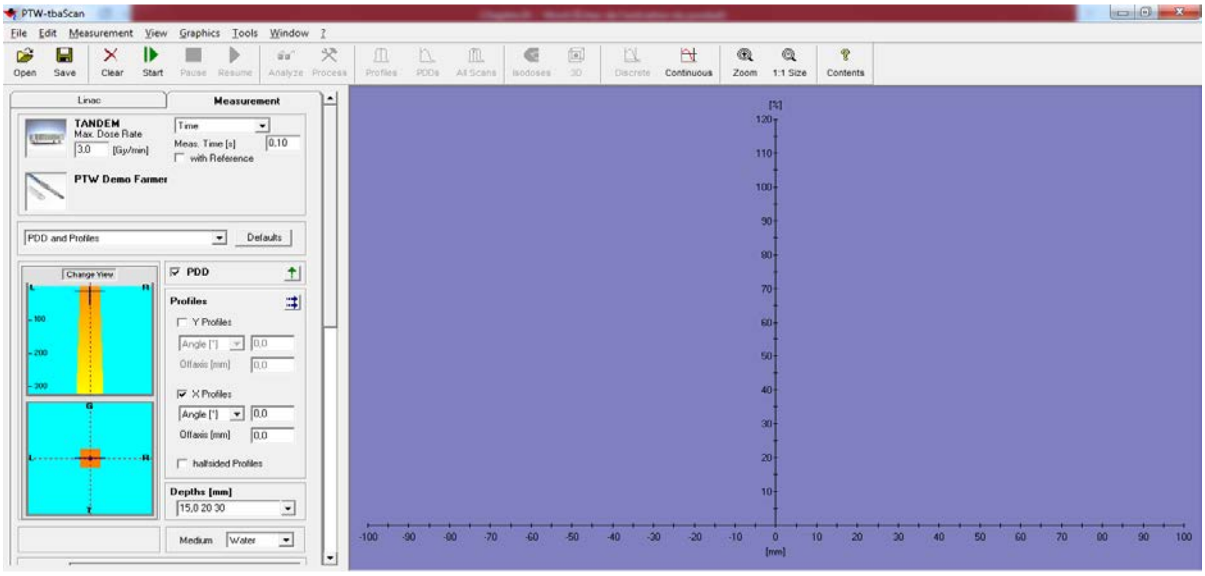

Max. Dose Rate 3.0 [Gy/min]
Time
Meas. Time [s] 0.10
☐ with Reference
PDD and Profiles
☑ PDD
Profiles
☐ Y Profiles
Angle [°] 0,0
Offaxis [mm] 0,0
☑ X Profiles
Angle [°] 0,0
Offaxis [mm] 0,0
☐ halfsided Profiles
Depths [mm] 15,0 20 30
Medium Water

Figure IV.5. Interface of the *Mephysto* PTW data acquisition software

IV.3.1.2 Experimental setup N°2

This setup was used for the measurement of the absolute dose at the reference position at a depth of 10 cm in water. It includes the following elements:

1. Water phantom PTW MP1

The PTW MP1 1D water phantom is a remote-controlled motorized phantom used in our work for the measurement of absolute doses at the reference position. It can also be used for the measurement of PDD depth yields for photon and electron beams (Figure IV.6). The dosimetric data acquisition is carried out in accordance with the AAPM TG-51, IAEA TRS 398 and DIN 6800-2 protocols. The phantom is equipped with a fixing system to install the Semiflex, Farmer, Markus or Roos type ionization chambers. The main characteristics of this phantom are given in Table (IV.1).

Figure IV.6: Water phantom PTW MP1

Table IV.1: Main characteristics of the PTW MP1 phantom

Type	Water phantom 1D PTW MP1
Application	Absolute dosimetry and measurement of the dose deep in water according to the AAPM TG-51, IAEA TRS 398 and DIN 6800-2 protocols
Resolution	0.1 mm
Tank material	PMMA
Volume	38 414,545000cm^{3}ou 38.41 L
External Dimensions (High*Lenght*Width)	(5320x320x370) mm^3
Wall thickness	1cm
Measuring depth	0 à 254 mm
Weight (empty)	10.3 Kg

2. UNIDOS Webline Electrometer

The UNIDOS Webline electrometer from PTW FREIBURG is used with ionization chambers in photon mode and in electron mode. It is a reference electrometer (Figure IV.7). It was calibrated with the 0.6 cm3 reference chamber (Semiflex PTW 30013) in absorbed dose for high energy photons and the Markus type 23343 chamber for electrons with energies of 6, 9, 12, 16 and 20 MeV. The absolute dose measurement is provided in terms of the total charge collected (ηC). Just put the electrometer in "Coulomb" mode to measure the charge collected. In order to overcome the background noise from the ionization chamber, the device is equipped with a reset.

Figure IV.7: UNIDOS Webline Electrometer

IV.3.1.3 Ionization chambers used in the two experimental setups

In this work we used two types of ionization chambers: the PTW Semiflex 0.3 cm^3 (PTW31013) (Figure IV.8), and the PTW Semiflex 0.125 cm^3 (PTW 31010) (Figure IV.9) [7].

The 0.3 cm^3 chamber was used for the measurement of the absolute dose and also as a reference for the measurement in relative dosimetry of PDDs and dose profiles OCRs. The main characteristics of this detector are given in Table (IV.2).

Figure IV.8: Ionization chamber 0.3 cm^3 Semiflex type 31013

Table IV.2: Main characteristics of the 0.3 cm^3 Semiflex chamber type 31013

Wall of sensitive volume	Materials	0.55 mm of PMMA, 1.19 g/cm^3
		0.15 mm of Graphite, 0.82 g/cm^3
	Total wall area density	78 mg/cm^2
Dimension of sensitive volume	Radius	2.75 mm
	Length	16.25 mm
Central electrode	Material	Aluminium 99.98%
	Diameter	0.9 mm
Build-up cap	Material	PMMA
	Thickness	3 mm
Working voltage	100-400 V	
Radiation enrgy range	Photons	100 kV-50 MV
	Electrons	10 -45 MeV
	Protons	50-270 MeV
Maximum dose rate	+99.5 % saturation	14 Gy/s
	+99.0 % saturation	28 Gy/s
Maximum dose rate per pulse	For 99.5 % saturation	0.8 mGy
	For 99.0 % saturation	1.5 mGy

Field size	(4 x 4) cm2-(40 x 40) cm^2
Air pressure	700-1060 hPa
Working Temperature	10-40 °C
Working Humidity	10 -80 %, max 20 g/m3
Ion collection time	80 μs

The 0.125 cm^3 ionization chamber was used for the measurement of PDDs and dose profiles OCRs. The main characteristics of this detector are presented in Table IV.3.

Figure IV.9: Ionization chamber 0.125 cm^3 Semiflex type 31010

Table IV.3: Main characteristics of the 0.125 cm3 Semiflex chamber type 31010

Wall of sensitive volume	Materials	0.55 mm of PMMA, 1.19 g/cm^3
		0.15 mm of Graphite, 0.82 g/cm^3
	Total wall area density	78 mg/cm^2
Dimension of sensitive volume	Radius	2.75 mm
Central electrode	Length	6.5 mm
	Material	Aluminium 99.98
	Diameter	1.1 mm
Build-up cap	Material	PMMA
	Thickness	3 mm
Working voltage	100-400 V	
Radiation enrgy range	Photons	140 kV-50 MV
	Electrons	10 -45 MeV
	Protons	50-270 MeV
Maximum dose rate	+99.5 % saturation	6 Gy/s
	+99.0 % saturation	12 Gy/s
Maximum dose rate per pulse	For 99.5 % saturation	0.5 mGy
	For 99.0 % saturation	1mGy
Field size	(3 x 3) cm^2-(40 x 40) cm^2	

Air pressure	700-1060 hPa
Working Temperature	10-40 °C
Working Humidity	10 -80 %, max 20 g/m3
Ion collection time	100µs

IV.3.1.4 Water tank installation

Installing the water tank is a very important step for data acquisition. Its installation must be as precise as possible in order to guarantee the accuracy of the measurements made. In its installation, it is first necessary to make the center of the tank coincide with that of the directing beam of the linear accelerator. Just use the reticule located in the head of the accelerator and have it superimposed on the cross at the bottom of the tank. In order to facilitate the positioning of the tank, it is possible to use the positioning lasers installed on the walls of the accelerator room. The tank is then filled with distilled water. The water source / surface distance (SSD) should be set to 100 cm. This distance is adjusted using a rangefinder. This will also make it possible to position the ionization chamber at the iso-center of the linear accelerator.

The tank's parallelism with respect to the ground (reference) is done by checking its vertical and horizontal inclinations with level meters of control. Figure (IV.10) illustrates the installation of the water tank.

Figure IV.10: Installation of the water tank

The last step in installing the tank is to fix the ionization chambers (Figure IV.11). For PDDs and dose profiles, the measuring chamber (0.125 cm^3 PTW31010) is fixed on the movable arms of the tank so that it can be moved. However, care must be taken to match the sensitive area of this ionization chamber with the iso-center of the linear accelerator. The reference chamber (0.3 cm^3 PTW M 31013) is placed on a support above the tank. The latter must be placed at the edge of the light field reproducing the field the shape of the beam used. The two chambers are then connected to the MP3 electrometer, which in turn is part of the *Mephysto* software. For the measurement of the absolute dose, the PTW MP1 1D phantom water tank is used with the 0.3 cm^3 ionization chamber (PTW M31013). For this measurement, the chamber is fixed at the reference position, i.e. at a depth of 10 cm in the water phantom.

Figure IV.11: Relative chamber fixed on the movable arms (green circle at the bottom) and reference chamber positioned on the edge of the selected field (red circle at the top)

IV.3.2 Methods

IV.3.2.1 Considered biased beam data measurement scenarios

The knowledge of the dosimetric parameters of the high-energy photon beams delivered by a linear accelerator is of great importance for the treatment planning in routine radiotherapy. To this end, we have imagined and implemented possible wrong measurement setup scenarios (systematic errors) of certain photon beam reference data in order to study their influence on dose calculation by the TPS. In this work, it was a question of studying the influence of an involuntary wrong positioning of the water phantom and the ionization chamber on the precision of the collected beam data and consequently on the calculated dose. To do this, a real and appropriate treatment case was considered to elucidate the effect of such measurement error scenarios on the real treatment planning accuracy. Indeed, we have to compare between the doses delivered to the most important organs and to the programmed target volume (PTV) and the dose indices by the analysis of dose-volume histograms (HDV) for the two cases without and with the introduction of positioning errors. The dose coverage of PTV was evaluated using the heterogeneity index (*HI*), the uniformity index (*UI*) and the conformity index (*CI*) defined as follows [8-9]:

$$HI = \frac{D_{2\%} - D_{98\%}}{D_{50\%}}, \qquad \text{(IV. 1)}$$

where $D_{2\%}$ is the dose of 2% of the programmed target volume, $D_{98\%}$ is the dose of 98% of the programmed target volume, and $D_{50\%}$ is the dose of 50% of the target volume [8-9];

$$UI = \frac{D_{5\%}}{D_{95\%}}, \qquad \text{(IV.2)}$$

where $D_{5\%}$ is the dose of 5% of the programmed target volume, and $D_{95\%}$ is the dose of 95% of the programmed target volume [8-9];

$$CI = \frac{PTV_{95\%}}{PTV}\ , \qquad \text{(IV.3)}$$

where, PTV is the programmed target volume and $PTV95\%$ is the volume covered by 95% of the prescribed dose.

IV.3.2.1.1 Positioning bias of the water phantom

In this first scenario, the PDD measurements and the dose profiles OCRs were carried out using the water phantom (PTW MP3) slightly inclined with a reasonable error angle of 1° to the left relative to the beam incidence. Measurements were made on the Varian Clinac IX linear accelerator for a 18 MV photon beam, 10x10 cm^2 aperture, and with a source-skin distance of 1000 mm (SSD = 1000 mm). PPDs and dose profiles were measured by two open air ionization chambers: the first having a volume of 0.125 cm^3 (PTW 31010) and the second reference volume chamber of 0.3 cm^3 (PTW 31013). For this measurement, the phantom used automatically moves in three directions (x, y, z) during signal capture.

IV.3.2.1.2 Positioning bias of the ionization chamber

For this second scenario, the measurement of the absolute dose was carried out using a well-positioned water phantom MP1 PTW D1, but this time the main axis of the ionization 0.3 cm^3 ionization chamber was slightly shifted from the water level by ~ 5 mm upwards.

IV.4 Results and discussion

The wrong positioning of the MP3 water phantom considered in this work had no effect on the PDDs because the inclination does not affect the depth covered in the water (the depth is the same with or without the introduction of this phantom tilt bias). In addition, a relatively slight effect was observed on the dose profiles OCRs. Figure (IV.12) shows the reference OCR dose profiles (with right phantom positioning) and the OCR dose profiles with the introduction of the phantom position error (1° tilt) for a field size of 100 mm and at different depths in the water (31, 50, 100, 200 and 300 mm).

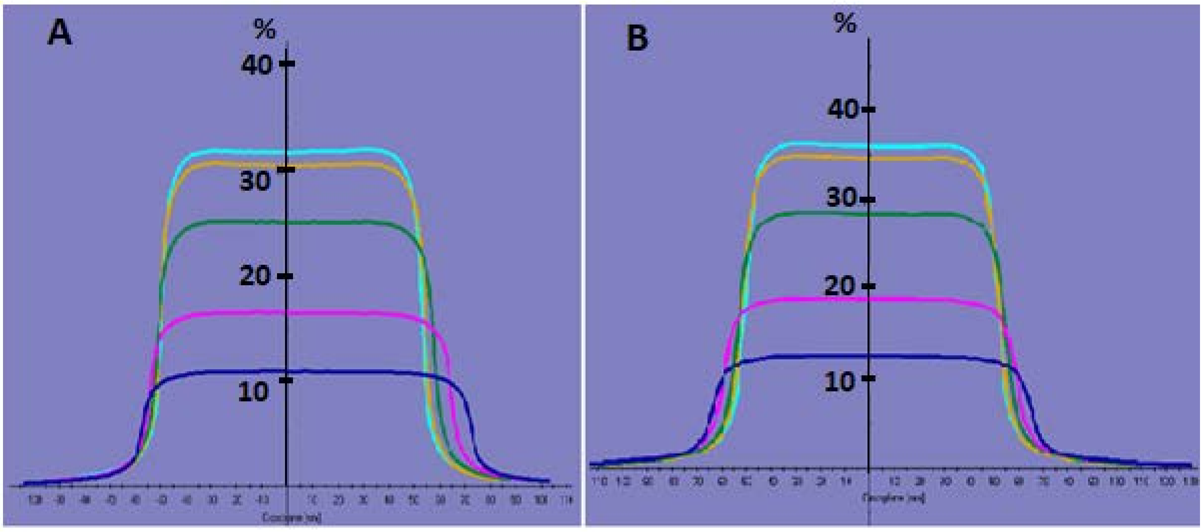

Figure IV.12: OCR dose profiles with introduction of the phantom positioning error (A), and the reference OCR dose profiles without positioning error (B)

The wrong positioning of the water phantom considered has led to some changes in the flatness and symmetry of the OCR dose profiles. Differences of 0.5% and 1.11% were observed respectively on the flatness and the symmetry for a field size of 30x30 cm^2 and a depth of 100 mm (Table IV.4).

Tableau IV.4: Induced changes in flatness and symmetry of the OCR dose profiles due to the considered improper positioning of the water phantom

	Reference OCR	**OCR with positioning error**	**Difference (%)**
Flatness (%)	1.64	2.14	0.5
Symmetry (%)	0.37	1.48	1.11

In addition, for the scenario of wrong the ionization chamber positioning, it was observed that this positioning bias induced a slight variation on the reference dose at the calibration depth (Z = 100 mm) for a field size of 100 mm and for a source-axis distance of 1000 mm (SAD = 1000 mm). The reference dose therefore changes from 0.94 Gy (reference) to 0.97 Gy (with positioning bias), i.e. with ~ 3% of difference.

To elucidate the effects of these two positioning biases on the treatment planning in radiotherapy, comparisons of calculated doses by the TPS for various organs and structures were made by comparing new HDVs to reference HDVs. The reference HDVs for the most important structures and volumes are presented in Figure (IV.13).

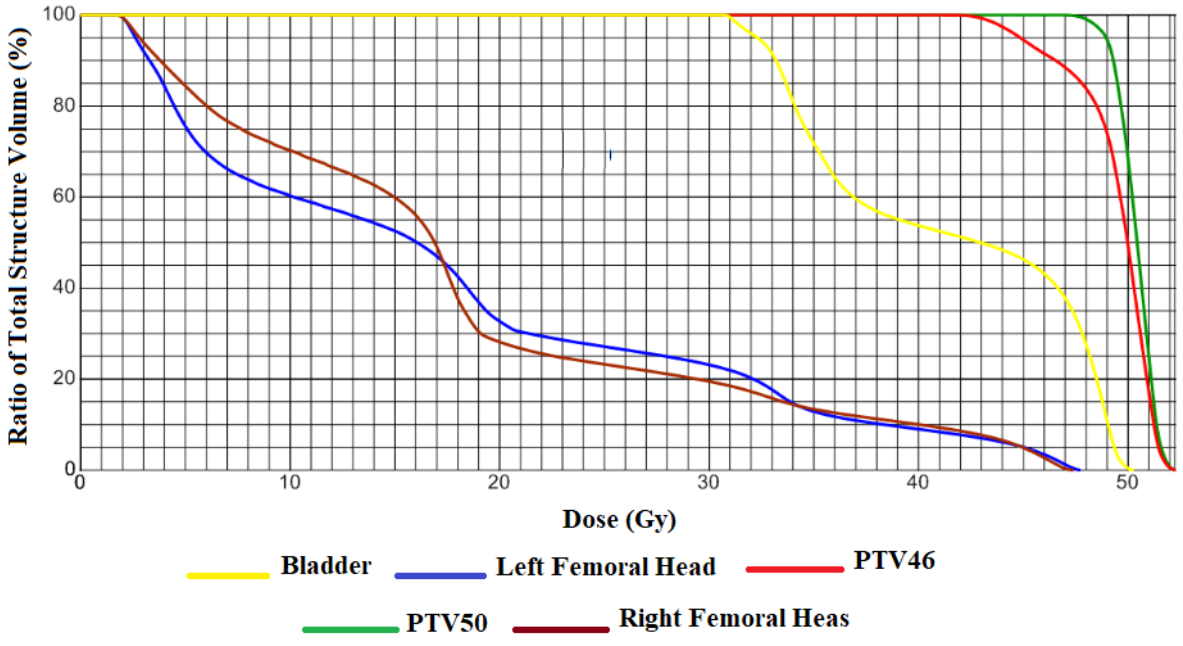

Figure IV.13: Reference HDVs for the most important organs and structures

The error scenarios considered in this work had no significant effect on the precision of treatment planning, see Table (IV.5). The wrong ionization chamber and the water phantom positioning considered induced slight changes on the reference HDVs, in particular on the target doses and the dose covering indices as presented in Table (IV.5).

Tableau IV.5: Changes observed in the doses (in volume) and the dose covering indices of the main organs, volumes and structures by the positioning bias considered.

Volume/Structure	**Dose (Gy)**			
		Reference	**Ionization chamber position bias**	**Water phantom position bias**
PTV 50 Rectum	Dmax	52.281	52.282	52.206
	D50%	50.434	50.434	50.399
	D98%	48.385	48.383	48.423
	D95%	48.956	48.956	48.956
	D2%	51.820	51.821	51.757
	D5%	51.576	51.576	51.520
	Dose covering index			
	CI	0.99	0.99	0.99
	HI	0.068	0.068	0.066
	UI	1.053	1.053	1.052
	Dose (Gy)			
Bladder	Dmax	50.283	50.283	50.281
	Dmin	30.745	30.744	30.709
	D2%	49.636	49.636	49.651
Left Femoral Head	Dmax	47.729	47.730	47.718
	Dmin	1.781	1.781	1.700
	D2%	46.665	46.664	46.65
Right Femoral Head	Dmax	47.398	47.398	47.421
	Dmin	1.597	1.596	1.513
	D2%	46.276	46.277	46.300

In this work, it was well verified that the wrong positioning of the ionization chamber considered had no direct impact on the value of absolute reference dose. Whereas the wrong water phantom positioning did not have any impact except on OCR dose profiles.

An in-depth analysis of the obtained results presented above allows us to note that:

- The asymmetrical OCR dose profiles observed by tilting the water phantom with a bias of 1° had no significant impact on the accuracy of the dose calculation and therefore on the radiotherapy treatment planning.

- The slight shift in the position of the ionization chamber with respect to its central axis by ~ 5 mm towards the top of the water level did not affect the clinical dosimetry calculated by the TPS.

- No significant differences in the PTV dose covering indices between the reference situation and the wrong positioning situation considered.

- The PDDs and OCRs dose profiles obtained for the wrong positioning situations considered had no direct impact on the accuracy of the radiotherapy treatment planning.

- No significant differences on the doses to be delivered to organs at risk between the reference situation and the wrong positioning situation considered.

IV.4 Conclusions

In this work, we studied the influence of involuntary but plausible bad positioning of the PTW MP3 water phantom and the ionization chamber on the collection of beam data around the Clinac IX accelerator. These beam data are necessary for external radiotherapy treatment planning with the TPS Varian Eclipse (11.0.31). The results obtained for the considered scenarios showed that the biases considered (tilt by 1° of the water phantom and shift by 5 mm of the ionization chamber) had no significant impact on the dose calculation and the whole treatment planning work for the clinical case considered. The differences in terms of new calculated doses remain within the limits authorized limits predefined by the International Commission on Radiation Units (ICRU) [10,11].

References

[1] Gibbons JP, Antolak JA, Followill DS, Huq MS, Klein EE, Lam KL, Palta JR, Roback DM, Reid M, Khan FM (2014) Monitor unit calculations for external photon and electron beams: Report of the AAPM Therapy Physics Committee Task Group No. 71, The international journal of medical physics research and practice 41(3). https://doi.org/10.1118/1.4864244

[2] Smilowitz, J et al. (2015) AAPM Medical Physics Practice Guideline 5.a.: Commissioning and QA of Treatment Planning Dose Calculations - Megavoltage Photon and Electron Beams. Journal of Applied Clinical Medical Physics 16(5):14-34

[3] Salomons G (2015) WE-AB-201-00: Treatment Planning System Commissioning and QA. Medical Physics 42(6): 3662-3663

[4] IAEA (2008) Commissioning of Radiotherapy Treatment Planning Systems: Testing for Typical External Beam Treatment Techniques. IAEA-TECDOC-1583.

[5] Cameron M, Cornelius I, Cutajar D, Davis J, Rosenfeld A, Lerch M, Guatelli S (2017) Comparison of phantom materials for use in quality assurance of micro-beam radiation therapy. J. Synchrotron Rad. 24: 866-876.

[6] PTW Water Scanning Systems, Document No. D817.199.00/00 2011-07 Wt. https://www.ptwdosimetry.com/en/products/mp3-water-phantom-system/. Accessed 15 April 2019.

[7] PTW, Ionizing Radiation Detectors including codes and practice, D165.229.00/08 2014-12. http://www.emf-japan.com/ptw/img/PDF/PTW_all_detectors.pdf. Accessed 11 April 2019.

[8] ICRU (2010) Prescribing, Recording, and Reporting Photon-Beam Intensity-Modulated Radiation Therapy (IMRT): Contents. Journal of the ICRU 10:1, NP:10.

[9] Feuvret L, Noel G, Mazeron JJ, Bey P (2006) Conformity index: a review. International journal of radiation oncology, biology, physics 64:333–342.

[10] Landberg, T, et al. (1993) Journal of the International Commission on Radiation Units and Measurements (ICRU) Report 50, 26 (1).

[11] Landberg, T, et al. (1999) Journal of the International Commission on Radiation Units and Measurements (ICRU) Report 62, 32(1).

CHAPTER V :

Dosimetric control and comparison of 3D-CRT versus IMRT in the treatment of lung cancer

In this chapter

V.1 Introduction

After many recommendations and advices, the IMRT was recently implemented at the radiotherapy service of CLCC-Setif, Algeria. The installation was done by a team of medical physicists and clinicians from the same department. Compared to the 3D conformal radiotherapy technique (3D-CRT) this technique responds better to certain dosimetric requirements and constraints, especially for certain complex treatment cases. The present work was undertaken for the dosimetric evaluation of IMRT and its contribution to better dosimetric management of certain radiotherapy treatments such as lung cancer which is difficult to treat with 3D-CRT. Indeed, the results of the Rando phantom study published by Bouacid et al. have shown that 3D-CRT has relatively high differences between the calculated and measured doses, particularly in regions close to the interfaces of heterogeneity in the case of lung cancer [1].

Although many studies support the use of IMRT for the treatment of lung cancer, the question is whether IMRT could help overcome such problems of point dose differences close to heterogeneities. It is therefore certain that the implementation of this technique involved clinical and technical challenges. IMRT being a more complex technique than 3D-CRT would certainly require more treatment planning work in terms of dose calculation and optimization. In fact, the motivation that arises behind the implementation of IMRT is manifested in the possibility of processing a large target volume with great geometric precision and more rigorous compliance with dose constraints, especially on organs at risk (OAR) for certain types of cancer.

In this part of the thesis project, IMRT, which uses the AAA (Anisotrpic Analytical Algorithm) dose calculation algorithm of 3D-CRT combined with its own dose planning and dose-volume optimization tools, is used for the same treatment planning carried out on a phantom and simulating a real case of lung cancer undertaken by Bouacid et al. with 3D-CRT [1]. The TPS Varian Eclipse (11.0.31) treatment planning system is used for this treatment planning. Through this study, we intend to check whether IMRT contributes to solving the problem of heterogeneities compared to 3D-CRT and how it contributes to ensuring optimal dose coverage of PTV while better sparing OARs. The objective of this work is also to verify and compare the point doses measured at different depths using the thermoluminescent dosimeter type TLD700 on the Rando phantom. In addition, this study also aimed to examine the compatibility of the dose-volume optimization algorithm (DVO) used in IMRT by the TPS to reduce the effect of heterogeneity on certain regions such as the interfaces between two heterogeneous media / homogeneous [2]. Finally, it was also a question of verifying whether the treatment plans validated during the calculation phase are valid experimentally by thermoluminescence dosimetry (TL) and this, according to the recommendations of the ICRU on the delivery of the dose to PTV reported in reports 50 and 62 [3-4].

V.2 Materiel et methods

V.2.1 Materiel

V.2.1.1 Linear Accelerator ClinacIX

Linear accelerators are used in radiotherapy to produce high energy ionizing radiation (up to 25 MeV). The linear accelerator Varian Clinac® iX SN5818 from CLCC-Sétif is used in this research work (Figure V.1). The technical characteristics of this accelerator are as follows:

- Photon energy: two possible energy: X6 and X18 MV (i.e. 6 and 18 MeV).
- Energy of the electrons: 6, 9, 12, 16 and 20 MeV.
- Dose rate: 100 to 400 monitor unit per minute (MU/min).
- Multi-Leafs Collimator (MLC): 120 leafs

Figure V.1: Varian Clinac® iX SN5818 Linear Accelerator

V.2.1.2 Rando Anthropomorphic Phantom

The RANDO phantom presents is an invaluable simulation and dosimetry aid device used for radiotherapy treatment planning simulation and for the dosimetric verification of radiotherapy treatment plans before application on real patient. It allows the establishment of a detailed map on the dose distribution. The detailed dosimetric information that it provides are very useful for the assessment of a patient's treatment plan and for the quality assurance of treatment planning system (TPS).

The male physical version of RANDO® phantom used in this study represents a man of average height: 175 cm in height and 73.5 kg in weight (Figure V.2). The phantom is made up of several numbered layers (slices) 2.5 cm thick each (see figure (V.2)). Each slice of the phantom has holes distributed over its entire surface to hold the TLD dosimeters. These holes are occupied by removable and cutable plastic plugs which allow the insertion of TLD dosimeters at the desired depth. The phantom is made with a natural human skeleton around which the different tissues are cast. Thus, two materials simulating human tissue are used to for manufacture of RANDO phantom: one is equivalent soft tissue material and the other one is equivalent lung tissue. These two materials are chosen to have the same absorption and diffusion characteristics for ionizing radiation generally used in radiotherapy. The lungs are molded to follow the contours of the human rib cage.

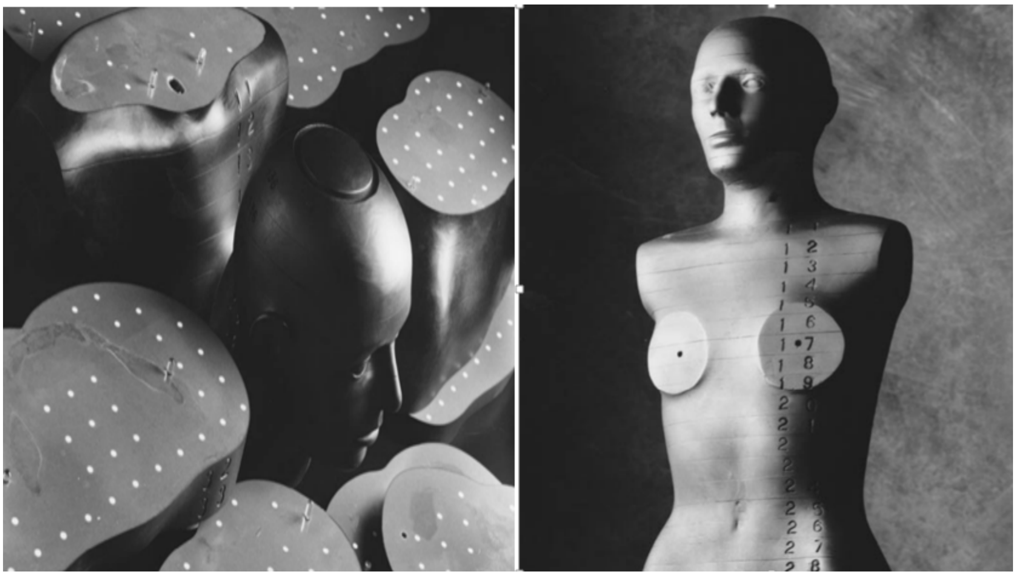

Figure V.2: Rando Phantom

The soft tissue material has an effective atomic number and mass density which simulates muscle tissue with randomly distributed fat. It should be noted that small air bubbles may appear on the CT scans of the RANDO phantom. These bubbles occur during the molding process of structural materials and are small enough to have no significant effect on the dose deposition. The lung material has the same effective atomic number as real lung tissue with a density that simulates the lungs in a median respiratory state. The molded lungs are well-shaped in order to fill and to fit well the rib cage.

V.2.1.3 Thermoluminescent detectors TLD

The thermoluminenscent detectors used in the framework of this work are the TLD-700 which are based on Fluorine of Lithium doped with Magnesium and Titanium (LiF: Mg, Ti). In external radiotherapy TLD-700 are used because they are equivalent to human tissue (Zeff = 8.18); which is an essential dosimetric advantage for effective and real verification of the doses delivered to the patient. In the present work, *ThermoFisher*” SNO78835 TLD-700 chips with dimensions of: 3.2 x 3.2 x 0.89 mm^3 were used for the measurement of the dose. In this context, it was necessary to characterize these TLDs by establishing their TL-Dose response curve before using them to determine the dose from the intensity of the measured TL signal. It must be noticed that the same TLD’s characterization work carried out in 3D-CRT by Bouacid et al. is repeated [1]. This is due to the fact that the same TLDs were re-used for our case study on IMRT and its comparison with 3D-CRT.

V.2.1.4 Thermoluminescence reader

In this work, the TL/OSL Risø DA-20 luminescence reader was used (Figure V.3) for thermoluminescence signals reading [5-6]. This reader includes three main modules:

1. Light detection system (PMT, photomultiplier);
2. Optical (OSL) or thermal (TL) luminescence stimulation system;
3. Additional sources of radiation: Beta source and X-ray generator.

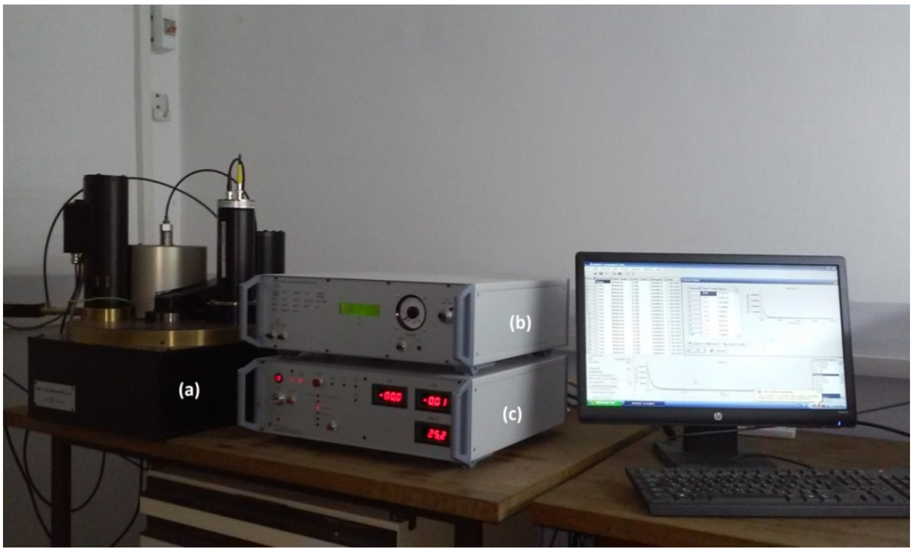

Figure V.3: RISØ TL / OSL-DA20 reader: a) Reader, b) Reader controller, c) X-ray generator controller

The light detection system includes a photomultiplier combined with several light filters. The luminescence stimulation system includes several types of diodes (LED) for optical stimulation (OSL) and a heating plate for thermal stimulation (TL). Additional in-situ irradiations can be performed by a beta source or an X-ray generator. The reader is able to analyze in one single pass 48 samples, each with its own programming sequence in terms of reading mode, heating conditions, additional irradiations, type of light filter, etc. The main characteristics of the reader used are summarized in the Table (V.1). For reading the signals and the additional irradiation, the TLDs are placed on stainless steel discs themselves placed in the different positions of the large rotating sample disc (Figure V.4). Reading of the TL signal and/or additional exposure is carried out by rotating the large sample disc from one reading or irradiation position to another.

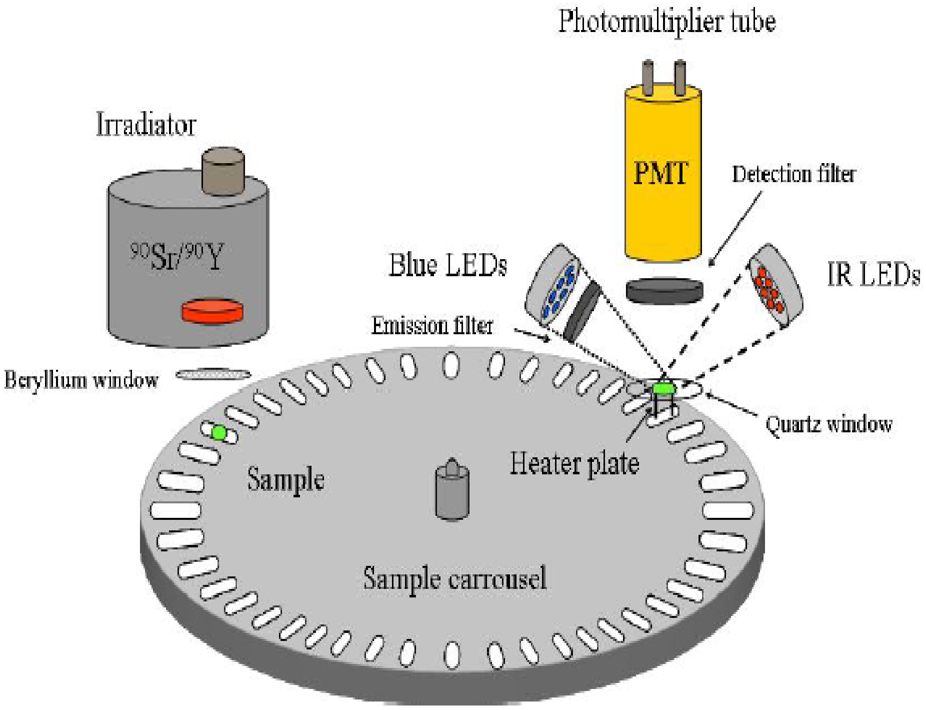

Figure V.4: Reading of luminescence signals and additional exposure (irradiation)

Table V.1: Main characteristics of the RISØ DA-20 TL/OSL reader

Photomultiplier	CsSb crystal with maximum detection efficiency between 200 and 400 nm and 0.4sr as solid detection angle
Heater material	Khantal with maximal temperature of 700°C and heating rate varying from 0.1 to 10°C/s
Beta source	^{90}Sr/^{90}Y, E_{max}: 2.27 MeV, Strength: 1.48GBq, Dose rate 0.1Gy/s in the quartz
X-ray Generator	Tungsten, 50 kV, 1 mA, 50 W, Dose rate in the quartz 2Gy/s

V.2.1.5 RW03 Phantom

Water is the standard and reference material in high energy photonic dosimetry. It is used for the measurement of reference data on the treatment beam in radiotherapy. Using the water phantom for calibrating the TLD-700s and verifying the accuracy of their response for deep dose measurement (PDD) is a necessary but a very complicated task for TLDs placing. To overcome this difficulty; we opted for the use of a solid water equivalent phantom (Real water phantom RW03). The RW3 T29672/U5 phantom used is made from polystyrene. The basic composition of this phantom is chosen to constitute a reference medium equivalent to human tissue with the same absorption and diffusion characteristics of the photons. RW03 contains in addition to polystyrene 2% in weight of Titanium oxide (TiO2). The RW03 was developed specifically for high energy photonic dosimetry (Figure V.5). The technical data and characteristics of the RW03 used are presented in the Table (V.2).

Figure V.5: RW03 sold phatom

Table V.2: Technical characteristics of the phantom RW03

Technical reference	RW3 phantom N° T29672/U5
Manufacturer	PTW-Freiburg, Germany
Use	Water equivalent phantom for high energy photon dosimetry
Composition	Polystyrene containing 2% in weight of Titanium dioxide (TiO2)

Plate thickness	1mm and 5mm
Plate dimensions	300×300 mm^2
Density	1.045 g/cm^3
Z/A ratio	0.536

V.2.2 Measurement methods and procedures

V.2.2.1 Creation of the virtual patient and IMRT treatment

In this work, a real patient with a lung lesion of 1394.1 cm^3 and corpulence similar to that of the Rando phantom was considered. This patient had been treated by the 3D conformal radiotherapy technique (3D-CRT) at CLCC-Sétif. Based on the same details and acquisition conditions of the real patient's CT scanning, similar CT data were acquired on the Rando phantom. A virtual patient was then created within the TPS by introducing Rando CT-scan data. Based on the prescribed dose, target volumes, and organs at risk (OAR) of the real patient, new IMRT treatment plans were generated and a new dose calculation was performed on the virtual patient (Rando). It is very important to mention that in order to have the same dose calculation conditions as the real patient already treated by 3D-CRT, meticulous work has been done to match the CT data and the contouring details of the real patient with those of Rando (virtual patient) treated this time by IMRT. Thus, the CT-slices of the real patient and the corresponding Rando CT-slices were readjusted and merged to form combined CT-slices allowing getting the reproduction of the same organs and structures contouring and delineations. The clinician was, thus, able to reproduce the same lesion and structures delineations of the real patient on the Rando virtual patient with exactly the same positions and the same planning target volume (PTV). It is also important to clarify that it was not necessary to change the Hounsfield numbers on the PTV region because they were close to those of the normal lung. This is due to the fact that the chosen case presents an early pulmonary metastasis and that lungs were just treated as a preventive measure. Regarding our comparison objective with 3D-CRT and as a reminder, the prescribed dose, the beams, the dose constraints of the treatment plans considered for 3D-CRT are presented in the Table (V.3) [1].

Table V.3: Details of the considered radiotherapy 3D-CRT treatment planning of lung lesion. PTV – planning target volume.

Prescribed dose	40 Gy given within 20 fractions (2Gy/fraction)									
Constraint on dose	95% of the dose covers 95% of the PTV									
Number of Fields	3 with 5 segments									
Beam ID	**Technique**	**Energy(MeV)**	**Field weight**	**Gantry rotation(°)**	**Coll rotation (°)**	**Couch rotation (°)**	**Beam X (cm)**	**Beam Y (cm)**	**SSD (cm)**	**MU**
Post[*]	Static	6X	1.084	195	0	0	14.8	15.4	87.8	97
Post.0	Static	6X	0.066	195	0	0	14.8	15.4	87.8	7
Post.1	Static	6X	0.076	195	0	0	14.8	15.4	87.8	7
OAD[*]	Static	6X	0.231	300	0	0	21.4	14.8	85	23
OAD.0	Static	6X	0.066	300	0	0	21.4	14.8	85	7
OAD.1	Static	6X	0.072	300	0	0	21.4	14.8	85	7
ANT[*]	Static	6X	0.976	15	0	0	14.3	14.1	88.4	84
ANT.0	Static	6X	0.079	15	0	0	14.3	14.1	88.4	7

[*] Post: posterior, OAD: Oblic Anterior Right, ANT: Anterior, SSD: source to surface distance, MU: Monitor Unit.

For the IMRT plan, new beams and dose constraints on the PTV and OARs were taken into account (Table (V.4). The IMRT dose-volume optimization objectives considered are presented in the Table (V.5).

Table V.4: Details of the considered radiotherapy IMRT improved treatment planning of lung lesion. PTV – planning target volume

Prescribed dose	40 Gy given within 20 fractions (2Gy/fraction)									
Constraint on dose	95% of the dose covers 95% of the PTV									
Number of Fields	3fields									
Beam ID	**MLC**	**Energy(MeV)**	**Field weight**	**Gantry rotation(°)**	**Coll rotation (°)**	**Couch rotation (°)**	**Beam X (cm)**	**Beam Y (cm)**	**SSD (cm)**	**MU**
POST	Dynamic	6X	1	195	0	0	16.1	15	87.8	364
OAD	Dynamic	6X	1	300	0	0	20.9	14.5	85	209
ANT	Dynamic	6X	1	5	0	0	14.4	14	88.7	275

*Post: posterior, OAD: Oblic Anterior Right, ANT: Anterior, SSD: source to surface distance, MU: Monitor Unit.

TableV.5: Dose-volume optimisation objectives

Organ and Structure	**Volume (%)**	**Dose (Gy)**	**Priority (P)**	**Resolution (mm)**
Heart	0	10 (max.)	200	3.0
PTV40	0	42 (max.)	200	
	9	39 (min.)		
	100	39.8 (min)		
Spinal cord	0	5 (max.)	400	
	30	5 (max.)	300	
Left lung	30	10 (max.)	200	
	20	20 (max.)	200	
Lungs without PTV	30	20 (max.)	200	
	20	30 (max.)	200	
PTV42	0	42 (max.)	200	1.72
Outside PTV	0	40 (max.)	300	4.5

V.2.2.2 Thermoluminescence dosimetry

In external radiotherapy, tissue equivalent thermoluminescence detectors (TLDs) such as TLD-700 can be used to check point doses delivered to a patient. In the present work, ThermoFisher SNO78835 TLD-700 chips of dimensions: 3.2 × 3.2 × 0.89 mm^3 were used. Before their use in clinical dosimetry application, the TLDs were completely characterized in terms of reproducibility of the TL signal, response as a function of depth, and response as a function of dose. Thus, the carefully selected TDLs have been subjected to a verification of their reproducibility by repeating their irradiation three times in same condition (after regeneration) with the same dose of 2 Gy [1]. Only TLDs with a standard deviation between TL intensities less than 3% were selected. In this work, the TL thermoluminescence signals were acquired under the same conditions presented in the Table (V.6).

Table V.6 : Conditions of the thermoluminescence signal reading

Luminescence reading mode	Thermoluminescence
Maximum reading temperature	300 °C
Heating rate	5 °C/s
TL signal sampling	250 points over the range 0 °C to 450°C
TLD annealing conditions	10 minutes at 400°C followed by 15 minutes at 100°C

V.2.2.3 TLDs calibration according to a reference TLD

To avoid fluctuations in TLDs response due to their own weights, reading positions, and irradiation history, correction factors have been determined and introduced to correct the TL intensity measured by each TLD. The calibration procedure is based on the exposure of all used TLDs (including the reference TLD) to the same photon beam and same dose of 2 Gy after regeneration. The regeneration was carried out by heating TLDs to 400 °C for 15 minutes, then to 300 °C for 10 minutes and by cooling them in open air. All the TLDs were, thus, exposed in the reference position inside the RW03 phantom. The reference exposure conditions are carried out at a depth Z of 10 cm with a photon beam of 10×10 cm^2 field size and in iso-centric SAD configuration (SAD = source-axis distance = 100 cm) (Figure V.6).

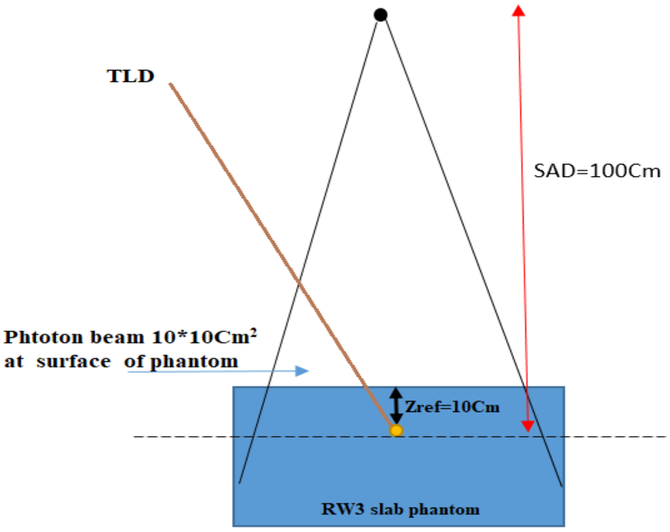

Figure V.6: Reference exposure conditions for TLDs calibration

The measured TL signals and therefore the determined intensities were corrected in accordance according to equation (V.1). Thus, four correction factors were considered for optimal accuracy of the measured TL intensity. These correction factors are given by the following equations: Eq.(V.2) - individual correction factor ***Ei*** for each TLD used (compared to the average), Eq.(V.3) - actual to reference TL measurement ratio ***R*** for a dose of 2 Gy, Eq (V.4) – TLD's weight correction factor ***Wi***, and Eq.(V.5) - Correction factor related to the reading position and calibration of the Riso OSL/TL reader DA-20 (48 positions in all) ***Pi***.

$$TL_{corr} = TL_{meas}.R.E_i.W_i.P_i \qquad (V.1)$$

$$E_i = \frac{TL_{mean}}{TL_i} \qquad (V.2)$$

$$R = \frac{TL_{act}(2Gy)}{TL_{ref}(2Gy)} \qquad (V.3)$$

$$W_i = \frac{m_i}{m_{mean}} \qquad (V.4)$$

$$P_i = \frac{TL(P_i)}{TL_{mean}(allpositions)} \qquad (V.5)$$

Where: TL_{corr} is the corrected TL intensity, TL_{meas} is the measured TL intensity (integral value), TL_{mean} is the mean TL intensity of all TLDs measured at 2 Gy dose, TL_i is the TL intensity of a given TLD measured at 2 Gy, TL_{act} is the measured TL intensity of the reference TLD for the actual experiment and a dose of 2 Gy, TL_{ref} is the measured TL intensity of the reference TLD for the first calibration experiment (reference) and a dose of 2 Gy, m_i is the TLD weight, m_{mean} is the average weight of all TLDs, $TL(P_i)$ is the measured TL intensity of the reference TLD at any given TL reading position in the reader for a dose of 2 Gy, TL_{mean}*(all positions)* is the mean TL intensities of the reference TLD for all TL reading positions of the reader and a dose of 2 Gy.

V.2.2.4 Verification of the in-depth response of TLDs

As is well known, the yield in depth (PDD) is a very important clinical data measurement on the used radiotherapy treatment beam necessary for dose calculation by the TPS. To check whether the TLDs used respond adequately in depth, some selected in-depth doses on the PDD measured by a standard ionization chamber used in clinical routine were measured by the reference TLD. Indeed, at the CLCC radiotherapy service, the PDD is generally checked in clinical routine using a calibrated Semiflex PTW 31010 (0.125 cc) ionization chamber and a water phantom (MP3). In our case, we used the reference TLD and the RW03 phantom to check these doses. Three doses were then checked at three depth positions: at the surface (Z = 0), at the electronic equilibrium position where the dose is maximum (Z = 1.5 cm), and at the reference depth of the TPS (Z =10 cm). For this verification, a standard field of 10x10 cm^2 with a source-surface distance (SSD) of 100 cm and photon energy of 6 MV were used.

V.2.2.5 Establishment of the TLDs response as a function of the dose

The curve of the TL response as a function of the dose of the TDLs was established by measuring the intensities of the TL signal corresponding to the following doses: 0.1, 0.5, 1, 1.5, 2 and 2.5 Gy. The TLDs were irradiated under TPS reference conditions using the solid water equivalent phantom RW03. The irradiation was carried out with the same treatment photon energy (6 MV). The TL signals were read immediately after exposure.

V2.2.6 Measurement of specific in-depth doses on Rando phantom by TLDs

Indirect TL dosimetry at different depths was performed using a Rando phantom instead the actual patient. To plan a Rando radiotherapy treatment, a virtual patient was created within the TPS with the real structures and the lung lesion of the real patient reproduced on Rando CT data. Based on the prescribed dose for the real patient, i.e. 40 Gy delivered in 20 fractions, an IMRT treatment planning and a dose calculation were performed for the virtual patient (Rando) using the AAA algorithm with the dose-volume optimization (DVO) algorithm of IMRT [2]. As part of this work, the calculated doses were verified by measuring the dose in 19 well-selected positions on the Rando phantom, using TLDs placed carefully in these previously selected positions on the CT-slices. The TLDs were, thus, distributed over three layers of the phantom corresponding to the following CT-slices: 6.3 cm, 9 cm and 12.3 cm (in terms of axial scanning position Z) (Figure V.7).

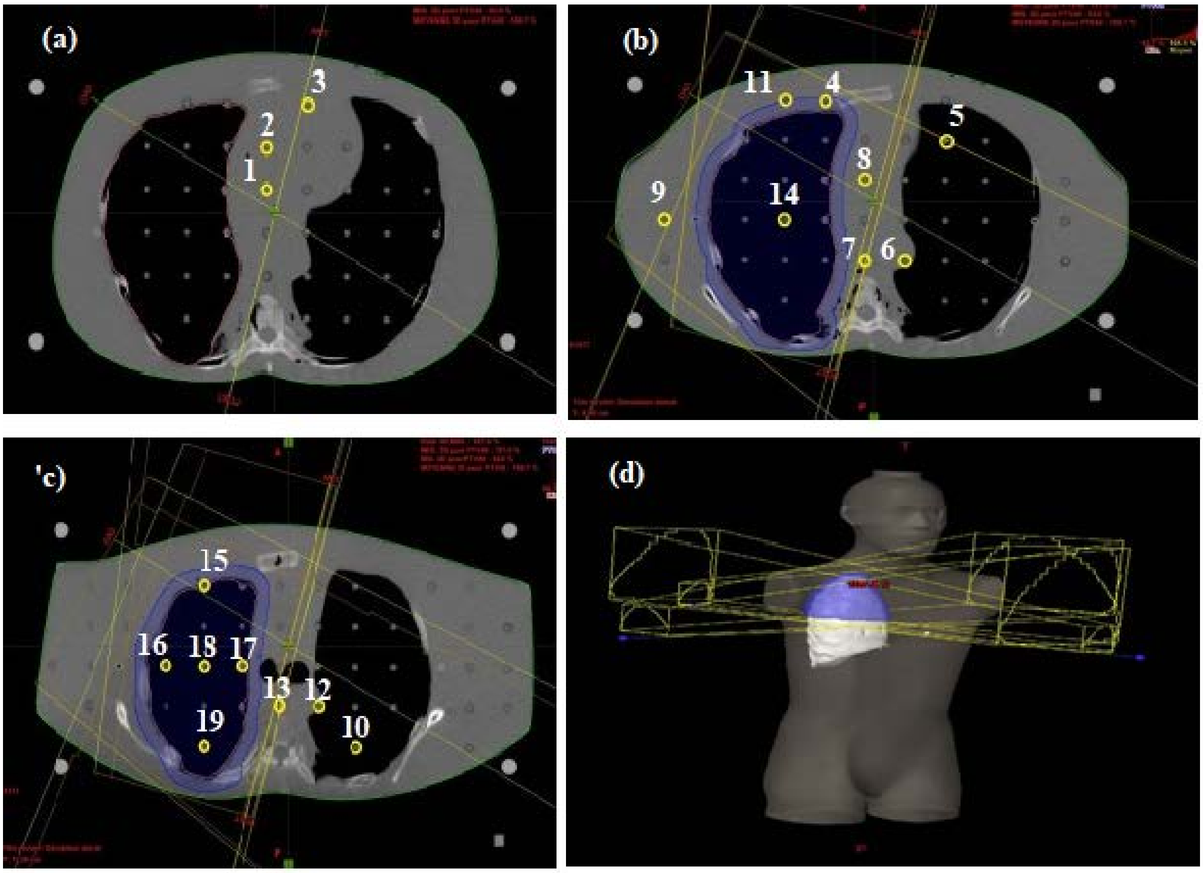

Figure V.7: TLD positions shown on CT-slices with radiotherapy beams angles for 3D-CRT: (a) slice with y=6.3cm, (b) slice with y=9cm, (c) slice with y=12.3 cm, (d) 3D fields viewing with PTV (in blue).

V.2.2.7 Dose calculation and heterogeneity correction

In this work, the dose calculation was carried out by the convolution and superposition anisotropic analytical algorithm (AAA) version 11.0.31 implemented within the Varian *Eclipse* TPS. The configuration of the AAA is based on the use of fundamental beam attenuation and energy deposition parameters and function (kernels) determined by Monte Carlo simulation. These parameters and kernels are generally adapted and checked with the measured clinical data of the beam. The AAA algorithm also uses Monte Carlo to simulate transport and energy deposition of primary photons, scattered and extra-focal photons and scattered electrons. The heterogeneity correction is carried out, in this case, on three levels: transversely (axially), laterally and at heterogeneous tissue interfaces namely, soft-tissue/lung and soft-tissue/bone interfaces. These corrections are based on equations (V.6), (V.7) and (V.8) [2]. In addition, AAA has a different approach to consider and to correct heterogeneity effect on dose compared to other algorithms which depends on the type of heterogeneity considered (air, bone ...), the tissue density and the tumor location [7-9].

$$I_\beta(Z,\rho) = I_\beta(\grave{Z}), with\ \grave{Z} = \int_0^Z \frac{\rho(t)}{\rho_{water}} dt(\tag{V.6}$$

$$K_\beta(x_\beta, y_\beta, z_\beta) = \frac{\rho(x,y,z)}{\rho_{water}} \sum_{k=0}^{5} c_k\ (\grave{z}) \frac{1}{r} e^{-\mu_k r_d(x,y,\rho)}, with r_d(x,y,\rho) = \int \frac{\rho(\vec{t})}{\rho_{water}} d\ \vec{t} \tag{V.7}$$

$$k_z(z) = \frac{\rho(z)}{\rho_{water}(z)} \sum_{i=1}^{2} c_i \frac{1}{\mu_i} e^{-\mu_i \grave{z}} \tag{V.8}$$

Where: $I_\beta(Z, \rho)$ is the energy deposition function taking into account heterogeneities, Z is the depth of the calculation point, Z is the radiological distance from the origin of the nucleus (diffusion centre), $\rho(t)$ is the mass density of the tissue, ρ is the water density, $K_\beta(x_\beta, y_\beta, z_\beta)$ is the diffusion nucleus (voxel) at the coordinates of the beam (x_β, y_β, z_β), c_k is the weighting factor of the nucleus allowing normalization of the total energy of the nucleus, μ_k is the attenuation constant, r_d is the radiological distance at Z depth which is the origin of the nucleus point at the point of coordinates (x, y, z) , $\vec{t}$ is the integral line of the nucleus origin $(0,0, z)$ to (x, y, z), kz is the one-dimensional diffusion nucleus (1D), c_i and μ_i are coefficients determined by Monte-Carlo simulation for the nucleus of each beam.

V.2.2.8 Dose-volume optimization in IMRT

In IMRT, the quality of the radiotherapy plans can be assessed using physical or biological criteria. With physical criteria, optimization in IMRT generates conformational dose distributions by modulating the field intensities iteratively until the dose-volume objectives considered in the treatment planning are fully satisfied. The objective function is the sum of the dose-volume objectives defined by the user. The mathematical formulation of the optimization problem is based on the combination of individual quality indicators on the target structures and the OARs on the base of dose constraints to produce a single measure which represents the quality of the complete treatment planning. This task is very complicated because the considered indicators for the targeted structures and the organs at risk are linked to interdependent and contradictory optimization objectives in terms of maximization and minimization of the delivered dose. Thus, the objective function for the target (T) and the OARs is simply presented by following elements according to weighted sum of the individual quality indicators [10,11].

$$F_{T_k} = \frac{1}{N_k}\left[\sum_{i=k}^{N_k}(D_i - D_{p_k})^2 + w_{min_k}\sum_{i=k}^{N_k}(D_i - D_{min_k})^2\mathcal{H}\left(D_{min_k} - D_i\right) + w_{max_k}\sum_{i=k}^{N_k}(D_i - D_{max_k})^2\,\mathcal{H}\left(D_i - D_{max_k}\right)\right] \qquad (V.9)$$

$$F_{OAR_k} = \frac{1}{N_k}\left[w_{max_k}\sum_{i=k}^{N_k}(D_i - D_{max_k})^2\,\mathcal{H}\left(D_i - D_{max_k}\right) + w_{dv_k}\sum_{i=k}^{N_{dv_k}}(D_i - D_{dv_k})^2\,\mathcal{H}\left(D_i - D_{dv_k}\right)\right] \qquad (V.10)$$

Where: N_k is the number of points in the target (T), and D_i is the dose to the i^{th} point in the target, Dp_k is the prescription dose, $Dmin_k$ and $Dmax_k$ are the minimum and maximum dose allowed, w_{mink} and w_{maxk} are weighting factors for each constraint on dose to be delivered to the target for under-dosage and over-dosage cases, $\mathcal{H}(x)$ is the Heaviside function, D_{dvk} and w_{dvk} are dose and weight parameters that define the dose–volume-histogram (DVH) constraints of an OAR [10,11].

Thus, the iterative process updated intensity (Ψ^*) and optimized dose (D^*) are given by:

$$\Psi^* = \arg min_I\left[\sum_j^{N_T} F_{T_j}(D(I),P) + \sum_j^{N_{OAR}} F_{OAR_k}(D(I),P)\right] \qquad (V.11)$$

$$D_i^{\,*} = \sum_{j=1}^{N} K_{ij} I_j^* \qquad \text{(V.12)}$$

Where: P is the set of dose limits and weights for all the optimization structures that defines the objective function and Kij is the dose coefficient (Kernel) corresponding to the j^{th} beamlet and the i^{th} voxel.

Within the Eclipse dose-volume optimization (DVO) the *Gradient* algorithm is used to optimize dose-volume for given set of parameters P initially selected. The selection of P parameters must satisfy the clinical criteria. Automatic methods of P parameter selection have been proposed [12,13]. Stochastic algorithms are also usually used for such parameters optimization [14-18]. Eclipse DVO uses automatic P parameters selection with *Simulated Recruit* method with an efficient speed. The iterative optimization stops when the objective function curve no longer varies, the maximum time limit has been reached, he maximum number of iterations has been reached, or dose uniformity in target volumes [19].

In this work DVO IMRT algorithm was used. This algorithm uses iterative method to detremine the optimal shape and intensity of the field and therfore and optimal solution that must conform the dose distribution to the defined user's objectives [20]. The Eclipse DVO version 11.0.31 is used in the framework of this study. DVO optimizes the field shape and intensity using simple determintisitic iterative global gradient optimization allowing to find the optimal solution [21]. On the Basis of clinical experience and by direct correlation between clinical observation and characteristic dose values, the dose constraints and the resolution of tissues of interest and OARs were predefined (Table (V.7)). In this work, the dose optimization algorithm performs the optimization as a minimization problem using simple gradient optimization. With the gradient optimization, the objective function is convex and therefore only a global minimum and no local minima exist [17]. In this algorithm a gradient evaluation generates first the gradient direction and length and then the objectives by a line search along the line segment in order to find the minimum. The mains steps of the DVO algorithm are as follows:

1. Optimization is performed field by field,

2. Calculation of an intermediate dose for the optimization of plan,

3. Calculation of the difference between the intermediate dose and the first optimization result,

4. The difference found is used to compensate the optimal result in the next iterations.

5. Calculation of new intermediate dose and its utilization to compensate next iteration if such case arises,

6. Iteration process is stopped when the predefined objectives are reached with minimum errors in respect to the DVHs produced during iteration.

DVO optimization is generally influenced by the tissue heterogeneity existence and subjected to optimization convergence error [22-25]. In the DVO optimization dose calculation errors are particularly present in electronic disequilibrium region near the heterogeneity interfaces as it is the case in our study. Finally, it is important to mention that medical physicist with the assistance of the clinician has to assign correct and optima priorities values to the optimization objectives of PTV structures and OAR objectives. During the iteration procss OAR objectives are gradually pushed to lower dose values at each iteration without significantly affecting the DVH of the PTV. PTV/OAR optimization priorities are adjusted to meet user-specific criteria for PTV dose coverage and homogeneity [26].

V.2.2.9 Dose covering assessment

To compare dose covering between 3D-CRT and IMRT, the programmed target volume coverage was evaluated using the heterogeneity index (HI), the uniformity index (UI) and the conformity index (CI) defined as follows [27]:

$$HI = \frac{D_{2\%} - D_{98\%}}{D_{50\%}}, \qquad (V.13)$$

where, $D_{2\%}$ is the dose of 2% of the programmed target volume, $D_{98\%}$ is the dose of 98% of the programmed target volume, and $D_{50\%}$ is the dose of 50% of the target volume [27];

$$UI = \frac{D_{5\%}}{D_{95\%}}, \qquad (V.14)$$

where, $D_{5\%}$ is the dose of 5% of the programmed target volume, and $D_{95\%}$ is the dose of 95% of the programmed target volume [28,29];

$$CI = \frac{PTV_{95\%}}{PTV}, \qquad (V.15)$$

where, *PTV* is the programmed target volume and $PTV_{95\%}$ is the volume covered by 95% of the prescribed dose.

V.3 Results and discussion

V.3.1 Reproducibility and selection of TLDs

After having been properly regenerated and in order to check their reproducibility, the TLDs were irradiated three times in succession with a dose of 2 Gy delivered by an X-ray generator (50 kV, 1 mA). The standard deviation σ calculation (in percentage) is used to assess reproducibility (Table V.7).

$$\sigma(\%) = \frac{\sigma}{TL_{mean}} . 100 \qquad (V.16)$$

With, σ: standard deviation and *TLmean*: average *TL* value of the three values measured for each TLD.

Table V.7: Standard devivation results of used TLDs

TLD N°	TL max	Standard deviation (σ)	Standard deviation σ in %
1	1227	2.49	0.20
	1225		
	1231		
2	789	1.67	0.21
	793		
	790		
3	827	2.16	0.26
	826		
	831		
4	1077	5.44	0.5
	1090		
	1081		
5	1076	7.48	0.69
	1082		
	1094		
6	1124	12.19	1.07
	1147		
	1152		
7	1225	14.16	1.15
	1248		
	1214		
8	1061	12.36	1.16
	1085		
	1057		
9	1060	17.44	1.63
	1060		
	1097		

10	1026	17.44	1.68
	1063		
	1092		
11	619	10.62	1.68
	633		
	645		
12	1149	21.27	1.8
	1192		
	1196		
13	1111	20.24	1.87
	1080		
	1062		
14	1307	27.21	2.03
	1348		
	1373		
15	1152	23.25	2.07
	1096		
	1115		
16	1002	24.25	2.34
	1059		
	1045		
17	1139	31.97	2.82
	1094		
	1172		
18	1121	55.37	1.53
	1156		
	-		
19	1154	77.467	0.51
	1166		
	-		

TLDs with standard deviation (%) greater than 3% were rejected and excluded from use in this work.

V.3.2 Characterization and calibration of TLDs

In this characterization step of measurement in real conditions, the selected TLDs were placed on the RW03phantom and exposed to a dose of 2 Gy of a 6MV photon beam delivered by the linear accelerator under reference conditions and with a SAD configuration. The correction factors of the TL signal with the same beam used in treatment are, thus, determined. The obtained values are indicated in the Table (V.8) for each TLD.

Table V.8: Determined correction factors of TLDs

TLD N°	Weight (mg)	*Wi*	*Pi*	*Ei*
1	23.8	0.98604	0.65173	0.93933
2	24.3	1.00676	0.55047	0.93995
3	24.3	1.00676	0.77869	0.87079
4	23.4	0.96947	0.67018	0.96374
5	24.3	1.00676	0.89727	0.9095
6	24.4	1.0109	0.84006	0.9597
7	24.2	1.00262	0.62506	0.84678
8	24.1	0.99847	1.11205	1.12235
9	23.9	0.99019	0.76485	0.90045
10	23.9	0.99019	1.25362	0.72552
11	24.5	1.01505	1.00082	1.08129
12	24.4	1.0109	0.64525	0.78995
13	24.4	1.0109	0.72134	0.93118
14	24.1	0.99847	1.03908	0.99817
15	24.3	1.00676	0.99197	0.99001
16	23.0	0.9529	1.23332	1.47829
17	24.4	1.0109	0.98124	1.05702
18ref	24.7	1.02333	0.93097	1.57761
19	24.2	1.00262	0.94477	0.91836

V.3.3 Establishment of the TL-Dose response curve of TLDs

For the establishment of the response function (abacus curve) expressing the variation of the intensity of the TL signal as a function of the dose, the reference TLD was exposed to several doses under the reference conditions. The TL signals obtained are shown in Figure (V.8).

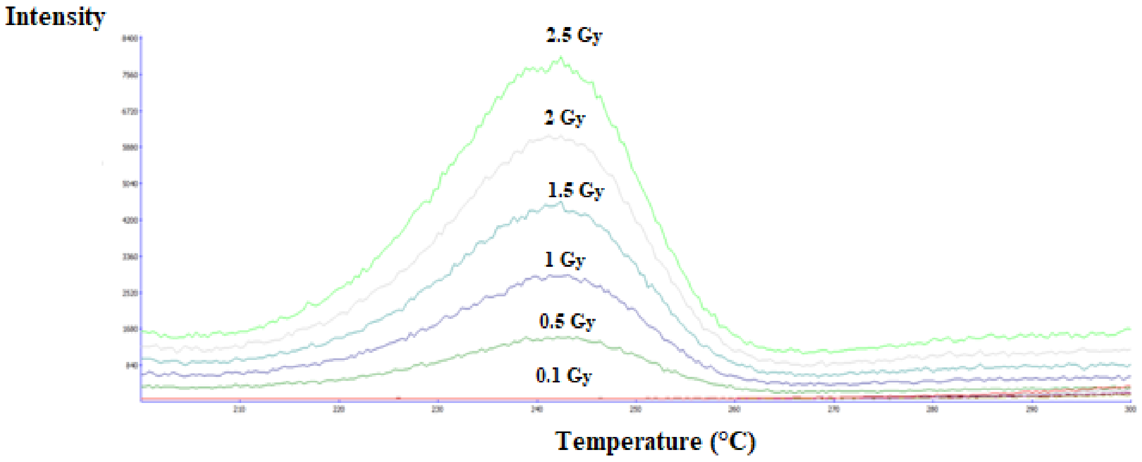

Figure V.8: TL signals from the reference TLD EXPOSED for several doses.

From these latter results, the response curve (TL = f (D)) of the TLDs was established by measuring the integral intensities of the TL signal corresponding to the doses considered: 0.1, 0.5, 1, 1.5, 2, and 2.5 Gy. The intensities TL are indicated in the Table (V.9).

Table V.9: TL intensities corresponding to the different doses

TLD N°	Dose (Gy)	Corresponding MU* number	TL Integral
6	0.1	13	8363
8	0.5	63	31865
11	1	125	73700
16	1.5	188	92977
18	2	251	143650
17	2.5	313	167152

*MU : monitor unit.

The results from Table (V.9) are plotted on the graph of Figure (V.9). It can be easily verified that the response of TLDs is linear along the dose interval considered. The linear fitting of the experimental data allowed the determination of an experimental relationship (Eq (V.17)) which was used for the accurate determination of the dose in Gray (Gy) for any measured TL intensity.

$$\boldsymbol{TL} = (64500 \pm 1300) * \boldsymbol{D} + (1800 \pm 380) \qquad \text{(V.17)}$$

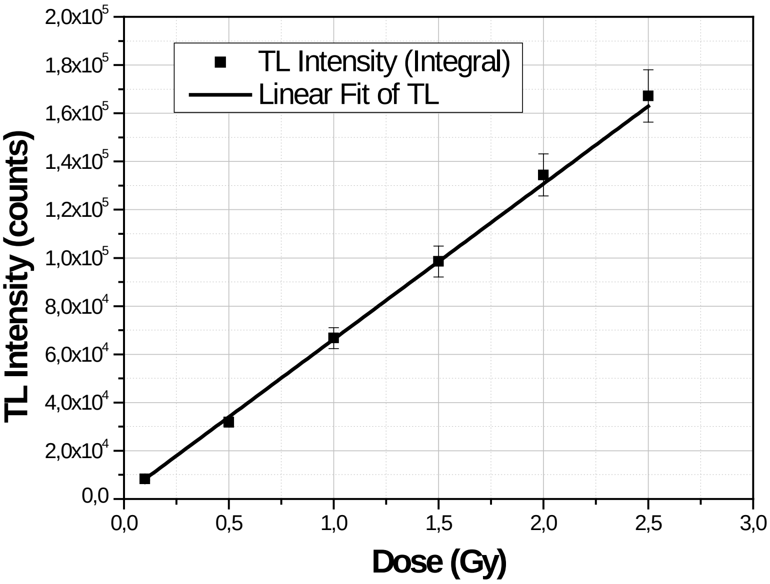

Figure V.9: TL-Dose response curve.

V.3.4 TLDs in water depth dose response checking (PDD)

To verify the conformity of the depth dose response of the used TLDs, these TLDs were exposed to a dose of 2 Gy (X6MV) at three depth distances of interest (Z = 0 cm, 1.5 cm, and 10 cm) using the RW03 phantom. The TL signals obtained after exposure at these considered three depths are presented in Figure (V.10).

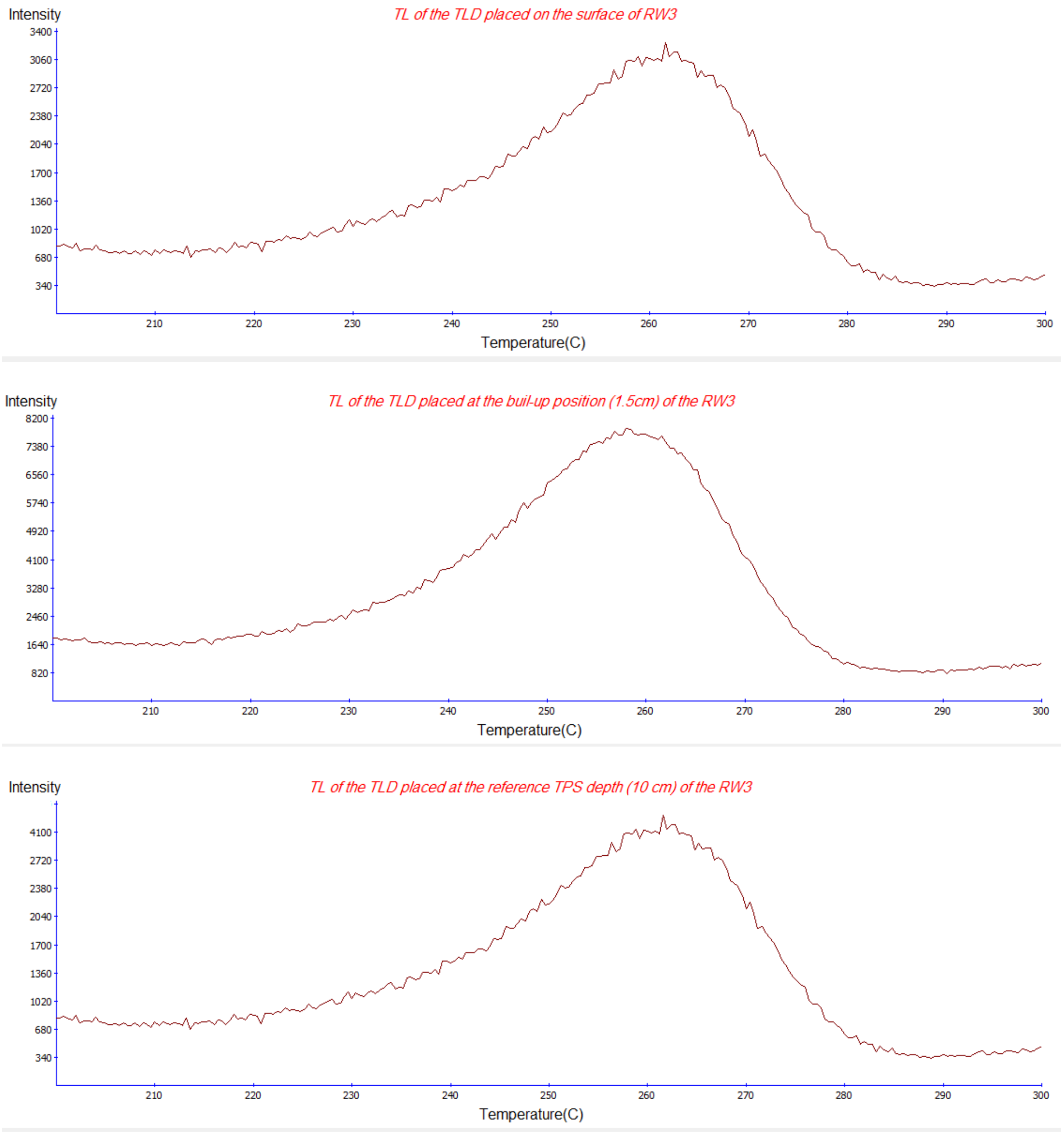
TL of the TLD placed on the surface of RW3

TL of the TLD placed at the buil-up position (1.5cm) of the RW3

TL of the TLD placed at the reference TPS depth (10 cm) of the RW3

Figure V.10: TL signals obtained for PDD verification.

The exposure conditions and the doses obtained after reading the TLDs are presented in Table (V.10). The comparison between the PDD established by the calibrated ionization chamber commonly used in clinical radiotherapy practice and the in-depth dose measured by the TLDs shows that the latter are capable to produce accurate and compliant PDD (Figure V.11). The TLDs used are therefore suitable for very accurate in-depth dose measurement.

Table V.10: Results of in-depth doses measured by TLDs (reduced PPD)

TLD N°	MU	Depth distance	Dose (Gy)	% of the max value (%)
18	949	Z=0 cm surface	2.05	52.66
18	949	Z max=1.5cm	4	100
18	949	Z=10 cm (référence)	2.5	67.37

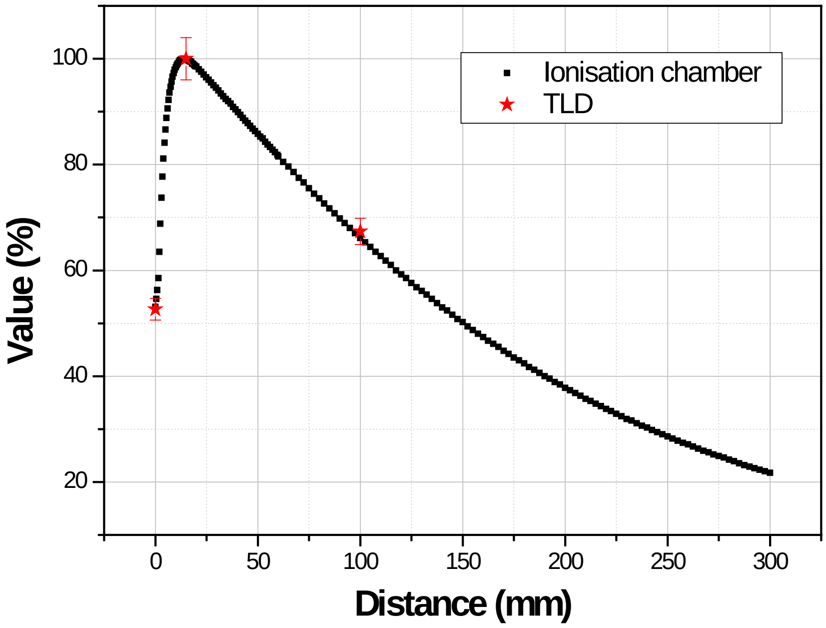

Figure V.11: PDD of the central axis established by the ionization chamber in the water phantom (MP3) and PDD reduced established by the TLDs in the RW03phantom for a photon beam of 6 MV, a field size of 10 ×10 cm^2. The measured doses are normalized to the maximum dose measured at the depth (Zmax) of 1.5 cm.

V.3.5 Comparison between calculated and measured doses

In the present work, ThermoFisher SNO78835 TLD-700 chips (3.2 x 3.2 x 0.89 mm3) were used as dosimeters. TL signals were read with the Risø TL/OSL-DA-20 luminescence reader [5-6]. The thermoluminescence signals were all collected under the same experimental conditions presented in the Table (V.6). The same 19 dose measurement positions on Rando phantoms already used in case of 3D-CRT [1] were used for IMRT (Figure V.7). The beams and fields listed in Table (V.4) were used to deliver the prescribed dose to RANDO phantom according to the considered IMRT treatment planning. Thus, the comparison between measured and calculated dose was made on the basis of the comparison between point-doses at the different considered positions on the Rando phantom. Furthermore, comparisons between 3D-CRT and IMRT calculated doses were made in terms of three aspects: 1-horizontal and vertical dose profiles passing through heterogeneous media (spinal cord and right lung) as shown in Figure (V.12), 2-through the dose-volume histograms of the PTV and OARs (HDV), and 3-on the basis of the calculated dose coverage indices.

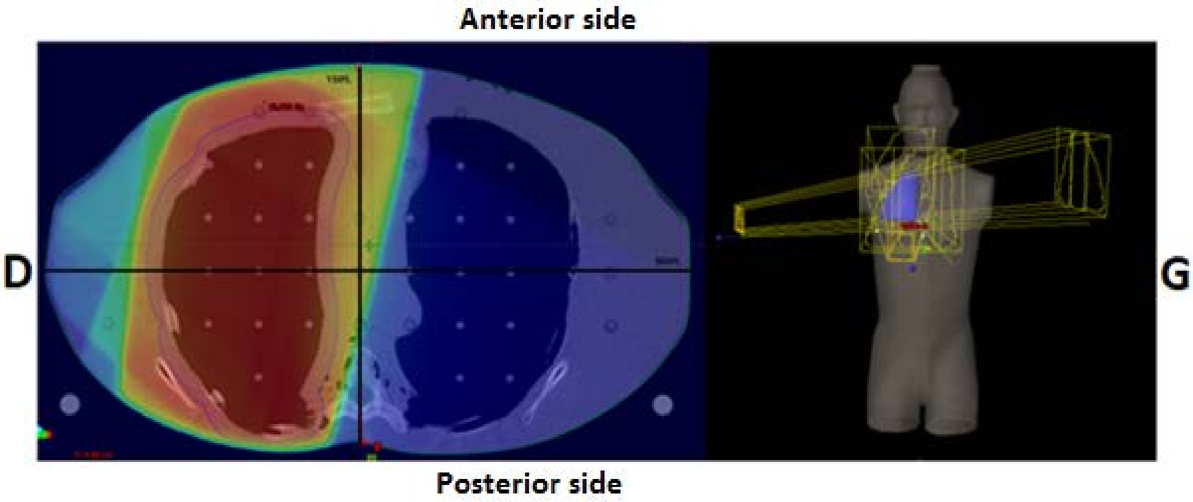

Figure V.12: Scanning lines selected on the CT-slice y = 9 cm used the vertical and horizontal dose profiles plotting (solid black lines on the left), and 3D image of the Rando phantom with the indication of the beams used in IMRT (on the right).

V.3.5.1 Comparison between calculated and measured point-doses

After establishing of the the TLDs TL-Dose response of the determination all correction factors, the doses were measured at the 19 positions selected position on the Rando phantom and compared to the doses calculated by the TPS (Table V. 11) for IMRT. Those of 3D-CRT are taken from reference [1]. The difference between calculated and measured doses for the two radiotherapy techniques IMRT and 3D-CRT is evaluated by calculating the value of the absolute difference Δ in percentage as indicated in Table (V.11).

Table V.11: Different AAA-calculated (AAA: anisotropic analytical algorithm) doses for 3D-CRT and IMRT and TL-measured (TL: thermoluminescence) doses and differences Δ between calculated and measured for 3D-CRT and IMRT; see Figure 1 for location of TLDs

TLD Position	**3D-CRT [1]**		**IMRT**		**Dose Comparison** $\Delta(\%) = \left\lvert \frac{D_{TL} - D_{cal}}{D_{TL}} * 100 \right\rvert$	
	Calculated Dose (Gy)	**Measured Dose** (Gy)	**Calculated Dose** (Gy)	**Measured Dose** (Gy)	**Δ(%) 3D-CRT**	**Δ(%) IMRT**
1	0.087	0.094±0.004	0,043	0.046±0.002	7.45	6.52
2	0.25	0.27±0.01	0,11	0.10±0.01	7.41	10
3	0.21	0.23±0.01	0,11	0.12±0.01	8.69	8.33
4	2.11	2.08±0.10	1,97	2.05±0.10	1.44	3.90
5	0.17	0.18±0.015	0,049	0.053±0.002	5.55	7.54
6	0.28	0.32±0.02	0,19	0.20±0.02	12.5	5
7	1.05	1.04±0.05	0,52	0.55±0.03	0.96	5.45
8	1.71	1.70±0.08	1,08	1.00±0.05	0.59	8
9	0.54	0.52±0.06	0,28	0.26±0.02	3.85	7.7
10	0.27	0.29±0.01	0,17	0.19±0.02	6.90	10.52
11	2.13	2.17±0.10	2.00	2.05±0.10	1.84	2.44
12	0.21	0.24±0.01	0,23	0.24±0.01	12.5	4.16
13	0.51	0.51±0.02	0,38	0.40±0.02	0	5
14	2.09	2.08±0.10	2,09	2.05±0.10	0.48	1.95
15	2.10	2.23±0.10	1,98	2.08±0.10	5.83	4.80
16	2.03	2.04±0.10	1,98	2.05±0.10	0.49	3.41
17	2.01	2.00±0.10	2,05	1.98±0.10	0.5	3.53
18	2.07	2.09±0.10	2,07	2.05±0.10	0.96	0.97
19	2.09	2.13±0.10	2,07	2.10±0.10	1.88	1.43

From the results in Table (V.11) we see that for the low doses the differences (Δ) between the measured and calculated doses are greater than those of the highest doses. Indeed, the average difference Δ between the calculated and measured doses for low doses (<0.55Gy) is around 6.5% for 3D-CRT and around 7% for IMRT; whereas it is around 1.0% for 3D-CRT and 3% for IMRT in the case of the highest doses (> 0.55 Gy). It is also noticed that the maximum total dose measured by the TLDs for the heart is reduced to 2 Gy in case IMRT instead of 5.4 Gy in 3D-CRT (Position 2). This new value is much lower than the dose constraint on this OAR considered in the IMRT radiotherapy planning in the current work (see Table (V.5)). It has also been observed that the doses measured for PTV for the two radiotherapy techniques comply with ICRU recommendations with a notable advantage for IMRT. In IMRT, all doses calculated and measured in the PTV (Table V.12) were found to be within 95%-107% (1.9-2.14Gy) interval of the prescribed dose (2 Gy). These results and observations confirm that the optimal dose administration to the PTV, as targeted with the IMRT treatment planning validated during the calculation phase by the TPS, is experimentally verified by thermoluminescence dosimetry. The same statement is not valid for 3D-CRT because some large differences have been observed between calculated and measured doses at certain positions (positions 11 and 15).

Table V.12: Percentage (%) of the calculated doses and TL-measured doses with respect to the prescribed dose (2Gy) for 3D conformal planning (3D-CRT) and IMRT optimized planning (IMRT). PTV – planning treatment volume; HU – Hounsfield unit; TLD – thermoluminescence dosimeter; GTV- Gross tumor volume.

TLD location	**HU_{av} (Location)**	**% of the calculated / TL doses to prescribed dose 3D-CRT**	**% of the calculated / TL doses to prescribed dose IMRT**
1	17.75(Heart)	4.4/4.7	2.15/2.4
2	19.75(Heart)	12.5/13.5	5.5/5.0
3	13.25(Heart)	10.5/11.5	5.5/6.0
4	25.75 (Soft tissue, GTV)	105.5/104.0	98.5/102.5
5	-669(Left Lung)	8.5/9.0	2.5/2.75
6	10.5/-650* (Interface)	14.0/16.0	9.5/10.0
7	12.75(Soft tissue)	52.5/52.0	26.0/28
8	13.75(Soft tissue)	85.5/85.0	54.0/50.0
9	12.5(Soft tissue)	27.0/26.0	14.0/12.5
10	-476.25(Left Lung)	13.5/14.5	8.5/9.5
11	12(Soft tissue, GTV)	106.5/108.5	100/102.5
12	20/-433.5*(Interface)	10.5/12.0	11.5/12.5
13	22.5(Soft Tissue)	25.5/25.5	19.0/20.0
14	-469(PTV)	104.5/104.0	104.5/102.5
15	8/-705.75*(Interface)	105.5/111.5	99.0/104.0

16	-439.25(PTV)	101.5/102.0	99.0/102.5
17	-404(PTV)	100.5/100.0	102.5/99.0
18	-434.25(PTV)	103.5/104.5	103.5/102.5
19	-339.5(PTV)	104.5/106.5	103.5/105

*HUs of soft tissue/lung interface.

V.3.5.2 DVO dose optimization in IMRT and heterogeneity correction

Tissue heterogeneity is a serious problem in the radiotherapy treatment planning which must be effectively taken into consideration for the optimization of the dose to be delivered to the patient according to predefined constraints. In the framework of this thesis project, the dose distributions calculated by considering a real case of lung cancer heterogeneities were compared for radiotherapy treatments using two techniques, namely the IRMT and the 3D-CRT. The treatment planning of these two techniques have already been described. The comparison was made on the basis of:

1. Horizontal and vertical dose profiles passing through heterogeneous media (lung and spinal cord)
2. Dose-volume histograms (DVHs)
3. Dose coverage indices

The comparison between the vertical dose profiles passing through the spinal cord and the horizontal dose profiles passing through the right lung are shown in Figures (V.13) and (V.14). The scan lines used for these dose profiles are shown in Figure (V.12). The data scanning were performed from right (D) to left (G) for the horizontal profile and from the posterior side to the anterior side for the vertical profile. Analysis of the dose profiles obtained shows that the spinal cord (OAR) receives in IMRT a dose 32.5% lower than that received by the same organ in 3D-CRT. We also note that the dose profile just after the interface (tissue-soft/bone) towards the anterior direction increases considerably in 3D-CRT when compared to IMRT. This means more dose deposition in 3D-CRT between the two lungs outside the PTV (Figure V.13). The horizontal dose profiles show that IMRT spares well the left lung and all the other surrounding tissues of the right diseased lung. The dose profiles in the region of the diseased right lung are almost similar for the two techniques IMRT and 3D-CRT; which demonstrates the same dose coverage of the PTV (Figure V.14).

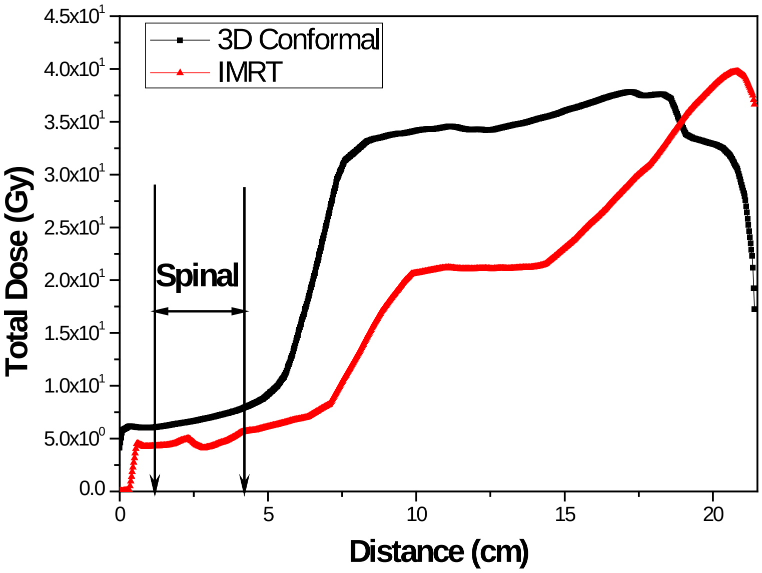

Figure V.13: Vertical dose profile line (VDPL) showing calculated dose variation through the heterogeneous spinal cord medium for IMRT and 3D-CRT.

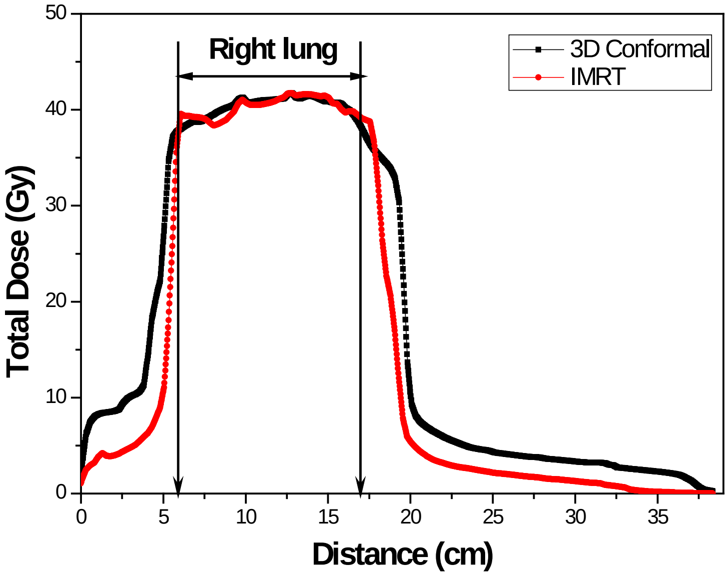

Figure V.14: Horizontal dose profile line (HDPL) showing calculated dose variation through the heterogeneous right and left lungs media for IMRT and 3D-CRT.

To deepen our comparison, the main dose-volume histograms (HDVs) were plotted and analyzed for IMRT and 3D-CRT (Figures V.15 and V.16). Indeed, the objective analysis of the HDVs obtained shows that the main constraints on the administration of the dose are generally respected in the two radiotherapy techniques. Furthermore, the comparison between the HDVs of the two techniques demonstrates that IMRT provides better dose coverage of the PTV than 3D-CRT. A reduction in the exposure of the OARs, namely: the left lung, the spinal cord and the heart, was also noted for IMRT compared to 3D-CRT.

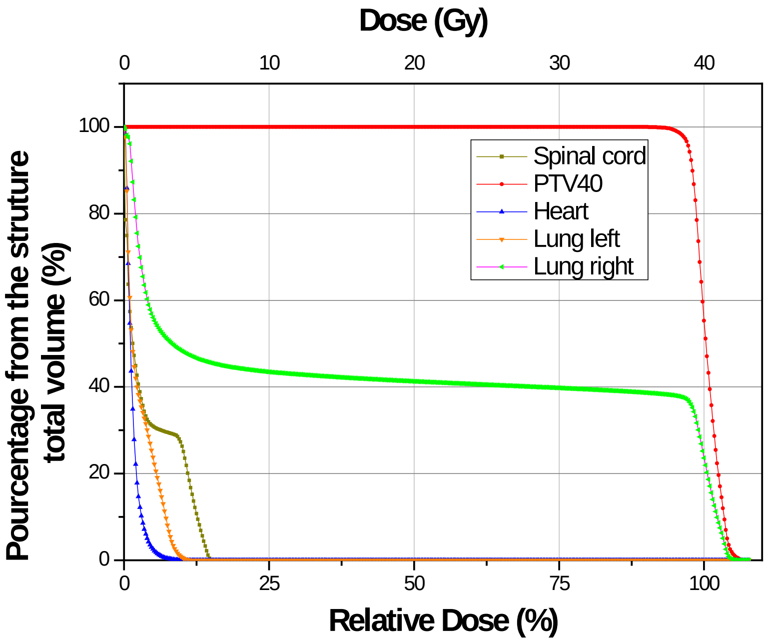

Figure V.15: Dose-volume histograms (DVHs) calculated for the most important organs and volumes for the considered IMRT treatment planning.

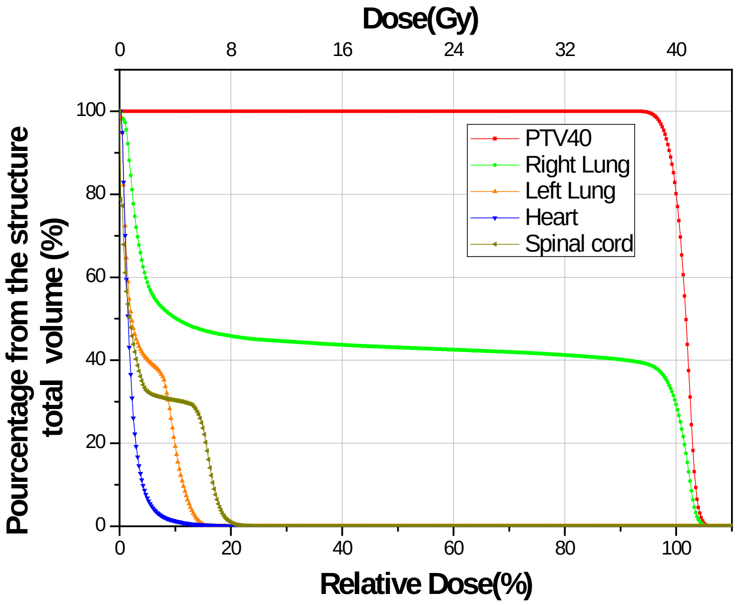

Figure V.16: Dose-volume histograms (DVHs) calculated for the most important organs and volumes for the 3D-CRT treatment planning.

HDVs show that the problem of the presence of heterogeneities is effectively corrected in IMRT by its dose-volume optimizer DVO. The treatment of heterogeneities in IMRT by its DVO is better than in 3D-CRT because by AAA algorithm and its proper methods of heterogeneity correction. In fact, the doses were reduced in IMRT when compared to 3D-CRT by 25.3%, 28.3% and 41.55% for the spinal cord, the heart and the left lung respectively. In terms of dose coverage of the PTV, the comparison shows an insignificant difference (0.92%) between IMRT and 3D-CRT. This proves that the two techniques manage to deposit the prescribed dose to the PTV with the same efficiency.

Finally, the dose coverage indices calculated and presented in the Table (V.13) confirm all the results obtained by the HDVs analysis.

Table V.13: Dose covering evaluation

Index	3D-CRT	IMRT	Acceptance Criterion
Conformity index CI	0.95	0.99	The closer value to one (1) is the best
Heterogeneity index HI	0.112	0.085	The closest value to zero (0) is the best
Uniformity index UI	1.099	1.07	The closer value to one (1) is the best

V.3.6 Discussion

Through the analysis of the results presented above, it is clear that IMRT considerably improves the treatment plans depending in terms of optimal dosimetric coverage and radio-toxicity reduction. In terms of local optimization of the dose, the measured in-depth pont-doses show a clear optimization of the dose in IMRT compared to 3D-CRT. In fact, the experimental results demonstrate that the local dose in the heart is reduced by more than 50% in IMRT compared to the reduced dose by 3D-CRT. The dose level near the spinal cord is also reduced by about 20% in IMRT always by comparison the reduced dose by 3D-CRT. In addition, the doses measured on the PTV are within ±5% of the prescribed dose for all measurement positions. The overestimates and underestimates of the doses calculated in IMRT and in 3D-CRT compared to the measured doses by TL dosimetry are all within acceptable tolerance ranges from a point of view of the compliance of the treatment plans with the constraints dose. Relatively large deviations were observed in 3D-CRT on the measurement points (positions): 11 with + 6.5%, and 15 with + 5.5%.

All the calculated DVHs and dose coverage indices are favorable for the application of IMRT instead of 3D-CRT, especially in the case of radiotherapy treatment exhibiting wide heterogeneities. Close collaboration between the radiotherapist and the medical physicist is more than necessary to achieve the predefined objectives for IMRT dose delivery. As IMRT is based on computerized reverse planning, OARs must be precisely delineated in order to avoid depositing excessive doses in these organs. Since the implementation of IMRT to date (January 2020), 126 patients have been treated for head-neck cancers and 21 for brain cancers at the cancer fighting centre of Sétif (CLCC-Sétif). For the treatment of lung cancer by IMRT, It is recommended that the radiotherapy service of CLCC-Sétif starts implementing techniques that avoid effect of respiratory movement on radiotherapy treatment. This can be done by using an assisting system for respiration retention or a respiratory triggering system (GATING) which controls the operation of the accelerator and the dose delivery according to the respiratory rate of the patient. Indeed, it has been clearly demonstrated through the current project that IMRT, compared to 3D-CRT currently used, effectively contributes to the treatment of lung cancer in terms of dose conformity and OARs exposure reduction.

Finally, it should be mentioned that in recent years IMRT with its DVO dose optimization algorithm has been intensively studied for the treatment of lung and other complicated cancers. Chen MJ. et al. report in an orientation and guidance study for the treatment of lung cancer by radiotherapy that IMRT can improves the physical and biological conformability of the dose with the possibility of releasing higher doses to target sub-volumes such as hypoxic without needing to increase the number of fractions and by maintaining low dose exposure of the healthy tissues [27]. These researchers also confirm that IMRT may be more appropriate than 3D-CRT for patients with large tumor volumes in difficult and sensitive locations in the thoracic anatomy [27]. In this same work, a retrospective study on 223 patients showed that the rate of patients with severe esophagitis requiring a feeding tube was 5% with IMRT versus 17% with 3D-CRT (p= 0.005). Another retrospective study conducted from multi-institutional databases also assessed the role of radiotherapy techniques on patient survival, demonstrating the superiority of IMRT over 3D-CRT. In fact, this study shows that 14% of patients treated with IMRT survived for 5 years after treatment with 11% for 3D-CRT (p = 0.0001) [27-30]. It has also been observed by Chan et al. [31] that according to numerous studies [32-38], IMRT reduces the volume of the whole lung receiving more than 20 Gy (V20). These studies also show that the effect of IMRT on low lung doses is not well understood. Indeed, some studies show a reduction in V5 [33,37], while other studies show an increase [35, 36,39]. Chen et al. report in their study that for exposure of the heart and spinal cord, the majority of studies have demonstrated an advantage with IMRT [35,36,38-41]. Boyle et al. demonstrate that IMRT decreased incidental dose to the lungs, heart, and esophagus with equivalent coverage of the planning target volumes as in 3D-CRT. They also claim that IMRT can, therefore, improve treatment tolerance [42]. In another more recent study, IMRT was associated with a significantly better overall survival (OS) of five years compared to 3D-CRT [43]. This study reports that with multivariate analysis of all the studied patients, IMRT has a good predictive factor for OS when compared with 3D-CRT. This last study showed that IMRT was significantly superior in terms of OS for advanced primary tumors. For different cases of lung cancer, C. Fiandra et al. demonstrate in their study that the IMRT technique allowed good coverage of the target volume by sparing the OARs with, as a consequence, larger volumes of healthy tissue receiving low doses and this for the case of Hodgkin lymphoma cancer at an early stage [44].

V.3.7 Conclusions

In this work, it has been shown that IMRT, compared to 3D-CRT, provides good protection for normal and at risk organs with a very accurate radiotherapy treatment planning, thanks to its dose optimization algorithm, DVO. Indeed, after the implementation of IMRT, the actual work demonstrates that technique improved the dose coverage of the target volume surrounded by heterogeneous media as it is the case of the considered lung cancer. In fact, it has been observed that IMRT effectively reduces radio-toxicity in the treatment of lung cancer. This dose reduction avoids certainly the observation of side effects just by the better protection of the healthy lung, the esophagus, the heart, and the spinal marrow. For the considered radiotherapy treatment of lung cancer with 3D-CRT, it has also been observed that AAA tends to underestimate the dose in the lung and to overestimate it in the adjacent tissues. With IMRT, the results of this thesis project clearly demonstrate that this technique is able to deliver the prescribed dose safely, with high precision, and with less radio-toxicity. At cancer fighting centre of Sétif, IMRT is now used for patients whose cases to be treated are unfavorable to the application of 3D-CRT and for patients who are judged to have a low chance of survival after radiotherapy treatment. On the basis of this work results, it is recommended that the application of IMRT be extended to the treatment of lung cancer after the installation of necessary techniques for respiratory movement reduction or automatic triggering of dose delivery according to the patient's breathing rate (Gating).

References

[1] Bouacid SS, Kharfi F, Boulakhssaim F. Comparison of measured and calculated doses in a Rando phantom with a realistic lung radiotherapy treatment plan including heterogeneities, Radiat Environ Biophys. 2018 Sep 11; 57:365–373.

[2] Varian medical system: Eclipse Algorithms Reference Guide. 2009 Aug; P/N B502612R03A, Palto Alto.

[3] Landberg T, Chavaudra J, Dobbs J, Gerard JP, Hanks G, Horiot JG, Johansson KA, Möller T, Purdy J, Suntharalingam N, Svensson H. Report 62: Prescribing, Recording and Reporting Photon Beam Therapy (Supplement to ICRU report 50). Journal of the ICRU. 1999 Nov 1; 32 (1).

[4] Landberg T, Chavaudra J, Dobbs J, Hanks G, Johansson KA. Report 50: Prescribing, Recording and Reporting Photon Beam Therapy. Journal of the ICRU. 1993 Sept 1; 26 (1).

[5] Kharfi F, Ketfi R. Irradiated black pepper identification based on thermoluminescence of silicate minerals. J Radioanal Nucl Chem. 2018 Jan 11; 315:503–507.

[6] Guide to the Risø TL/OSL Reader. 2015 Aug; DTU Nutech. Denmark. Available from: https://www.usu.edu/geo/luminlab/Reader.pdf.

[7] Carrasco P, Jornet N, Duch MA, Weber L, Ginjaume M, Eudaldo T, Jurado D, Ruiz A, Ribas M (2004), *Comparison of dose calculation algorithms in phantoms with lung equivalent heterogeneities under conditions of lateral electronic disequilibrium*, Med Phys31:2, 899–911.

[8] Rana SB (2013), *Dose prediction accuracy of anisotropic analytical algorithm and pencil beam convolution algorithm beyond high density heterogeneity interface*, South Asian J Cancer 2(1), 26–30.

[9] Van Esch A, Tillikainen L, Pyykkonen J, Tenhunen M, Helminen H, Siljamäki S, Alakuijala J, Paiusco M, Lori M, Huyskens DP (2006), *Testing of the analytical anisotropic algorithm for photon dose calculation*, Med Phys.33(11), 4130–4148.

[10] Oelfke U, Nill S, Wilkens JJ. Physical Optimization. In: Bortfeld T, Schmidt-Ullrich R, De Neve W, Wazer DE, editors. Image-Guided IMRT. Berlin Springer Heidelberg; 2006.

[11] Lu R, Richard, Radke RJ, Yang J, Happersett L, Yorke E, Jackson A. Reduced-order constrained optimization in IMRT planning. Phys Med Biol. 2008 Nov 7; 53(23): 6749–6766.

[12] Xing L, Li J, Donaldson S, Le Q, Boyer A. Optimization of importance factors in inverse planning. Phys Med Biol. 1999 Oct; 44(10):2525-36.

[13] Lu R, Radke R, Happersett L, Yang J, Chui C, Yorke E, Jackson A. Reduced-order parameter optimization for simplifying prostate IMRT planning. Phys. Med. Biol. 2007 Jan 17; 52:849–70.

[14] Webb S. Optimisation of conformal radiotherapy dose distributions by simulated annealing. Phys Med Biol. 1989 Oct; 34(10):1349-70.

[15] Morrill S. M., Lane R. G., Jacobson G, Rosen II. Treatment planning optimization using constrained simulated annealing. Phys Med Biol. 1991 Oct; 36(10):1341-61.

[16] Webb S. Optimization by simulated annealing ofthree-dimensional, conformai treatment planning for radiation fields defined by a multileaf collimator: II. Inclusion of two-dimensional modulation of the x-ray intensity. Phys Med Biol. 1992 Sep; 37 (8):1689-704.

[17] Bortfeld T. Optimized planning using physical objectives and constraints. Semin Radiat Oncol. 1999 Jan; 9(1):20-34.

[18] IMRTCWG. Intensity-modulated radiotherapy: current status and issues of interest. Int J Radiat Oncol Biol Phys. 2001 Nov 15; 51(4):880-914.

[19] Vanetti E, Nicolini G, Nord J. On the role of the optimization algorithm of Rapid Arc volumetric modulated arc therapy on plan quality and efficiency. Med Phys. 2011 Nov; 38(11):5844-56.

[20] Zacarias AS, Mills MD. Algorithm for correcting optimization convergence errors in Eclipse. J Appl Clin Med Phys. 2009 Oct 14; 10(4):3061.

[21] Holmes T. and Mackie TR. A comparison of three inverse treatment planning algorithms. Phys Med Biol. 1994 Jan; 39(1):91-106.

[22] Jeraj R, Keall PJ, Sieber JV. The effect of dose calculation accuracy on inverse treatment planning. Phys Med Biol. 2002 Feb 7;47(3):391-407.

[23] Jeraj R, Wu C, Mackie TR. Optimizer convergence and local minima errors and their clinical importance, Phys Med Biol. 2003 Aug 12; 48(17):2809–27.

[24] Dogan N, Siebers JV, Keall PJ, Lerma F, Wu Y, Fatyga M, Williamson JF, Schmidt-Ullrich RK. Improving IMRT dose accuracy via deliverable Monte Carlo optimization for the treatment of head and neck cancer patients. Med Phys. 2006 Nov; 33(11):4033-43

[25] Mihaylov IB, Siebers JV. Evaluation of dose prediction errors and optimization convergence errors of deliverable-based head-and-neck IMRT plans computed with a superposition/convolution dose algorithm. Med Phys. 2008 Aug; 35(8): 3722–3727.

[26] Tol JP, Dahele M, Doornaert P, Slotman BJ, Verbakel WF. Different treatment planning protocols can lead to large differences in organ at risk sparing. Radiother Oncol. 2014 Nov; 113(2):267-71.

[27] Prescribing, Recording, and Reporting Photon-Beam Intensity-Modulated Radiation Therapy (IMRT): Contents. Journal of the ICRU. 2010 Apr; 10(1).

[28] Feuvret L, Noel G, Mazeron JJ, Bey P. Conformity index: a review. Int J Radiat Oncol Biol Phys. 2006 Feb 1; 64(2):333-42.

[29] Sheng K, Molloy JA, Larner JM, Read PW. A dosimetric comparison of non-coplanar IMRT versus Helical Tomotherapy for nasal cavity and paranasal sinus cancer. Radiother Oncol. 2007 Feb; 82(2):174-8.

[30] Chen MJ, Novaes PE, Gadia R, Motta R. Guidelines for the treatment of lung cancer using radiotherapy. Rev Assoc Med Bras. 2017 Sep; 63(9):729-732.

[31] Chan C, Lang S, Rowbottom C, Guckenberger, M, Faivre-Finn C. Intensity-modulated radiotherapy for lung cancer: current status and future developments. J Thorac Oncol. 2014 Nov; 9(11):1598-608.

[32] Murshed H, Liu HH, Liao Z, Barker JL, Wang X, Tucker SL, Chandra A, Guerrero T, Stevens C, Chang JY, Jeter M, Cox JD, Komaki R, Mohan R. Dose and volume reduction for normal lung using intensity-modulated radiotherapy for advanced-stage nonsmall-cell lung cancer. Int J Radiat Oncol Biol Phys. 2004 Mar 15;58(4):1258-67.

[33] Zhang GG, Ku L, Dilling TJ, Stevens CW, Zhang RR, Li W, Feygelman V. Volumetric modulated arc planning for lung stereotactic body radiotherapy using conventional and unflattened photon beams: a dosimetric comparison with 3D technique. Radiat Oncol. 2011 Nov 9 ;6:152.

[34] Cattaneo GM, Dell'oca I, Broggi S, Fiorino C, Perna L, Pasetti M, Sangalli G, Di Muzio N, Fazio F, Calandrino R. Treatment planning comparison between conformal radiotherapy and helical tomotherapy in the case of locally advanced-stage NSCLC. Radiother Oncol. 2008 Sep; 88(3):310-8.

[35] Chan OS, Lee MC, Hung AW, Chang AT, Yeung RM, Lee AW. The superiority of hybrid-volumetric arc therapy (VMAT) technique over double arcs VMAT and 3D-conformal technique in the treatment of locally advanced non-small cell lung cancer–a planning study. Radiother Oncol. 2011 Nov;101(2):298-302.

[36] Liu HH, Wang X, Dong L, Wu Q, Liao Z, Stevens CW, Guerrero TM, Komaki R, Cox JD, Mohan R. Feasibility of sparing lung and other thoracic structures with intensity-modulated radiotherapy for non-small-cell lung cancer. Int J Radiat Oncol Biol Phys. 2004 Mar 15; 58(4):1268-79.

[37] McGrath SD, Matuszak MM, Yan D, Kestin LL, Martinez AA, Grills IS. Volumetric modulated arc therapy for delivery of hypofractionated stereotactic lung radiotherapy: A dosimetric and treatment efficiency analysis. Radiother Oncol. 2010 May; 95(2):153-7.

[38] Christian JA, Bedford JL, Webb S, Brada M. Comparison of inverse planned three-dimensional conformal radiotherapy and intensity-modulated radiotherapy for non-small-cell lung cancer. Int J Radiat Oncol Biol Phys. 2007 Mar 1;67(3):735-41.

[39] Bree Id, van Hinsberg MG, van Veelen LR. High-dose radiotherapy in inoperable nonsmall cell lung cancer: comparison of volumetric modulated arc therapy, dynamic IMRT and 3D conformal radiotherapy, Med Dosim. 2012 Mar 28; 37(4):353–357.

[40] Ong CL, Verbakel WF, Cuijpers JP, Slotman BJ, Lagerwaard FJ, Senan S. Stereotactic radiotherapy for peripheral lung tumors: a comparison of volumetric modulated arc therapy with 3 other delivery techniques. Radiother Oncol. 2010 Dec; 97(3):437-42.

[41] Simeonova A, Abo-Madyan Y, El-Haddad M, Welzel G, Polednik M, Boggula R, Wenz F, Lohr F. Comparison of anisotropic aperture based intensity modulated radiotherapy with 3D-conformal radiotherapy for the treatment of large lung tumors. Radiother Oncol. 2012 Feb; 102(2):268-73.

[42] Boyle J, Ackerson B, Gu L, Chris R. Kelsey R. Dosimetric advantages of intensity modulated radiation therapy in locally advanced lung cancer. Adv Radiat Oncol. 2017 Jan-Mar; 2(1): 6–11.

[43] Moon SH, Cho KH, Lee CG, Keum KC, Kim YS, Wu HG, Kim JH, Ahn YC, Oh D, Lee JH. IMRT vs. 2D-radiotherapy or 3D-conformal radiotherapy of nasopharyngeal carcinoma. Strahlenther Onkol. 2016 Jun; 192(6):377-85.

[44] Fiandra C, Filippi AR, Catuzzo P, Botticella A, Ciammella P, Franco P, Borca VC, Ragona R, Tofani S, Ricardi U. Different IMRT solutions vs. 3D-Conformal Radiotherapy in early stage Hodgkin’s lymphoma: dosimetric comparison and clinical considerations. Radiat Oncol. 2012 Nov 2; 7:186-195.

CONCLUSIONS

Conclusions

In this thesis work, two problems of validation and quality assurance in radiotherapy were treated. The first problem deals with the influence of the acquisition of radiation beam data on the accuracy of radiotherapy treatment planning by considering scenarios of involuntary but plausible wrong positioning of the water phantom and the ionization chamber. The second problem is related to the validation of the implemented intensity modulation radiotherapy technique (IMRT) for the treatment of lung cancer and its advantage when compared to the 3D conformational technique (3D-CRT) already used in the cancer fighting centre of Setif.

For the first problem treated, the results of this work show that a bias in the positioning of the water phantom by an inclination up to 1 ° did not significantly affect the accuracy of the dose calculation undertaken on the basis of the new PDDs, dose profiles and reference dose measured. Indeed, the observed differences in terms of flatness of the dose profiles are considered as negligible from a dosimetric point of view. In addition, it has also been verified that the bias on the ionization chamber positioning by a shift of almost five millimeters (5 mm) above the water level did not cause a significant error on dose calculation by the TPS. Likewise, the slight variations observed on the PDDs and the reference dose had no effect on the accuracy of the dose calculation performed by the TPS. Our approach by considering such error scenarios in relation with beam data acquisition has therefore proven to be very interesting insofar as it was able to tell us to what extent these plausible errors can be tolerated. Thus, this approach fits well into the overall quality assurance approach in external radiotherapy.

Concerning the second problem related to the validation of the IMRT in the treatment of lung cancer that is characterized by the existence of wide ranges of heterogeneities and its advantage when compared to 3D-CRT, theoretical (calculation) and experimental comparisons by thermoluminescence dosimetry and TPS calculation were performed. The results of this validation work have clearly shown that the IMRT, compared to 3D-CRT, ensures the protection of normal and at risk organs and provides a more precise treatment plan, thanks to its DVO dose optimization algorithm. Indeed, IMRT with its DVO dose optimization algorithm clearly improves the dose coverage of the target volume which is surrounded by heterogeneous media. Our results clearly demonstrate that IMRT effectively contributes to reduce the radio-toxicity of the sensitive organs and OARs in the treatment of lung cancer, things which avoid the observation of side effects after treatment. For the considered treatment of the lung cancer, experimental measurements have shown that 3D-CRT tends to underestimate the dose in the lung and to overestimate it in the adjacent tissues. Experimental measurements on the 19 points considered within Rando phantom have shown that the two radiotherapy techniques globally respect the constraints on dose delivery except for two points observed for 3D-CRT.

At the cancer fighting centre of Sétif, IMRT is now used for patients whose cases to be treated are unfavorable to the application of 3D-CRT and for patients who are judged to have a low survival chance after radiotherapy treatment. On the basis of this work results, it is recommended that the application of IMRT be extended to the treatment of lung cancer after the installation of suitable techniques for respiratory movement reducing or automatically triggering of dose delivery according to the patient's respiratory rate (Gating).

Abstract: In this thesis work, two problems of validation and quality control in radiotherapy were treated. The first problem deals with the influence of the acquisition of radiation beam measured data on the accuracy of radiotherapy by considering scenarios of involuntary but plausible errors in relation the wrong positioning of the water phantom and the ionization chamber. The second problem is related to the validation of the intensity modulation radiotherapy technique (IMRT) for the treatment of lung cancer and its advantage compared to the 3D conformal technique (3D-CRT). Regarding the first problem, the results of this work showed that positioning bias by tilting the water phantom up to 1° and the elevation of the ionization chamber by almost five millimeters (5 mm) above the water level produced no significant effect on the accuracy of the dose calculation undertaken using the new PDDs, dose profiles and reference dose measured . Concerning the second problem, the results of this validation work clearly showed that IMRT, compared to 3D-CRT, ensured the protection of normal and at risk organs and provided a more precise treatment plan; thanks to its dose optimization algorithm DVO. For the treatment of the lung cancer considered, experimental measurements have shown that 3D-CRT tends to underestimate the dose in the lung and to overestimate it in the adjacent tissues. Experimental measurements by thermoluminescence dosimetry have clearly shown that the two radiotherapy techniques respect well the dose constraints with a clear advantage of the IMRT.
Keywords: Radiotherapy; Beam data; Quality assurance; IMRT; 3D-CRT.

Résumé : Dans ce travail de thèse, deux problèmes de validation et de contrôle qualité en radiothérapie ont été traités. Le premier problème traite de l'influence de l'acquisition des données de mesure du faisceau d'irradiation sur la précision de la radiothérapie en envisageant des scénarios d'erreurs involontaires mais plausibles par rapport à de mauvais positionnements du fantôme d'eau et de la chambre d'ionisation. Le deuxième problème est par rapport à la validation de la technique de radiothérapie par modulation d'intensité (IMRT) pour le traitement du cancer des poumons et son avantage par rapport à la technique conformationnelle 3D (3D-CRT). Par rapport au premier problème traité, les résultats de ce travail ont montré que des biais positionnement par inclinaison du fantôme d'eau jusqu'à 1° et élévation de la chambre d'ionisation de presque cinq millimètres (5 mm) au dessus du niveau d'eau n'ont engendré aucun effet significatif sur l'exactitude du calcul de dose entrepris à partir des nouveaux PDDs, profils de dose et dose de référence mesurés. Concernant la deuxième problématique, les résultats de ce travail de validation ont bien montré que l'IMRT, à comparer à la 3D-CRT, assurait la protection des organes normaux et à risque et fournissait un plan de traitement plus précis grâce à son algorithme d'optimisation de dose DVO. Pour le traitement du cancer du poumon considéré, les mesures expérimentales ont montré que la 3D-CRT a tendance à sous-estimer la dose dans le poumon et à la surestimer dans les tissus adjacents. Le mesures expérimentales par dosimétrie de thermoluminescence ont bien montré que les deux techniques de radiothérapie respectent les contraintes sur la dose avec un net avantage pour l'IMRT.
Mots-clés : Radiothérapie ; Données faisceau ; Assurance qualité ; IMRT ; 3D-CRT.

ملخص: في هذه الا طروحه ، تم علاج مشكلتين للتحقق من الج دوة ومراقبة الجودة في العلاج الإشعاعي. تتعامل المشكلة الأولى مع تأثير دقه بيانات قياس حزمة الإشعاع على دقة العلاج الإشعاعي من خلال النظر في سيناريوهات الأخطاء اللاإرادية ولكن معقولة الحدوث فيما يتعلق بالتموضع الخاطئ لمجسم الماء و غرفة التأين. وتتعلق المشكلة الثانية بالتحقق من جدوى تقنية العلاج الإشعاعي بتعديل الكثافة (IMRT) لعلاج سرطان الرئة ومزاياها مقارنة بتقنية المطابقة ثلاثية الأبعاد (3D-CRT). فيما يخص المشكلة الأولى التي تم علاجها ، أظهرت نتائج هذا العمل أن التحيز ع ن المواضع الصحيحة عن طريق إمالة مجسم الماء حتى 1 درجة و رفع غرفة التأين بحوالي 5 ملم فوق مستوى الماء لم ينتج عنه تأثير ملحوظ على دقة حساب الجرعة التي تم إجراؤها باستخدام الـ PDDs، تغيرات الجرعة العرضية ، والجرعة المرجعية الجديدة . فيما يتعلق بالمشكلة الثانية، أظهرت نتائج هذا التحقق بوضوح أن تقنيه IMRT ، مقارنة بـ 3D-CRT ، ضمنت حماية الأعضاء المعرضة للخطر وقدمت خطة علاج أكثر دقة بفضل خوارزمية تحسين الجرعة DVO. لعلاج سرطان الرئة الذي تم النظر فيه ، أظهرت القياسات التجريبية أن تقنيه 3D-CRT تميل إلى التقليل من الجرعة في الرئة والإفراط في تقديرها في الأنسجة المجاورة. أظهرت القياسات التجريبية بقياس الجرعات بتقنيه التوهج الحراري بوضوح أن كلا تقنيتي العلاج الإشعاعي المدروستان تحترمان قيود الجرعة مع ميزة واضحة لـIMRT.
كلمات مفتاحيه : المعالجة بالإشعاع، بيانات حزمة الإشعاع، ضمان الجودة، IMRT، 3D-CRT